ABSTRACT

The Study of Overlapping Sheath and Dust Particle Structures in Dusty Plasma

Mudi Chen, Ph.D.

Mentor: Truell W. Hyde, Ph.D.

Complex (dusty) plasma consists of plasma and dust particles which vary in size from nanometer to millimeter in diameter. Complex plasma exists across many different environments, and can be found in environments from the cosmos to industry. Due to plasma fluxes to its surface, a dust particle embedded in a complex plasma will charge negatively or positively depending on the charging mechanism. It should be noted that unless the electron are very energetic, the dust particle is usually negatively charged.

When a surface is immersed in plasma, the region closest to the surface where a quasi-neutral plasma no longer exists is called the plasma sheath. Due to the perturbative nature of the majority of diagnostics in common use, such sheaths, especially the sheath forming near surfaces, can exhibit complex geometries making their physics difficult to diagnose. In such plasma sheath, the surface most often has a negative electric potential, which allows negatively charged dust particles to levitate against the force of gravity. These dust particles can behave as minimally perturbative electrostatic probes. This technique is relatively simple since the necessary measurements are simply the position of the particle and its motion after perturbation.

A novel plasma diagnostic technique, the freefall particle technique, will be introduced in this thesis. This technique allows measurement of the sheath profile with small perturbations, high spatial resolution and minimal equipment requirements. This technique will be employed to investigate the sheath produced at a planar surface allowing investigation of the overlapping sheaths formed inside a glass box commonly used to confine dust in laboratory experiments. The first experimental measurements of the plasma sheath inside a trench-like structure will also be discussed, as will the ion-wake inside a glass box. Finally, the various dust particle structures will be studied. Through measurement of the external confinement force at each position of the dust particle structures, the relationship between dust particle structure formation and confinement is also examined.

The Study of Overlapping Sheath and Dust Particle Structures in Dusty Plasma

by

Mudi Chen, M.S.

A Dissertation

Approved by the Department of Physics

____

Lorin Swint Matthews, Ph.D., Chairperson

Submitted to the Graduate Faculty of
Baylor University in Partial Fulfillment of the
Requirements for the Degree
of

Doctor of Philosophy

Approved by the Dissertation Committee

____

Truell Hyde, Ph.D., Chairperson

____

Lorin Swint Matthews, Ph.D.

____

Anzhong Wang, Ph.D.

____

Qin(Tim) Sheng, Ph.D.

Accepted by the Graduate School
December 2022

____

J. Larry Lyon, Ph.D., Dean

Page bearing signatures is kept on file in the Graduate School.

TABLE OF CONTENTS

LIST OF FIGURES

LIST OF TABLES

ACKNOWLEDGMENTS

This thesis is the culmination of long and arduous journey that I have only been able to make as a result of the dedicated support I have received from so many people along the way.

The deepest and sincerest gratitude goes to my supervisor Dr. Truell Hyde for his invaluable guidance and insightful advice throughout my research. It is my great honor and privilege that I was given the opportunity to work under his supervision. His continuous concern and considerate care were significant for me. Working with him was definitely one of the most unforgettable experiences in my life. It is he who encouraged me when I encountered difficulties in my life and it is because of his help that I can finally break through myself. Without his support, patience and empathy, this thesis would not have been accomplished.

In addition, I would like to extend my heartfelt gratitude towards Dr. Lorin Matthews and all my committee members for their valuable comments and suggestions on my thesis.

Meanwhile, adoration goes to all the academics and colleagues in the department of physics at Baylor University who have enlightened me and helped me. They are kind and they are responsible. They stayed with me through the hard times. Making progress is always accompanied by challenges, and I am grateful to have met you all.

Above all my sincere appreciation goes to my beloved families who have always been helping me out of difficulties and supporting without a word of complaint. They have always supported me unconditionally in every decision I made and guided my direction when I was confused. Especially to my grandmother, whose departure was truly heart-breaking, but meanwhile whose words of encouragement continued to inspire me.

At last, please allowed me to say something to myself who has been insisting: Please maintain this love and continue to strive to live up to dreams even in the most difficult moments. Those who sow with tears will reap with joy. We will all have bright futures, in various ways.

ATTRIBUTIONS

The work detailed in Chapter Five has been partly reproduced from a publication by multiple authors with the permission of The American Physics Society journal, Physics Review E. As such it is appropriate to detail the contribution of each coauthor. The author of this dissertation (Mudi Chen) contributed to the collection of experimental data, analysis of the experimental data to prove the existence of the Ion-wake and create the ion-wake field map, as well as writing of the manuscript. Michael Dropmann contributed to the experimental data collection and assisting to create the freefall particle method. Lorin S. Matthews and Truell W. Hyde contributed to the improvement of writing manuscript.

CHAPTER ONE

Introduction

1.1. Plasma

Plasma is not just a physics definition which has no direct impact on our lives. In cosmology, plasma can be found in stellar interiors, ionospheres, gaseous nebulae, interstellar media, Van Allen radiation belts, solar wind, and elsewhere. On the earth and in our daily life, plasma phenomena are also present, for example, lightning, the aurora, fluorescent lighting, rocket exhaust, medical treatment and the semiconductive industry. Plasma is often defined as the fourth and most common state of matter, composing 99% of the visible universe. Plasmas are conductive ensembles of electrons, ions and neutral molecules. Although the definition of plasma is simple, the parameter range in which plasma exists is much larger than for any other state of matter. Particle densities in plasma can be as small as 10^{-10} m^{-3} in space and as high as 10^{39} m^{-3} in fusion reactors, while the size of the plasma ranges from across the galaxy to nanosize deposition in the semiconductor industry. Plasma temperature range over 14 orders of magnitude from 10^{-2} to 10^{12} K. Fig. 1.1 provides a rough idea of the plasma parameters and corresponding phenomena that exist in 'normal' plasma.

With such a large range of parameters for plasma, it is perhaps surprising that so many common properties within plasma phenomena exist. One of the main properties of a plasma is the collective effect, which helps define how charged particles interact with each other through the Coulomb force. Any single moving charged particle will also interact with its neighbors, resulting in both polarization of the medium and the establishment of a local electric field. In return, nearby particles will move collectively to reduce this electric field. Taken together, this phenomenon is called the "collective effect." The second important property of plasma is quasi-neutrality. When any deviation from neutrality emerges, the electrostatic interaction with the ions and electrons will create a local electric field or current compensating the non-neutrality.

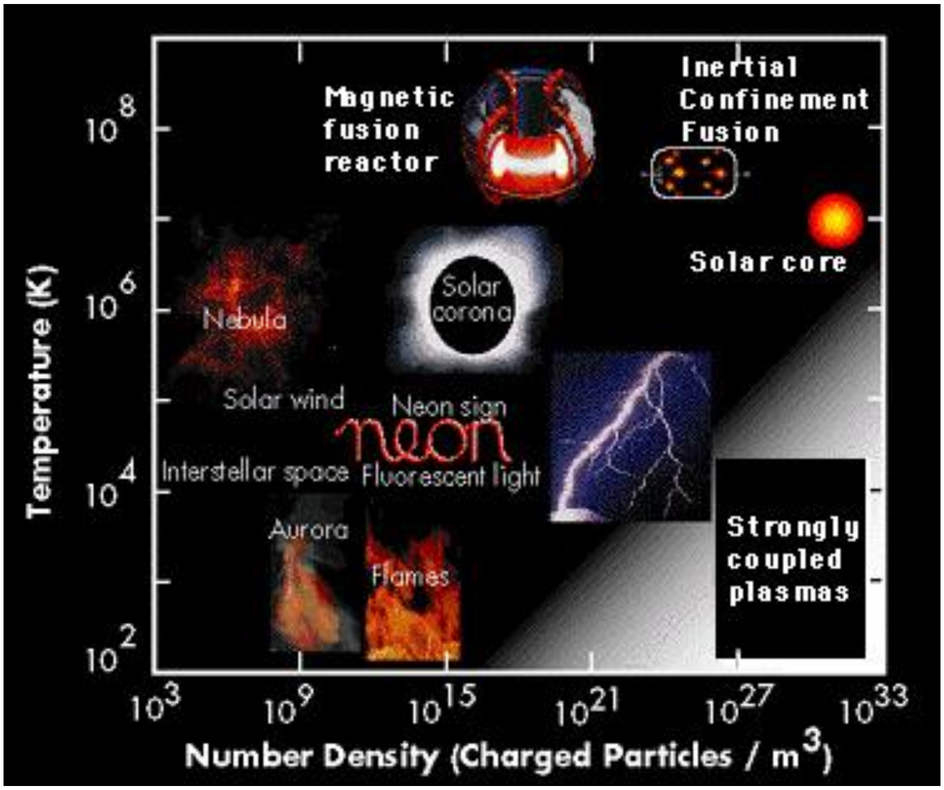

Figure 1.1. Plasma parameters for various types of plasmas (Courtesy of www.plasmas.org.)

1.2 Applications of Plasma

When discussing the applications of plasma, three main areas arise: fusion, space propulsion and the materials science and industry. Nuclear fusion is the process of combining nuclei to form different nuclei with subsequent release of huge amounts of energy. This is the process that powers the sun. If we can harness it, nuclear fusion has the potential to provide us with nearly limitless amounts of clean energy. There are three primary conditions necessary for nuclear fusion: high temperatures (on the order of about 10^7 K), high density, and prolonged stability. The high temperature requirement places fusion in the plasma regime. Although experiments have attained these high temperatures, it has proven to be extremely difficulty to achieve a sufficiently high combination of density and stability at the same time.

Plasmas also have potential applications in spacecraft propulsion. Among the earliest reported electrodeless plasma thrusters were the pulsed inductive thrusters developed at the aerospace corporation, TRW in the 1960s. This system used charge stored in a capacitor to produce a rapidly increasing current in a planar coil that ionized a propellant gas and then accelerated the resulting plasma through magnetic pressure [Dailey and Lovberg 1987,1988]. Similar devices are still under investigation. This development was followed in the 1980s by the hybrid plume plasma rocket where plasma, confined by magnetic mirrors in a solenoidal field, was heated by radio frequency energy and then accelerated through the magnetic nozzle formed within a diverging magnetic field [Yang, 1988]. Now known as the Variable Specific Impulse Magnetic Rocket (VASIMR), this hybrid device is currently undergoing durability tests that are expected to bring the device to NASA's TRL5 in the near future [NASA. gov].

The applications of plasma most likely to directly impact on our daily lives are in the material sciences industry, as defined by plasma etching, material deposition, ion implementation and others. The primary advantages plasma brought to this rapidly developing set of industries are its high energy and active particle density. For example, in DC electrical arcs or RF inductive plasma torches, the plasma power density can range from 100 W/cm^3 to 10 kW/cm^3. Such plasmas are in thermodynamic or thermal equilibrium at these temperatures and capable of melting or even vaporizing materials. Fig. 1.2 shows some of the primary applications plasma impacts within the industrial sapce.

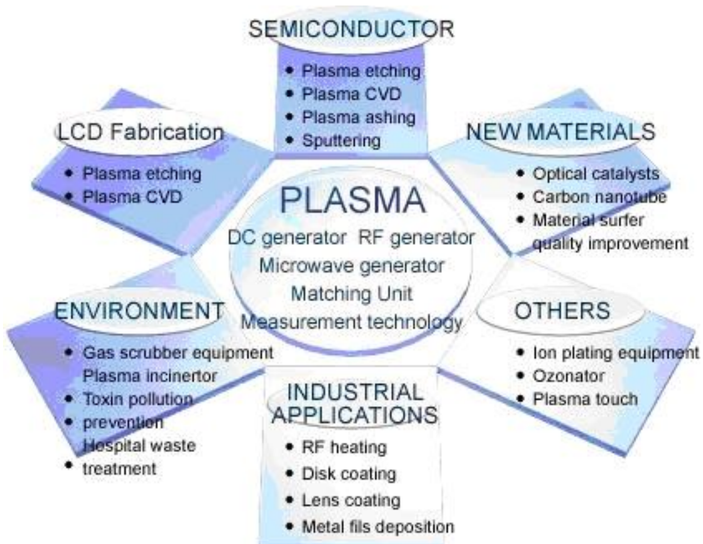

Figure 1.2. Various present applications of plasma technologies (Image Courtesy: en.adtec-rf.com)

1.3 The Development of Dusty (Complex) Plasma

Small charged dust particles are often found in plasmas in space, such as in the interstellar medium, in cometary environments, in planetary magnetospheres and in the upper atmosphere. In this case, the dust particles involved are round or irregularly shaped grains of carbon, silicates or other material measuring on the order of a micrometer or a fraction of a micrometer in diameter. Such small fine micrometer size particles in space were first examined in detail by Pioneers Spitzer [Spitzer 1978] and Alfven [Alfven 1954], while Irving Langmuir reported the first laboratory observation of a dusty plasma in 1924 [Langmuir 1924].

Langmuir, at the Centenary of the Franklin Institute, presented his observation on minute droplets, or globules, of tungsten vapor in an arc discharge and proposed a theory which include the formation of minute solid particles and the attachment of electrons to the droplets. In the 1940s, Spitzer discussed the charging process for dust grains in interstellar space and suggested the possibility of the presence of dust grains in this plasma environment with both negative and positive charges. Positive charges are present because of photoelectric emission by UV light, while dust grains could be negatively charged because of the plasma particles (fast moving electrons and slow moving ions) arriving at and absorbed by the dust particles. The plasma in interstellar space is mainly composed of hydrogen, while heavy elements exist as dust grains in interstellar space. The total ratio of gas mass (including He) to dust mass was estimated to be about 160 in interstellar space [Spitzer 1978]. Most heavy atoms are considered to be condensed on grains, together with about one-third of C, N and O atoms. The observation of the polarization of starlight was explained in terms of interstellar dust grains [Thompson 1962]. Hiltner discovered that the polarization depends not on the nature of the emitting star, but on its distance from the earth. The discovery suggested the effect of interstellar dust grains, particularly the scattering by elongated (aspherical) paramagnetic dust grains aligned by a weak interstellar magnetic field of nT strength [Hiltner 1949]. Much later, dusty plasmas attracted attention in the plasma community through the observation of dust in the processing in reactive plasmas in the 1980s. Research in contamination control in the semiconductor industry revealed that the particulate contamination of silicon substrates was produced from the plasma itself rather than from external air. The micrometer-sized particles, conveniently called dust, were formed and grew in the gas through aggregation. They formed a cloud electrically levitated above the wafer and fell on the wafer when the applied voltage on the wafer was turned off. The Coulomb lattice, predicted in 1986 to exist in a plasma [Ikezi 1986], was discovered in 1994 in the form of a Coulomb crystal, where dust particles in a plasma form regular structures [Chu 1994]. Experimental discoveries of Coulomb crystals in laboratory dusty plasmas rekindled the interest in Coulomb lattice formation, and recent research on plasma crystallization includes the study of phase transitions, lattice defects and others. Since micrometer-sized dust particles in laboratory plasmas can accumulate thousands of electrons on the surface, the resulting Coulomb repulsion between charged dust grains is expected to be strong. The dusty plasma is now known as a complex plasma which characterizes a complex system in which charged dust particles interact with plasmas. Fig.1.3 to Fig. 1.6 show some classical dusty plasma phenomena.

Figure. 1.3. Star formation in the Eagle Nebula. (Courtesy of Space Telescope Science Institute, NASA.)

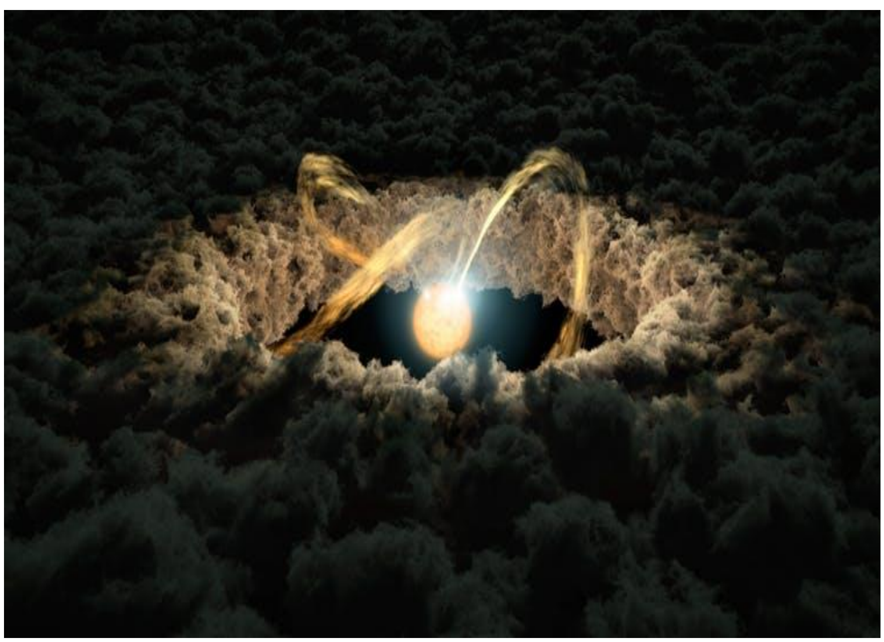

Figure 1.4. Illustration of a star surrounded by a protoplanetary disk. (NASA/JPL-Caltech, CC BY-ND)

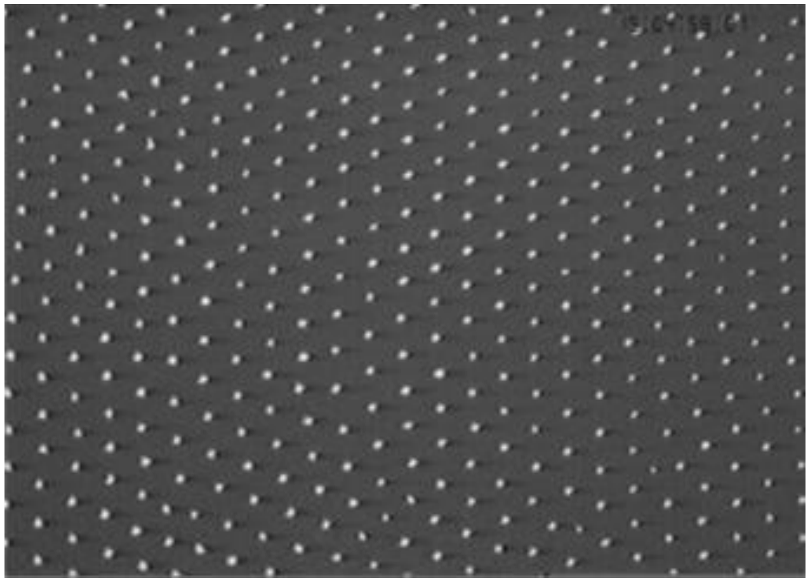

Figure 1.5. Dust crystal (MPE lab)

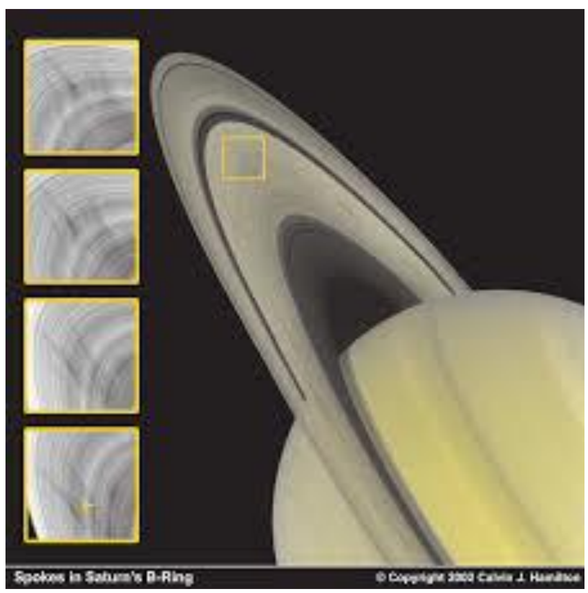

Figure 1.6. Spokes in Saturn's rings. The spokes are the radially extended dark features. (Andre Melzer 2012)

1.4 The Potential Applications of Dusty Plasma

1.4.1 Applications in Industry

In industry, typical plasma processes operate in reactive gases, like silane, hydrocarbons, fluorocarbons or organosilicons. These gases are required to deposit thin films on substrates or to etch into silicon layers, photoresists or protective films, for examples, in chip manufacturing or in solar cell production. In the plasma etching and sputtering or thin film deposition process, dust particles are usually considered harmful. In these processes, dust particles can grow either due to plasma polymerization, or particles etched or sputtered from the substrate can arrive in the plasma and can be trapped there. When such dust particles are deposited onto the substrate during the discharge cycle or during switch off, these particles can damage the surface properties and can easily destroy integrated circuits. They can cause short circuits or may clog up wafer trenches. Due to the small size of these dust particles (micrometers and even nanometers), it is difficult to detect them. In order to prevent or control this damage, investigating the dust particle's behavior in the plasma, especially in the plasma sheath, is sorely needed.

Dust particles produced in plasma-chemical systems can also have very interesting and useful properties since it is possible to control both their size and composition. Plasmas can not only be used to grow 'designer' particles but can also be used to modify the properties of existing materials that are introduced into the processing plasmas. One of the main advantages of the use of low pressure plasmas is the size of grown particles can be controlled and the very nature of the processe leads to the formation of relatively monodisperse (very narrow size distribution) particles. The nanoparticles grown in plasma discharges are seen as the building blocks of nanotechnology. Bouchoule gives very detailed examples of these applications[Bouchoule 1999].

1.4.2 Dust in Fusion Devices

Dust in fusion devices occurs due to the interaction of the plasma with the plasma facing components (like graphite or carbon fiber composite tiles) of the vessel. Dust can be produced by thermal overload of the surfaces leading to brittle destruction of carbon, to melt layer loss of metals or to disintegration of co-deposited layers. The problems that are associated with dust in fusion devices are the following. First, dust can lead to difficulties with the vacuum vessel and pumping. Second, diagnostics might be covered by dust. For example, mirrors for optical diagnostics of the plasmas might be 'blinded' by the dust. More important, material eroded from the wall could enter the core plasma, which can occasionally lead to the device stop operating, e.g., in some tokamaks, tungsten is used as a plasma facing component. Finally, in a real deuterium-tritium fusion plasma, the radioactive tritium can be chemically bound to carbonaceous dust particles, which will cause safety problems as the dust must be cleaned out and disposed of. Solving these problems requires the improvement of dusty plasma study.

1.4.3 Other Applications of Dusty Plasma

Besides the applications mentioned above, there are still many areas dusty plasma can offer significant help. In environmental areas, charging the fine powders of particles on the order of 10 nm are used for environmental pollution control. For example, soot particles in diesel engine exhausts and aerosol particles are controlled through the charging of the particles. Plasma deposition technology is developing as an application to the biomedical field. Nanoparticles are used to produce nanocomposite biocompatible materials. These materials can be applied for bone ingrowth or for drug delivery systems to treat brain tumors. Concepts of dusty plasma can be extended to microbes exposed to plasma, where microbes can be considered as animate particulates. The Interaction of microbes with plasmas has been studied for the application of biotechnology. Germicidal effects of a non-equilibrium atmospheric pressure plasma generated by a resistive barrier discharge have been reported. The plasma exposure produced structural damage to E. coli bacteria. The electrophysical process apparently damages the bacterial cell [Laroussi 2003].

1.5 The Organization of the Dissertation

This work is mainly focusing on diagnosing the plasma sheath and measuring the ion-wake effect. The experiments presented were performed in a modified Gaseous Electronic Conference (GEC) radio- frequency (RF) reference cell in the Hypervelocity Impacts & Dusty Plasma Lab (HIDPL) at the Center for Astrophysics, Space Physics and Engineering Research (CASPER) located at Baylor University.

In this Chapter, an introduction to the plasma and dusty plasma has been given. In the next Chapter, the basic concepts and theory of the dusty plasma will be discussed. In Chapter Three, the experimental setup and the equipment involved will be introduced. In Chapter Four, a new technology for diagnosing the plasma sheath will be described and the results for the sheath of planar surface and overlapped sheaths will be analyzed. In Chapter Five, the experimental observation of ordered aligned dust particle structures will been shown and the relationship between the different structures and confinement will be discussed. In Chapter Six, the theory of the ion-wake effect will be introduced and the experimentally measurement method and results will be presented. In the final Chapter, a brief summary of the work discussed previously and a discussion of possible future work will be given.

CHAPTER TWO

Basic Theory of Complex Plasma

2.1 Plasma Generation

Plasma is often defined by two parts, the plasma bulk and the sheath. Usually, the plasma bulk is considered to be a 'quasineutral ionized gas of charged and neutral particles, which exhibits collective behavior' [Chen 2006]. This definition identifies two important concepts in the plasma bulk, which are ionization and an approximately equal electron density n_e and ion density n_i. The first points out the way to generate plasma while the second separates the plasma into the plasma bulk and the sheath.

Ionizing a gas is the easiest and most common method to generate plasma. To ionize neutral gas, various methods can be employed. These include heating gas to the temperature at which ionization occurs, usually a few thousand Kelvin, beaming electromagnetic waves of sufficiently high energy through a gas, or creating a large enough electric field to make a gas discharge. In most complex plasma laboratories, discharge plasma is the most widely used plasma. Two types of discharge plasma, a direct current (DC) discharge plasma and a capacitively coupled radio frequency (RF) discharge plasma, which are commonly used in both industry and laboratory experiments, will be briefly introduced here.

2.1.1 DC Discharge Plasma

DC discharge plasmas have been investigated for almost 200 years, primarily due to the fact that they offer a basic and very easily reproducible source of plasma. DC plasmas are typically configured with a negative cathode at one end and a positive anode at the other end separated from one another by a gas-filled gap. A sketch of the layout is shown in Fig. 2.1. The term “gas discharge” refers to a flow of electric current through a gaseous medium. For this to occur, at least some of the gas atoms and/or molecules must be ionized. Then, an electric field must be present to drive this current. Furthermore, the current, which provides power to the discharge, has to be continuous throughout the length of the discharge.

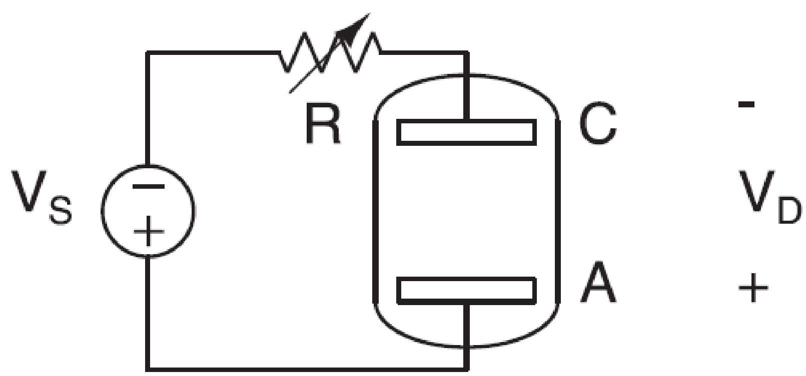

Figure 2.1. A sketch of a DC discharge plasma. Vs is the power source, R is the resistance of the system, C is the cathode, A is the anode and V_D is the voltage applied between the cathode and anode

In this case, free electrons are accelerated away from the cathode by the electric field created between the two electrodes, and gain energy. During their travel, they collide with and ionize neutral atoms, resulting in more charged particles. While the resulting electrons produced are accelerated and collide with more neutral atoms, the positive ions are accelerated toward the cathode, emitting electrons through the secondary electron emission process. Thus, a self-sustained discharge is created. In the resulting DC discharge, the current is driven by both ions and electrons created within the plasma volume, as well as by electrons emitted from the cathode.

2.1.2 Capacitively Coupled RF Discharge Plasma

To sustain a DC discharge, the electrodes must be conducting. When one or both of the electrodes are non-conductive, e.g. when a glow discharge is used for the spectro-chemical analysis of non-conducting materials or the deposition of dielectric films, the electrodes gradually become covered with insulating material. In this case, the electrodes will accumulate positive or negative charges and this will block the electrons or ions moving toward the electrodes. Then, the glow discharge will extinguish. This problem is usually overcome by applying an alternating voltage between the two electrodes, so that each electrode acts alternately as the cathode and anode. This has the benefit that the charge accumulated during one half-cycle will be at least partially neutralized by the opposite charge accumulated during the next half-cycle. The frequencies generally used for such alternating voltages are typically in the radiofrequency (rf) range (1 kHz–10^3 MHz) with a most common value of 13.56 MHz). The term ‘capacitively coupled’ refers to the way of coupling the input power into the discharge, employing two electrodes and their sheaths to form a kind of capacitor.

Unlike a DC discharge plasma, at RF frequencies, the electrons and ions exhibit a totally different behavior because of the difference between their mass. The highest frequency an individual electron or ion can follow is called the electron plasma frequency and ion plasma frequency. Their definitions are given in Eq. 2.1,

$$\omega_{pe} = \sqrt{\frac{n_e e^2}{m_e \epsilon_0}} \quad \text{and} \quad \omega_{pi} = Z\sqrt{\frac{n_i e^2}{m_i \epsilon_0}}\,, \tag{2.1}$$

where n_e, n_i is the density of the electrons and ions, m_e, m_e is the mass of the electron or ion, ϵ_0 is the permittivity of free space, e is the electron charge and Z is the charge state of the ion. For electron densities varying between 10^{10} to 10^{13} cm^{-3}, the electron plasma frequency ranges from 9×10^8 to 3×10^{10} Hz, which is much higher than the typical rf-frequency of 13.56 MHz. The ions, on the other hand, can only follow the field if the driving frequency is less than the ion plasma frequency. As a result, most of the excitation and ionization involved within the RF plasma is created by collisions between high speed electrons and neutral atoms, while the secondary electron emission caused by ion collisions with the electrodes is minor. When the applied discharge power is strong enough, a small number of free electrons are subject to acceleration by the electric field, colliding and ionizing atoms within the gaseous medium, thereby forming new electrons which undergo the same process in successive cycles, this is called "*electron avalanche*" [Sparks 1975]. As soon as an electron avalanche is triggered, the gas becomes electrically conductive due to abundant free electrons. Fig. 2.2 shows a sketch of a capacitively coupled discharge plasma.

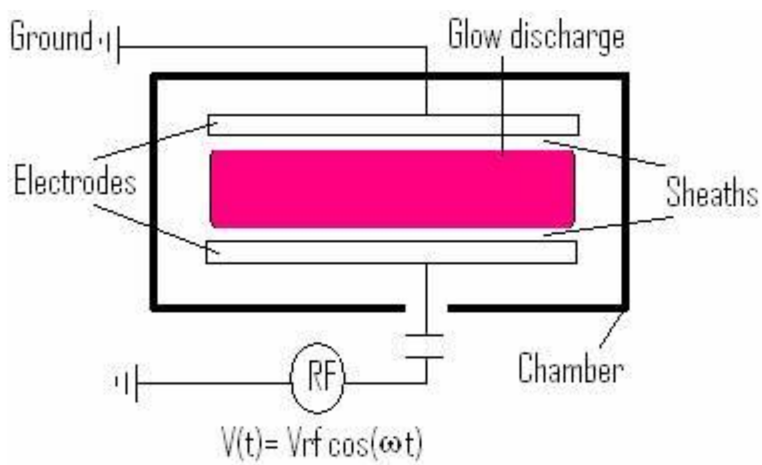

Figure 2.2. A sketch of a capacitively coupled discharge plasma system.

2.2 Debye Shielding

Plasma has a notable property in its ability to shield the electric field of an individual particle or particles within it. The distance characterizing the influence of the electric field produced by an individual charged particle on another charged particle inside a plasma is defined as "*the Debye Length*". This concept is introduced in many text books in a usually clear manner [Chen 1984, Meltzer 2014]. A brief description is given following.

The potential at a particular distance from a charged particle can be found using the Poisson equation of electrodynamics,

$$\nabla^2 \Phi = -\frac{\rho}{\epsilon_0} = -\frac{e(n_i - n_e)}{\epsilon_0}, \tag{2.2}$$

where Φ is the electric potential and ρ is the net charge density. Usually, electron and ions are assumed to follow a Boltzmann distribution,

$$n_e = n_{e0} \exp(\frac{e\,\Phi}{k_B T_e}), \qquad n_i = n_{i0} \exp(\frac{e\,\Phi}{k_B T_i}), \tag{2.3}$$

where $n_{e0,i0}$ is the unperturbed electron (ion) number density, k_B is the Boltzmann constant and $T_{e,i}$ is the electron (ion) temperature. By assuming $e\,\Phi \ll k_B T_{e,i}$ and substituting (2.3) into (2.2), the Poisson equation can be solved, providing

$$\Phi = \frac{Q}{4\pi\epsilon_0 r} \exp(-r/\lambda_D), \tag{2.4}$$

where Q is the total amount of net charge, r is the distance to the charged particle and λ_D is the Debye Shielding length,

$$\lambda_D^2 = 1/(\frac{1}{k_B T_e/4\pi\epsilon_0 n_e e^2} + \frac{1}{k_B T_i/4\pi\epsilon_0 n_i Z^2 e^2}) = 1/(\lambda_{De}^{-2} + \lambda_{Di}^{-2}), \tag{2.5}$$

where $\lambda_{De.Di}$ is the electron (ion) Debye length.

2.3 Plasma Sheath

As mentioned above, most plasmas exist in two parts, the plasma bulk and the plasma sheath. Although the plasma bulk is quasi-neutral, the plasma sheath is not. Due to the high mobility of electrons as compared to the ions, electrons are the first to arrive at the walls of a plasma device. If the walls are insulated, a negative electric potential will develop which grows to the point where new incoming electrons are repelled. If the walls are grounded, electrons are lost from the plasma, creating a net positive plasma potential. Thus, when compared to the bulk plasma, a positive space charge region is created immediately in front of the plate electrode ($n_i > n_e$), called the plasma “sheath.” This region appears optically dark due to the lack of excitation of neutral atoms. Therefore, in the region closest to the surface, a quasi-neutral plasma no longer exists.

2.3.1 Bohm Criterion

To understand the separation of the plasma bulk and plasma sheath, the *Bohm Criterion* is an important concept. Assuming the simplest representative case, we consider a neutral non-magnetized plasma with one kind of singly-charged ions in contact with an absorbing wall. Due to the higher mobility of the electrons, the wall will normally become negatively charged, so that the majority of new electrons are repelled. In this case, the thermal electrons are only weakly disturbed by wall losses and can be assumed to be in Boltzmann equilibrium. The corresponding decrease in the electron density forms a positive space charge shielding the potential distortion at a typical distance of some electron Debye lengths λ_{De} in front of the wall (see Fig. 2.3).

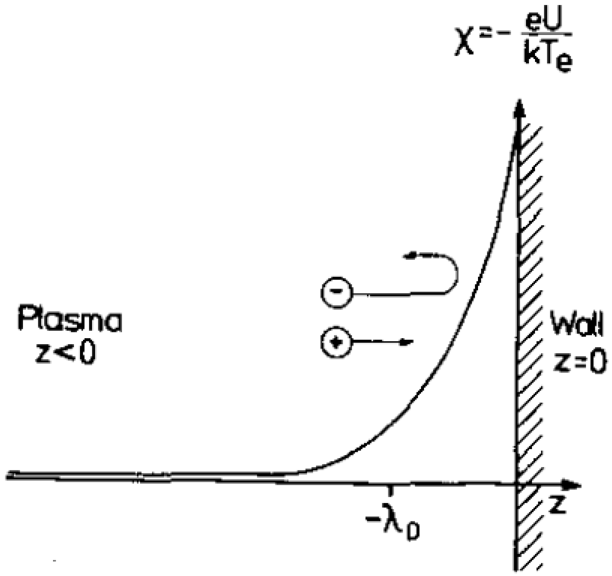

Figure 2.3. The positive sheath formation in front of a negative wall (Riemann 1991).

Assuming the plasma is collisionless, the electron distribution can be considered to be Maxwellian. At the boundary of plasma bulk and the plasma sheath, which is also called the sheath edge, $n_i = n_e$, the energy conservation and flux continuity equations for the ions can be expressed as,

$$\frac{1}{2}m_i u^2(z) = \frac{1}{2}m_i u_s^2 - eV(z), \tag{2.6}$$

$$n_i(z)u(z) = n_s\, u_s, \tag{2.7}$$

where $u(z)$ and u_s are the ion drift velocity in the sheath and its value at the sheath edge, respectively. Assuming $V(z)$ is the local electrostatic potential and n_s is the ion density at the sheath edge, the ion density in the sheath $n_i(z)$ can be expressed by,

$$n_i(z) = n_s / \sqrt{1 - \frac{2eV(z)}{m_i u_s^2}}, \tag{2.8}$$

and the resulting Poisson equation can be written as,

$$\frac{d^2V(z)}{dz^2} = \frac{en_s}{\epsilon_0}\left[\exp\left(\frac{eV(z)}{k_B T_e}\right) - \sqrt{\frac{2eV(z)}{m_i u_s^2}}\right]. \tag{2.9}$$

Eq. (2.9) has a real solution only if (Hall 1961),

$$u_s \geq V_B = \sqrt{{k_B T_e}/{m_i}}, \tag{2.10}$$

where V_B is called Bohm Speed and is also known as the ion sound speed, while Eq. (2.10) is named the Bohm Criterion. Hall pointed out that only when the ion speed exceeds the Bohm Speed, can a stable plasma sheath be formed. In physics terms, only when the ion speed is larger than the Bohm Speed, the ion density falls more slowly than the electron density**,** near the sheath edge, will a positive space-charge shielding the negative wall distortion from the neutral plasma be built up**.**

Many attempts have been made to locate a singular position that can be considered to separate the plasma from the sheath, thus defining the sheath edge. Initially, the location of the sheath edge was approximated by marking the position in the change in optical emission from the plasma [Melzer 1994]. Another standard definition is the position where the ions reach the Bohm velocity [Chen 2006]. Subsequent discussion led to a reworking of this definition to instead determining an electron edge, defined to be the point where the electron charge below this point equals the net positive charge above this point up to the center of the plasma [Brinkmann 2007]. A more recent method that has been adoped for higher pressures employs dust particles as probes in the plasma, determining the sheath edge by increasing the RF voltage amplitude (i.e., increasing the plasma power) until the dust reaches a stable vertical position. In this case, the dust particle identifies an approximate location of the sheath edge since the upward electric force increases (because the charge on the dust particle increases) with plasma power [Douglass 2012]. Beckers et al. proposed a sheath edge definition used to experimentally determine the location of the sheath edge as being where the plasma emission is reduced by a factor of 1/e (2011). An alternative experimental method to determine the sheath edge as defined theoretically is predicated on the measurement of the equilibrium height of nanoparticles [Samarian 2001]. However, all of these methods face challenges and have their own limits. The details will be discussed in a greater depth later chapter.

2.3.2 Electric Field in the Sheath

The potential difference between the bulk plasma and the electrodes creates an electric field within the sheath. The simplest estimation of the electric field in the sheath assumes a time averaged electric field which is only dependent on distance to the electrode. Neglecting electrons and assuming a constant ion density, the electric field can then be determined through integration of Eq. (2.11) [Melzer 1994] to be

$$E_z = \frac{en_i}{\epsilon_0}(z - z_s), \tag{2.11}$$

where z_s is the position of the sheath edge. Until recently, the electric field in a RF sheath has been widely assumed to be linear in nature [Homann 1998, Schollmeyer 1999]. Both numerical models and experimental measurements [Zafiu 2001, Samarian 2005] showed some validity of this assumption.

Recently, Tomme summarized nine separate methods, both theoretical and experimental, to show that the parabolic sheath potentials could be used, especially below the sheath edge [Tomme 2000]. It assumes the potential spans the fixed DC potential V_0 on the lower electrode and the plasma potential (V_P) at the sheath edge leads to the parabolic potential,

$$V_z = \frac{V_0 - V_p}{s^2} z^2 + \frac{2(V_p - V_0)}{s} z + V_0, \tag{2.12}$$

where is the distance from the lower electrode to the sheath edge which is also called the sheath thickness. Due to the lack of an accurate diagnostic method in the sheath, this approximation is widely used in investigations of the plasma sheath. However, this assumption assumes a zero electric field at the sheath edge, which is not always reasonable. As mentioned above, to generate a sheath, the ions must exceed the Bohm Speed which is much larger than the ion thermal speed, requiring a non-zero electric field at the sheath edge. Moreover, recent experimental work has determined that the electric field is in fact not linear throughout the entire sheath [Douglass 2011].

2.4 Dusty Plasma Basics

2.4.1 Charging

Similar to a surface immersed in plasma, when dust particles are injected into the plasma, they usually are negatively charged due to the high mobility of the electrons. The resulting negatively charged dust particles repel electrons and attract ions due to Coulomb forces. The final balance between the electron and ion fluxes leads to an equilibrium charge on the dust particle. One of the most commonly used approaches to describe the electron and ion fluxes to a dust particle surface is the *Orbital Motion Limited* (OML) approximation [Allen 1992].

Before introducing the details of basic OML theory, some assumptions need to be listed here:

(i) the dust particle is isolated and does not interact with other dust grains in its vicinity;

(ii) the plasma is collisionless implying electrons and ions approach the dust particle without collisions;

(iii) the effective potential has no boundary.

Additionally, there are a few essential ideas of OML theory. First of all, the collection of plasma electrons and ions by a dust particle is governed by their collisionless orbit. Therefore, these are subject to the energy and angular conservation laws. The energy and angular are defined as,

$$E = \frac{1}{2}m_\alpha(v_r^2 + v_t^2) + q_\alpha \Phi(\mathrm{r}), \tag{2.13}$$

$$J = m_\alpha v_t r \,, \tag{2.14}$$

where m_α and q_α are the mass and charge of the particles of species α $(\alpha = e, i)$, Φ is the plasma potential, while r, v_r and v_t are the radial distance, radial velocity and tangential velocity in a spherical reference framed centered on the dust particle. For this case, the radial motion of the electrons and ions can be described employing a one degree-of-freedom Hamiltonian with effective potential Φ_{eff},

$$H = \frac{1}{2}m_\alpha v_r^2 + \Phi_{eff}(r), \qquad \Phi_{eff}(r) = \frac{1}{2}\frac{J^2}{m_\alpha r^2} + q_\alpha \Phi(\mathrm{r}). \tag{2.15}$$

Secondly, for a typical negatively charged dust particle, Φ is negative and monotonically increasing with r, so that Φ_{eff} is positive and monotonically decreasing with r (for electrons). As a result, only electrons having $\mathrm{E} > \Phi_{eff}(r = r_d)$ can reach the dust particle, where r_d is the dust particle radius.

Last but not least, OML theory also approximates Φ_{eff} for ions as a monotonic function of r, which leads to the result the ions with

$$v_r^2 > -2\Phi_{eff}(r_d)/m_i \tag{2.16}$$

can also reach the dust particle. The assumption greatly simplifies the theory since $\Phi\,(r)$ is no longer needed to evaluate the ion and electron current collect by the dust particle. Solving Eqs. (2.15), the electron and ion current can be obtained as,

$$I_e = \sqrt{8\pi} n_{e0} r_d^2 \sqrt{\frac{k_B T_e}{m_e}} \exp\left(\frac{e\,\Phi_d}{k_B T_e}\right), \tag{2.17}$$

$$I_i = \sqrt{8\pi} n_{i0} Z r_d^2 \sqrt{\frac{k_B T_i}{m_i}} \left(1 - \frac{Ze\,\Phi_d}{k_B T_i}\right), \tag{2.18}$$

where $n_{e0,i0}$ is the electron (ion) density far away from the dust particle and Φ_d is the surface potential of the dust particle. Setting the two currents equal to one another allows a numerical solution for Φ_d to be obtained. To determine the charge on the dust particle, a capacitance model is assumed. Since the dust particles used in the experiments discussed here are spherical, the standard expression for spherical capacitance can be used

$$C = 4\pi\epsilon_0 r_d. \tag{2.19}$$

This yields the charge on the dust particle as $Q = C\,\Phi_d$.

For an 8.89 μm diameter dust particle, the charge is around 35,000 electronic charges using the parameters from a preview work (the gas pressure is 100mTorr and the system power is 2.7W) [Brandon 2014], with an estimated charging time, calculated using Eq. (2.17), of about 1 ms. In the experiments described here, the charge of the dust particle will always be considered to be in equilibrium.

Standard OML theory is only valid in a collisionless plasma and therefore not suitable for a high pressure case. Land [Land 2010] employed the screening length and ion mean free path to calculate the currents to the dust particle in order to adapt the above to a collisional plasma. Additionally, OML theory is also not capable of predicting the plasma response. This problem was recently solved by a modified OML model reported by Tang [Tang 2014].

Besides the collection charging mechanism just described, there are some other potential charging mechanisms. For example, when dust grains in space are examined, photoelectric emission must also be taken into account in the charging process. Ultraviolet light from stars (with energy h\nu > 10 eV) can cause ejection of electrons and thus a reduction, if not complete reversal, in charge magnitude. This process is thought to aid the dust coagulation that ultimately forms new planets or stars [Ma 2013]. Other charging mechanisms such as secondary electron emission, photoemission, thermionic emission, etc., will not be discussed in this dissertation, since they are not significant to the problem at hand.

2.4.2 Forces on a Dust Particle

All of the experiments presented in this dissertation have dust particles floating in a plasma. In order to properly understand the physics involved, the analysis of the forces acting on the dust particles is crucial. In labs , the dust particle sill generally experience the gravitational, electric field, neutral and ion drag forces and the thermophoretic force. This section will give a detailed introduction about all of these forces.

2.4.2.1 The gravitational force. Every particle in a laboratory dusty plasma generated on Earth is subject to the gravitational force. This force is strongly related to both the material and the size of the dust particles,

$$F_G = m_d g = \frac{4}{3}\pi r_d^3 \rho_d g, \tag{2.20}$$

where r_d and ρ_d is the radius and density of the dust particle and g is the gravitational acceleration. In all experiments and discussions in this dissertation, F_G is perpendicular to the bottom electrode of the CASPER GEC Reference Cell.

2.4.2.2 Electric field force. The electric field force discussed here is the electric field force provided by the sheath. As discussed previously, in a plasma dust particles immersed are negatively charged allowing them to levitate within the sheath. This electric field force is created by the sheath of every equipment surface immersed in the plasma and therefore is not only provided by the sheath of the lower electrode but also by the sheath of the side walls or any other equipment within the plasma, such as the surfaces that provide system confinement. The electric field force provided and acting on the dust particles creates an effect which is the major force compensating the gravitational force. This results in particle levitation in the sheath and also acts as the main confinement force determining the various structural states of the dust particles. The electric force acting on the dust particle created by the sheath from the bottom electrode, was introduced by Daugherty [Daugherty 1993], who provided the analytical equation,

$$F_E = ZeE[1 + \frac{\left({r_d}/{\lambda_D}\right)^2}{3\left(1+{r_d}/{\lambda_D}\right)}]. \tag{2.21}$$

The first term in Eq. 2.21 is due to the electric field created by the sheath while the second term is due to the presence of the charged dust grain, which produces a polarization in the surrounding plasma. In most cases, the second term is not significant when compared to the first term and can be ignored.

2.4.2.3 Neutral drag force. The neutral drag force is defined as the rate of momentum exchange between dust particles and neutral atoms during collision. The relative motion between the dust particles and the neutral atoms can be interpreted in one of two ways. The first is that the relatively static dust particles receive momentum transferred from the neutral gas flow while the second assumes the moving dust particles transfer their momentum in a roughly static gas background. The two important parameters for the neutral drag force are the Knudsen number and the relative particle velocity. The Knudsen number is defined as

$$K_n = \frac{l_{\mathrm{n}}}{r_d}\,, \qquad (2.22)$$

where l_{n} is the mean free path of the neutral atoms. Based on the value of the Knudsen number, the calculation of the neutral drag force is usually divided into two regimes: 1) $K_n \ll 1$, which is called the "*hydrodynamic*" regime and 2) $K_n \gg 1$, known as the "*kinetic*" regime.

In the first case, the neutral drag force can be interpreted employing Stokes law as

$$F_n = -6\pi\eta r_d v_d, \qquad (2.23)$$

where η is the viscosity of the neutral gas and v_d is the relative velocity of the particle. The minus sign ensures that the direction of the neutral drag force is always opposite to the particle's direction of motion. It should be noted that in this dissertation, since the gas pressure in the experiments discussed is relatively low, the "kinetic" regime will be assumed and the "hydrodynamic" regime will not be discussed in any detail.

In the second case, "kinetic" regime, the mean free path of the neutrals is usually much larger than the particle's radius. As such the comparison between the relative dust particle velocity v_d to the gas flow velocity u_n and the neutral thermal velocity v_T leads to two different expressions for the neutral drag force.

In the case $| v_d - u_n | \ll v_T$, the neutral drag force can be expressed by [Epstein 1924],

$$F_n = -\frac{4}{3}\pi m_n n_n r_d^2 v_T (v_d - u_n), \tag{2.24}$$

where m_n is the mass density of the neutral atoms and n_n is the number density of the neutral atoms. For the case $| v_d - u_n | \gg v_T$, the neutral drag force can be expressed by

$$F_n = -\pi m_n n_n r_d^2 v_T (v_d - u_n) \mid v_d - u_n \mid \tag{2.25}$$

In most dusty plasmas, the relative velocity between the particles and the gas flow is much smaller than the neutral thermal velocity. Therefore, the neutral drag force will only be discussed assuming the (2.24) expression.

In this case, the Epstein drag expression is a good approximation for the neutral drag force and can be written as

$$F_n = -\beta m_d v_d, \tag{2.26}$$

$$\text{with } \beta = \delta \frac{4}{3}\pi \sqrt{\frac{8}{\pi}}\, \frac{m_n n_n r_d^2 v_T}{m_d}, \tag{2.27}$$

where β is the damping rate coefficient also known as the *Epstein coefficient* and δ represents the collision mechanism. When δ =1.0, specular reflection dominates while δ =1.44 corresponds to perfect diffusion [Konopka 2000]. The δ value for melamine-formaldehyde (MF) particles (often used in dusty plasma experiments) has been experimentally determined by several groups [Konopka 2000, Liu 2003], with all measured results demonstrating good agreement with the Epstein expression.

2.4.2.4 Ion drag force. Because there is an electric field in the sheath, streaming ions will follow the direction of the electric field. The ion drag force is defined as the momentum transferred from flowing ions to the charged particles immersed in a dusty plasma. Due to the substantial size and mass of the ions, the ion drag can become significant under certain conditions. As a result, the ion drag force can play an important role in affecting or even determining the dust symmetry configuration in either a laboratory or microgravity plasma, resulting in “string chains” in the vertical direction [Morfill, Thomas 1996], “voids” in the center of the discharge under microgravity experiments [Fortov 2004] and a host of other interesting structural states. Compared to the neutral drag force, the ion drag force is much more complicated due to the additional interaction resulting from the charge on the particles.

Since the dust particles themselves are charged, there are two basic types of ion drag represented by the separate cross-sections. The first of these is the collection cross-section, which occurs when ions actually collide with the dust grain. The second is the Coulomb cross-section, which occurs as the ions flow past a dust grain, electrically interacting with the dust particle. It is this attraction that is believed to create the ion wake-field [Miloch 2012] beneath a dust particle, where flowing ions converge to generate a more positive region. This positive region can provide an attractive force to particles beneath the grain as well as generate vertical alignment. The ion-wake field will be discussed in details in Chapter Six.

2.4.2.5 Thermophoretic force. A temperature gradient within the plasma produces a thermally induced force that is directed from the high temperature region to the low temperature region. This is known as thermophoresis. This force can be described as

$$F_{th} = \frac{4\sqrt{2\pi} r_d^2}{15 v_T} k_n \nabla T_n, \tag{2.28}$$

where k_n is the thermal conductivity of the gas and T_n is the neutral temperature. In some experiments [Fortov 2004], this force is large enough to levitate the dust particle (even on the Earth). However, under the experimental conditions discussed in this dissertation, the thermophoretic force is negligible compared to the electric field force.

2.4.2.6 Particle Interaction (repulsive). Due to the Debye shielding, the electrostatic force between dust particles is not the Coulomb force. As known, the negatively charged dust particle is surrounded by a positive space charge and the electrostatic potential surrounding a spherical dust particle in a plasma with equilibrium charge Q_d is called the *screened Coulomb potential or Yukawa potential,*

$$\varphi(r) = \frac{Q_d}{4\pi\epsilon_0 r} \, e^{-r/\lambda_D}. \tag{2.30}$$

The repulsive interaction force between two dust particles can be obtained by the multiplication of particle charge and gradient of electrostatic potential,

$$F_{int} = -\frac{Q_d^2}{4\pi\epsilon_0 r} \left(\frac{1}{r} + \frac{1}{\lambda_D}\right) e^{-r/\lambda_D} \tag{2.31}$$

In most dusty plasma experiments, when the dust particles reach the equilibrium, their interparticle distances r are usually less than λ_D due to the existence of the external confinement. The confinement force may come from many sources, such as, the sheath of the equipment surface, the distribution of the plasma density, external laser and et.al. The particle interaction and the confinement force will be discussed in Chapter Five.

2.5 Summary and Challenge

In this chapter, the basic concepts in plasma and the basic theory in the dusty plasma have been briefly introduced. Most of the dusty plasma experiments on the earth take place in the plasma sheath. However, the lack of a diagnostic method for the sheath leads researchs to use the parameters measured in the plasma bulk to estimate the real experiment parameters, for example, Debye length, electron and ion temperature. All the theoretical and numerical studies for dust particle behavior in the sheath lack these experimentally measured parameters. Therefore, in this dissertation, to find a reliable method to diagnose the plasma sheath becomes our first and the most important goal.

CHAPTER THREE

Experiment Setup

3.1 Introduction of GEC RF Reference Cell

The initial design for the GEC RF reference cell was established by an *ad hoc* committee formed at the 1988 Gaseous Electronics Conference. The design was based on four guidelines [Hargis *et al* 1994]: 1) it could be easily replicated; 2) it would be able to accommodate a variety of diagnostics; 3) it would be compatible with the reactive gases used in plasma processing, and 4) it would employ discharge geometries relevant to those used in the manufacture of semiconductor devices. The initial GEC design was finalized in March 1989 and six chambers were built and installed in different laboratories to test. As shown in Fig. 3.1, a "standard configuration" GEC RF reference cell contains two parallel plate electrodes each having a diameter of 10.2 cm (4 in.) with an interspacing fixed at 2.54 cm (1 in.). These electrodes are insulated from the chamber employing electrical insulators which provide access to power, ground or bias for each electrode independently. Ground shields surround the insulators and spread from the electrode mounting flange to the plane of the electrodes. This ground shield minimizes sputtering of the insulator material, helping enhance the uniformity of the electric field between the parallel electrodes.

The GEC reference cell was designed to achieve a base pressure in the range of 10^{-4} mTorr with a 300 *l*/s turbo-molecular pump and to operate at a maximum pressure of approximate 10 Torr [Hargis *et al* 1994]. Gas is supplied to the discharge region through a “showerhead” type upper electrode which has 169 equally spaced holes (0.3 mm in diameter) and pumped out via the symmetric pumping manifold located near the bottom of the cell as shown in Fig. 3.1. This pumping configuration was designed to minimize azimuthal variations in the gas flow at pressures above 100 mTorr since relatively large azimuthal variation takes place when only one pump-out port is used, with this reduced to 10% when four symmetric pump-out ports being used [Hargis *et al* 1994].

(a)

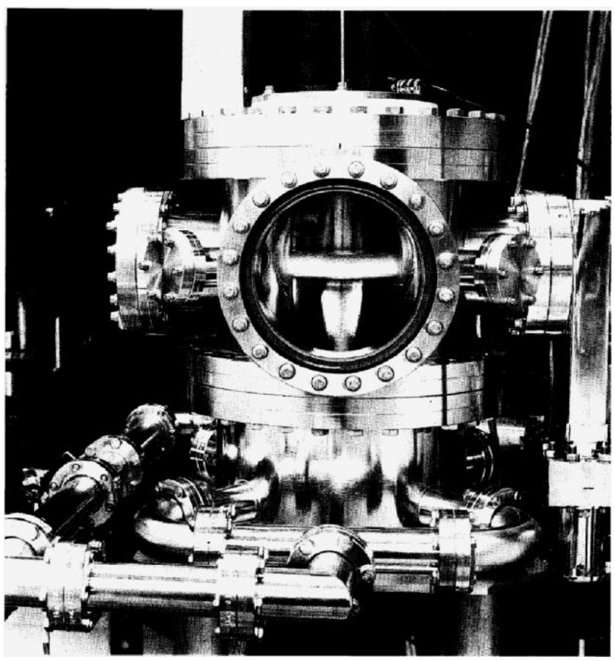

(b)

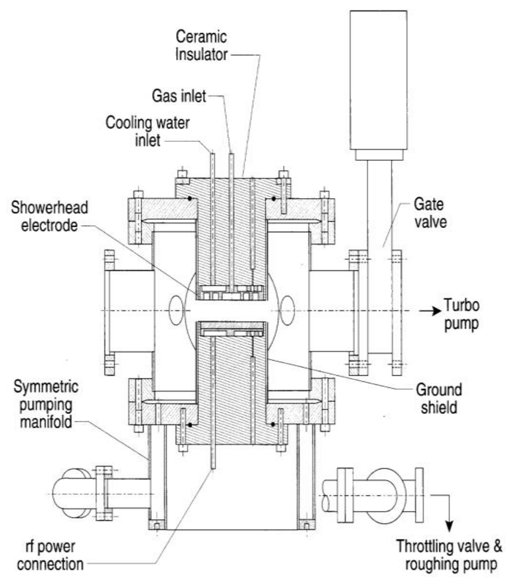

Figure 3.1. Photo (a) and schematic cross section diagram (b) of a standard-configuration GEC RF reference cell (Olthoff and Greenberg 1995).

3.2. CASPER GEC RF Reference Cell

All of the experiments presented in this dissertation are conducted in the CASPER GEC RF Reference Cell, which is located at Hypervelocity Impacts and Dusty Plasma Laboratory (HIDPL), part of the Center for Astrophysics, Space Physics, and Engineering

Research (CASPER) in Baylor University. The CASPER GEC RF Reference Cell has been extensively modified in order to be made suitable for dusty plasma research. Here, a brief introduction will be given and details can be found in the dissertation of Smith [Smith 2005].

3.2.1 Vacuum System

The pumping system for the CASPER GEC RF reference cell consists of three pumps: a turbo vacuum pump (Alcatel 5401CP), a roots vacuum pump (RUVAC WS 151) and a rotary vane vacuum pump (TRIVAC D 25 BCS). This combination is able to provide a background pressure of 10^{-4} mTorr (10^{-5} Pa). The roots vacuum pump is backed by the rotary vane vacuum pump, allowing for a high volume of gas to be processed while reducing back-streaming into the pump-out manifold. These two pumps are constrained in a stack (Fig. 3.2 (b)) which is connected to the pump-out manifold through a flexible PVC tube. The turbo vacuum pump (Fig. 3.2 (a)) is only applied when the pressure in the chamber is lower than 10^{-5} Torr (1.33×10^{-3} Pa). A gate valve connects the turbo vacuum pump to an 8 in. chamber port of the chamber to separate the turbo vacuum pump from the chamber when the pressure is above 10^{-5} Torr. In order to control low vacuum pressure, a butterfly valve is installed between the pump-out manifold and the foreline of the PVC tube. An exhaust valve controller (MKS 252) is employed to open and close the butterfly valve to maintain the desired pressure with the exhaust valve controller reading the pressure from a power supply readout (MKS PDR-C-1C). Finally, the gas flow rate into the chamber is controlled by a mass flow meter (FATHOM GR 112-1-A-PV) and a needle valve (Fig. 3.2 (c)), which for these experiments was set to 5~20 sccm (standard cubic centimeters per minute). The gas used for generating the plasma examined here was ultra pure argon (99.999%). Nitrogen gas was employed to prevent the chamber from contamination whenever the internal chamber is opened to atmosphere. A schematic of the entire vacuum system for the CASPER GEC RF reference cell is given in Fig. 3.3.

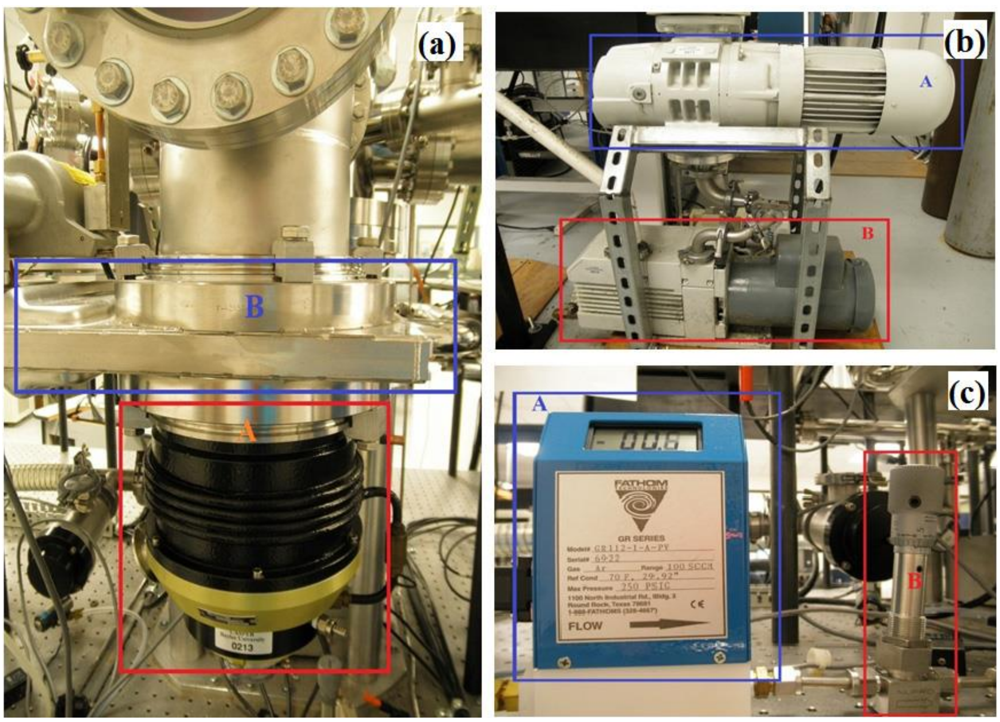

Figure 3.2. (a) The turbo vacuum pump (A) and gate valve (B). (b) The roots (A) and rotary vane (B) vacuum pumps. (c) The mass-flow control unit (A) and needle valve (B).

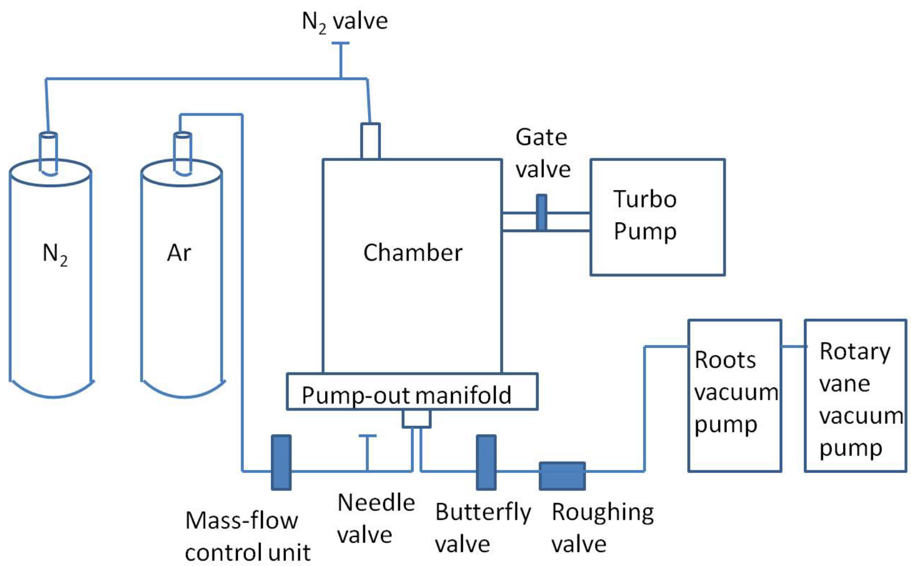

Figure 3.3. Schematic of the vacuum system for the CASPER GEC RF reference cell.

3.2.2. Illumination and Recording System

The CASPER GEC RF reference cell offers several windows for observation and illumination. Two diode laser setups are designed to illuminate dust particles with minimal radiation pressure perturbation: the horizontal laser sheet and the vertical laser sheet. The horizontal laser is a LASIRIS™ SNF Laser with wavelength 685 nm and a power of 50 mW and the vertical laser is a LASIRIS™ SNF Laser with wavelength 635 nm and a power of 10 mW. Cylindrical lenses are used to expand the laser produced beam into a laser sheet. The horizontal laser uses a LASIRIS™ SNF 5° fan angle, line generating lens and the vertical laser uses a LASIRIS™ SNF 1° fan angle, line generating lens. The maximum radiation pressure force for either of these is estimated to be on the order of 10^{-14} N, which is at least two orders of magnitude smaller than the gravitational force (10^{-12} N). Thus, the radiation force can be safely neglected. For accurate control in moving the laser sheets, stepper motors allow the lasers sheets to be moved in the (x, y, z) direction (Fig. 3.4). Both the laser and camera systems have stepper motors attached to screw drive actuators (Velmex UniSlide P40) which provide movement of each stage by a specific distance per step; for the P40 model, this distance is approximate 1.59 μm per step. The motors used for the laser and camera systems are different according to their required moving space. The laser systems use Velmex PK245 stepper motors while the camera systems use Velmex MO62 stepper motors.

To record the motion of the dust particles, several camera systems are used. In the CASPER GEC RF reference cell, two CCD (charge coupled device) cameras with microscope lenses are located at the top and side ports of the cell. Under normal conditions, the cameras used are Sony XC-HR50s which can reach 120 fps (frame per second). The top camera employs a Navitar Zoom 7000 lens, while the lens used on the side camera is an Infinity K2. When higher frame rates are required, a Photron camera (1024 PC Photron High Speed Camera) which can reach a maximum of 10^5 fps is employed (Fig. 3.4). In the experiments presented in this dissertation, both the XC-HR50 camera running at 120 fps and the Photron camera running at 250 to 2000 fps were used. All data collected by the cameras is immediately stored to a dedicated workstation and is ready for analysis. All cameras are mounted to stepper motors (Velmex MO62) and are free to move in (x, y, z) direction, allowing them to be properly focused (Fig. 3.4).

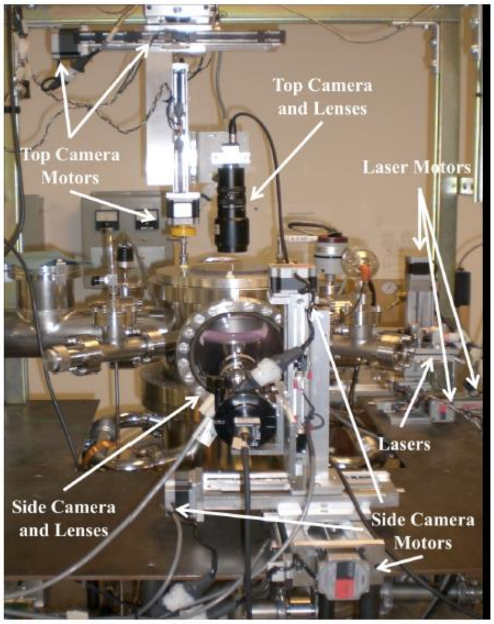

Figure 3.4. CASPER GEC RF reference cell setup with locations of cameras, lasers and motors marked. The purple glow in the center indicates the main gas discharge region in the chamber (Creel 2010).

Figure 3.5. Photograph of the 1024 PC Photron High Speed Camera mounted for side view in the CASPER GEC RF reference cell.

3.3.3 Manipulating Laser

Using laser to heat or push the particle is a convenient method to study the motion of dust particles. A Verdi Coherent G5 laser is employed to manipulate the dust particle in parts of the experiments presented in this dissertation. Based on optically pumped

semiconductor laser (OPSL) technology, the Verdi G-series is a robust multiwatt level continuous wave, low noise and high performance pump laser. The compact cavity design employs intracavity second harmonic generation to produce green (532 nm) visible light output, key for ultrafast Ti:Sapphire pumping (Fig. 3.6). OPSL technology offers many advantages inherited from its monolithic semiconductor chip used to produce laser light. Unprecedented flexibility in terms of variable output power with no effect on beam quality or beam pointing and extremely low noise are characteristics of OPSL lasers. In addition, the short upper-state lifetime of the OPS chip removes the “green noise” problem as seen in diode pumped solid-state (DPSS) lasers. Verdi G-Series lasers are available as single or multi-transverse mode.

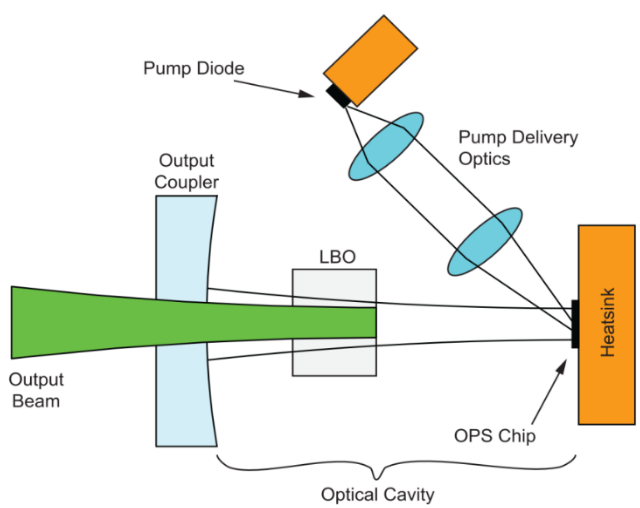

Figure 3.6. Verdi G-Series Laser Head Optical Schematic. (Coherent Co,)

The Verdi laser used to manipulate particles can be concentrated to a single spot or a sheet. In the majority of the experiments, the Verdi laser is set to single point mode. The illumination time is controlled by an auto-electrical shutter, the period (open and close once) of which can be as low as 0.01s. The power can vary from 0 to 20W, but for safety reason, in all of our experiments, the power is restrained under 5 W.

3.3.4 The Confinement

The GEC RF reference cell is constructed of a stainless-steel chamber containing two parallel plate electrodes. A capacitively coupled discharge occurs between these two electrodes when the proper power is supplied. In the original GEC reference cell design, the upper electrode consisted of a disk with holes in it in a “showerhead” pattern allowing gas to be introduced into the system. For the purpose of observation and access to the discharge region between the two electrodes from the top flange, the GEC cell used here has the showerhead upper electrode replaced by a cylindrical ring electrode. This electrode is insulated from the chamber by a Teflon disk, allowing it to be powered, grounded or biased separately from the main chamber. In the experiments in this dissertation, the upper electrode is always grounded through connection to the main chamber via a ground strap. The diameters of the two electrodes are 8 cm and the electrode interspacing is fixed at 2.20 cm.

The lower electrode in the standard GEC RF reference cell is a flat stainless-steel air-cooled disk, powered by a radio frequency generator at 13.56 MHz through a matching network. Dust particles levitating over the lower electrode move at thermal velocity or are repelled by other charged particles through Coulomb forces. Over a period of time, these particles move away from the lower electrode and are lost. To constrain the particles within the discharge region, a horizontal force is required. For this purpose, various diameter plates having a central cutout [Chu 1994; Hebner *et al* 2003] or a glass box [Arp *et al* 2004] are placed on the lower electrode in order to provide a horizontal confining force.

In this dissertation, glass boxes are implied to provide confinement force. A Glass box can help to control the number of the dust particles and offer confinement with different ration between the horizontal and vertical direction. Three types of glass box are used in our experiments, as shown in Fig. 3.7. Different sizes of the box can provide different confinement and plasma environment within the box, which will be discussed in Chapter Four and Five.

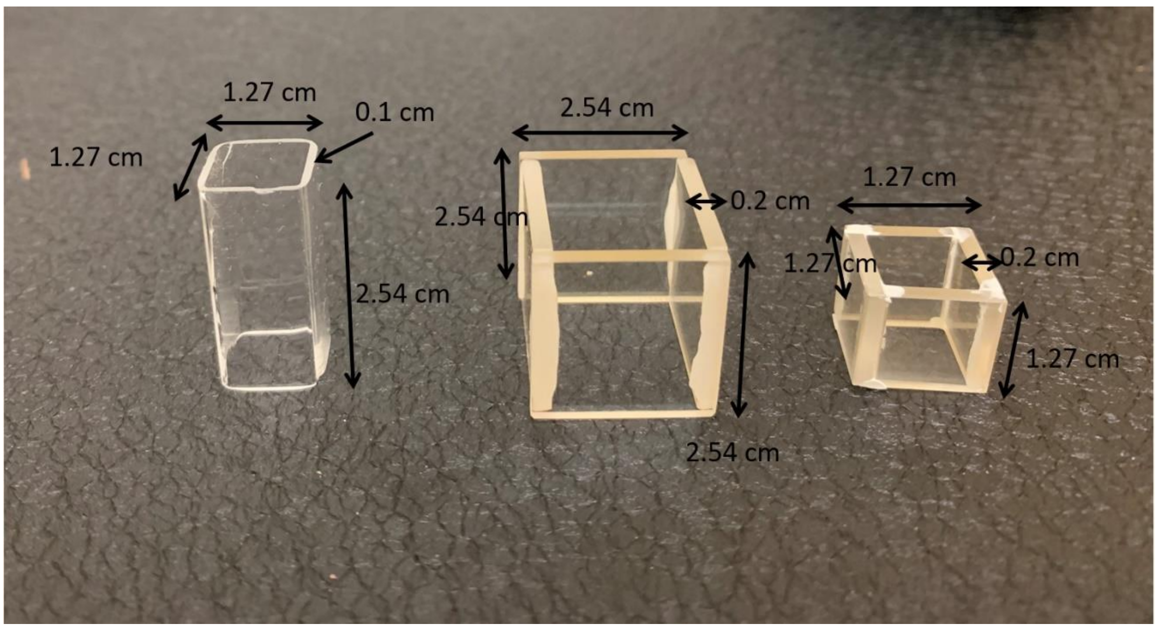

Figure 3.7. The glass boxes used in the experiments.

3.3.5 RF Power System

To generate a low amplitude RF signal ($\leq 1\ V_{rms}$), a signal generator (Hewlett-Packard 8657A) is employed with the frequency held at 13.56 MHz. Post signal generator, the signal is sent to a VPA (variable passive attenuator) where the signal is increased by 11-31 dBm at a maximum of $1\ V_{rms}$ as controlled by a variable resistor knob. An RF power amplifier (EIN (Electronic Navigation Industries) 420 L) having a 50 Ω load is used to amplify the signal from the VPA by approximately 48 dB. Next, the signal is transferred to a tuning network which is necessary to prevent damage to in-line devices (for example, the signal generator and power amplifier) due to reflection of the signal resulting from possible impedance mismatch between the components of the RF system. In such a case, as the impedance mismatch increases, the amplitude of the reflected signal increases. Thus, the tuning network must be used when running a high voltage signal ($> 1\ V_{rms}$). In the case of low voltage signal application, the RF power amplifier and tuning network can be bypassed. The tuning network used here is constructed of two variable capacitors on the powered side of the circuit with one variable capacitor and a constant inductor from power to ground; this results in the tuner capacitively connecting the RF power amplifier to the shunt network, preventing DC current from passing between the amplifier and the shunt. Once a plasma is generated and becomes stable, the tuning network is adjusted to minimize power reflection; this is always set to be less than 10% in the CASPER GEC RF reference cell. Detailed information concerning the entire RF setup can be found in Smith 2005.

3.3.6 DC Bias

Since the dust particles are located above the lower electrode in a laboratory RF discharge plasma, the application of a variable DC bias on the lower electrode can be used as an effective tool for experimental investigation in dusty plasma research [Schollmeyer *et al* 1999]. To fully employ this advantage, a DC power supply is inserted in the RF power system, allowing the DC bias on the lower electrode to be modulated in a controlled manner. To minimize power dissipation and current flow in the DC power supply, a network with a 15 kΩ resistor is placed in series with the DC power supply. The location of the DC power supply must always be on the cell side of the tuning network, since this has a blocking capacitor protecting the RF power source and RF power amplifier from possible damage which can be caused by the DC bias.

3.3.7 Dust Particles

In the experiments discussed here, micrometer-sized spherical melamine formaldehyde (MF) dust particles were introduced into the plasma by physically agitating a dust container fixed above the upper electrode. The diameter of the particals varies from 2 to 11 \mum in diamters and the dust particles with a diameter of 8.89 \mum are used most often. Melamine formaldehyde has many advantages, such as being hard and durable and having good heat resistance, which allow the particles to maintain their size in experiments of long duration. The density of MF dust particles is 1.516 g/cm^{-3}.

All the following experiments are conducted under the system described above. Any small modification will be discussed in Chapter Four and 5.

CHAPTER FOUR

Experimental Measurement of Plasma Sheath Profiles and Overlapped Plasma Sheaths

4.1 Introduction

The properties of the plasma sheath have attracted interest since the sheath was defined by Tonks and Langmuir more than one hundred years ago. The intermedia between plasma and any material immersed in plasma is defined as the plasma sheath and therefore, in almost all fields within material industry, such as material deposition, surface treatment and ion implement, the investigation of properties of the sheath is considered a crucial task. In particular, the space–charge sheath region adjacent to the electrode surfaces has been the subject of much investigation [Klick 1997, Sobolewski 2000]. As the ions required for the etching of semiconductors receive their energy from the fields within the sheath, a knowledge of the spatial variation of these fields is important to allow for the best design of the manufacturing process. Multiple sheath models have been proposed [Bornig 1992, Libermann 2005, Edelberg 1999], but their predictions are often contradictory and have rarely been tested experimentally.

In this Chapter, several experimental diagnostic methods for establishing the plasma sheath as well as their advantages and disadvantages will be introduced. An over view will be given in Section 4.2, while in section 4.3 a novel technique, the particle-freefall method will be described. The diagnostic results for a standard sheath created by a planar surface will be shown in Section 4.4 with the measurements of representative overlapped sheath presented in Section 4.5.

4.2 Overview of Experimental Diagnostic Methods for the Plasma Sheath

4.2.1 Langmuir Probe

Langmuir probe theory is still mainly based on the first paper from Langmuir [Langmuir 1926] who described the currents collected by different kinds of biased probes (plane, cylindrical, and spherical) in a potential well. The mechanisms are generally based on the Orbital Motion Limit (OML) theory and the Allen-Boyd-Reynolds (ABR) theory, specially for the cylindrical probe [Allen 1957].

A short explanation of the mechanics of a Langmuir probe can be given by assuming a wire inserted into a plasma. Instead of changing to the plasma potential (V_p) it instead charges to a negative potential (i.e., the floating potential: $V_f < V_p$) retarding the electron current enough so that it matches the ion current. At this point, an equal flow of electrons and ions—zero net current— is achieved and charging stops. Whenever the wire is held at potentials above or below V_f, a net current will flow into the plasma (positive current: plasma electrons attracted to the probe), or out from the plasma (negative current: plasma ions attracted to the probe). Through applying different biases on the probe, the famous I-V characteristic graph can be obtained, from which the electron temperature, electron/ion density and the plasma potential around the probe can be calculated. Fig. 4.1 shows a typical Langmuir probe and I-V characteristic graph.

(a)

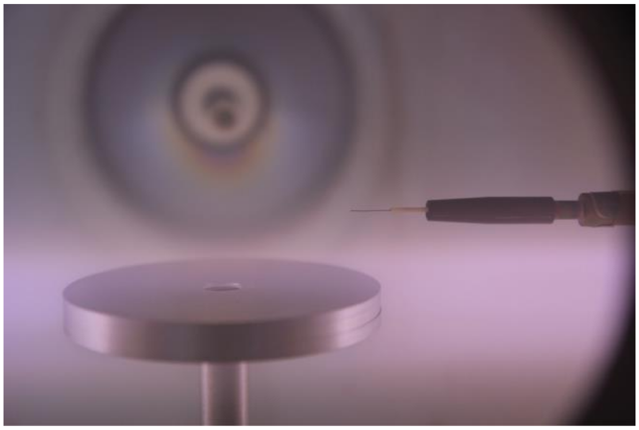

(b)

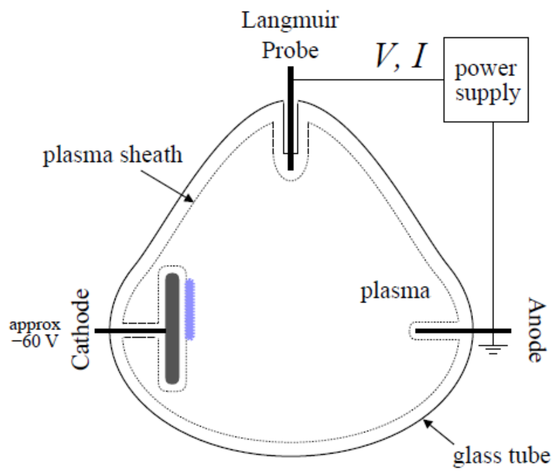

(c)

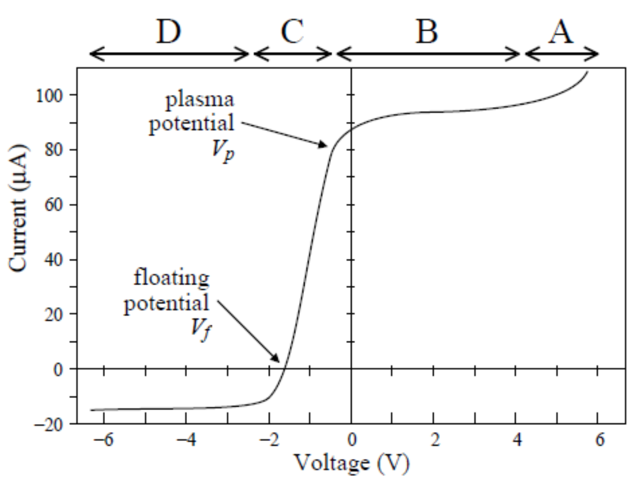

Figure 4.1. Photo of (a) and simple schematic (b) of a Langmuir probe (Faudot 2019); (c) a typical I-V characteristic (Chen 1984).

In the region shown in Fig. 4.1 (c) and labeled A to D, different plasma parameters can be observed:

A. When the Langmuir probe is well above the plasma potential it begins to collect some of the discharge current, essentially replacing the anode.

B. When the probe is at the plasma potential (left side of region B), the probe does not exhibit a plasma sheath, and the surface of the probe collects ions and electrons that hit it. In this case, the electron current is much larger than the ion current, so at V_P the current is approximately

$$I_P = \frac{1}{4} e n_e A \left[\frac{8 k_B T_e}{\pi m_e}\right]^{1/2}, \tag{4.1}$$

where *A* is the area of the probe while the other variables have the same meaning mentioned in Chapter Two. For $V > V_P$, a sheath forms, effectively expanding the collecting area. Thus, the probe current increases slightly before approaching equilibrium in this region.

C. When the Langmuir probe's potential falls below Vp, the probe begins to repel electrons. As a result, only electrons with sufficient kinetic energy can hit the probe. In this region, the probe current is equal to

$$I = e n_e A \left[\frac{k_B T_e}{2\pi m_e}\right]^{1/2} \exp\left[-\frac{e(V_P - V)}{k_B T_e}\right]. \tag{4.2}$$

For $V \ll V_P$, very few electrons have the required velocity needed to intersect the probe. At $V = V_f$, the electron current has been suppressed to the extent that it equals the ion current. (The ion current is always present in region C, but typically for $V > V_f$, it is "negligible" in comparison to the electron current.)

D. In this region the probe exhibits a well-developed sheath repelling all electrons with ions that random-walk past the sheath boundary collected by the probe. Since the sheath area is only minimally affected by the probe voltage, the collected ion current is approximately constant and can be given by,

$$I \approx \frac{1}{2} e n_i A u_B, \tag{4.3}$$

where u_B is the Bohm Speed.

Generally speaking, the Langmuir probe is the most widely used plasma diagnostic method providing a convenient mechanism for diagnosing the plasma bulk. Unfortunately, the Langmuir probe will not work properly in either the sheath or presheath region. Fig. 4.2 shows the equipotential contours near a Langmuir probe inserted in a sheath. It can be easily seen that biasing the probe results in large perturbations to the sheath structure and that the resultant electron saturation current will provide the bulk electron parameters rather than the local sheath/presheath parameters. Another issue is that Langmuir probes tend to short out when placed in the sheath.

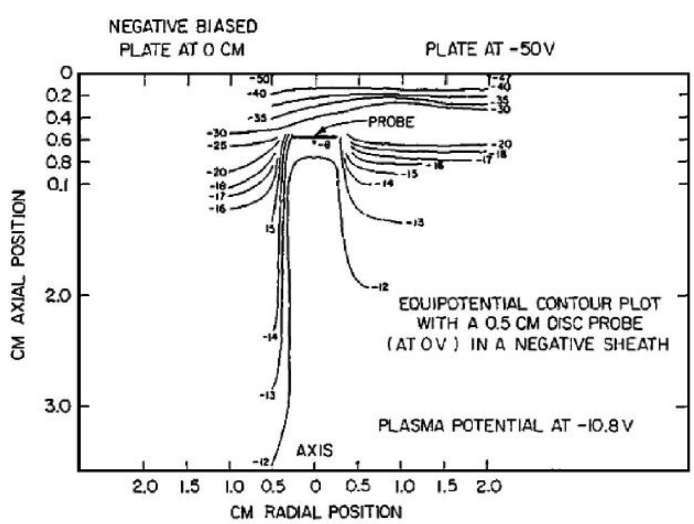

Figure 4.2. Equipotential contours near a 0.5 cm diameter planar Langmuir probe biased at 0 V. The probe was positioned 0.6 cm from a plate biased at −50 V (Coakley 1980).

4.2.2 Emissive Probe

The first concept of an electron-emitting probe was proposed by Langmuir in 1923, at the same time he proposed the Langmuir probe. Collecting probes determine plasma potential by identifying the 'knee' in the I-V characteristic curve. Emissive probes, however, determine the plasma potential more precisely due to its special mechanism. When an emitting probe is biased more negatively than the plasma potential, the electrons can be emitted from the probe into the plasma. When an emitting probe is biased more positively than the surrounding plasma potential, electrons are no longer emitted, except for a small number of electrons residing in the tail of the emitted electron distribution. Fig. 4.3(a) provides a schematic of an emissive probe and (b) shows the resulting I-V curves measured at specific wire temperatures $T_{W.}$ At low bias voltages, the emitted current is space charge limited and can be described by the Child–Langmuir law. For higher negative bias voltages to the probe, the emitted current is best described by the Richardson–Dushman equation. Although a emissive probe exhibits less perturbation and higher resolution than does a regular Langmuir probe, when it is immersed into the sheath region, it will still destroy the sheath environment due to thermal heat and secondary electron emission.

(a)

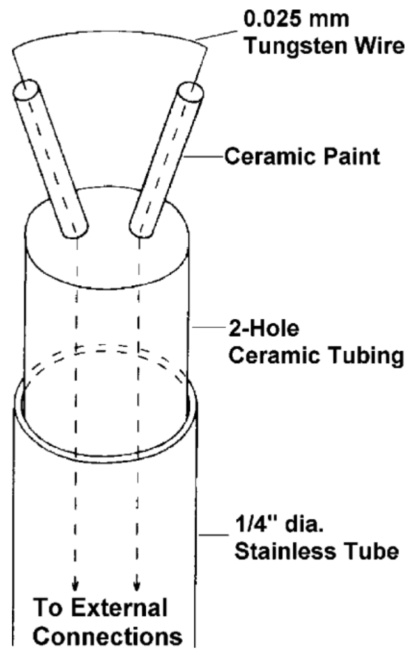

(b)

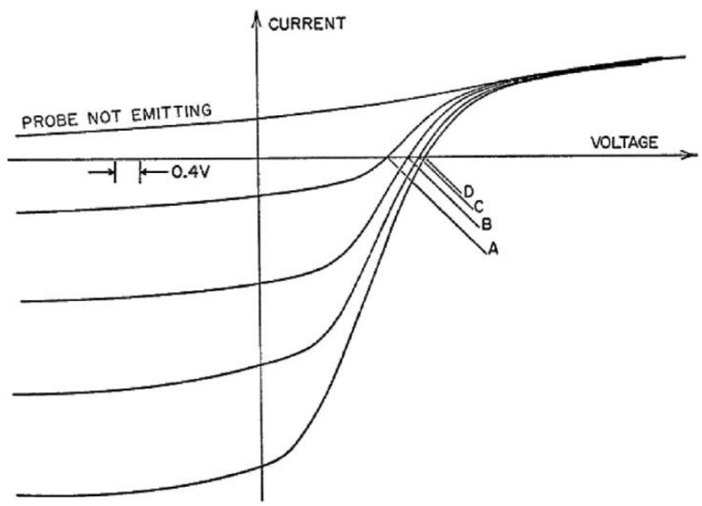

Figure 4.3. (a) One version of the hairpin design of an emissive probe; (b) Experimental emissive probe I-V curves at varioust wire temperature (A-D) (Hershkowitz 2005).

4.2.3 Laser-based Techniques

Doughty and Lawler [Doughty 1984] made spatially resolved measurements in the cathode sheath of a dc glow discharge using a technique based on the linear Stark effect in Rydberg states of helium: the optogalvanic effect was used to detect the transition from a helium metastable level to the Stark split Rydberg levels as a dye laser was scanned through the transition. These measurements indicated a linear field variation across the cathode fall, from a maximum at the cathode surface to essentially zero at the interface with the positive column. Using a different approach, Goeckner *et al.* [Goeckner 1992] have used laser induced fluorescence (LIF) and the Doppler Effect to measure the velocity profile of metastable argon ions in a dc plasma sheath. Moore *et al.* [Moore, 1984] used a LIF technique which exploited the Stark mixing of excited levels in the molecule BCl. The ratio of intensities of forbidden and allowed fluorescence lines from laser excited levels provided an absolute measure of the electric field. Using this technique, Moore *et al.* were able to carry out spatially resolved measurements of the electric field in the rf sheath of a capacitively coupled rf discharge at specific times during the rf cycle. Bowden *et al.* [Bowden 1995] measured the spatial distribution of the average electric field in a rf sheath in helium by detecting the fluorescence from levels excited by collisional transfer from laser excited Rydberg levels. Recently, in a much more complete investigation, Czarnetskii *et al.* [Czarnetskii 1999] used LIF techniques to make spatially and temporally resolved measurements of electric fields in rf sheaths in helium and hydrogen. Another LIF technique for sheath field measurements, used by Takiyama and coworkers [Takiyama 2001], relies on Stark mixing in helium which perturbs laser excited forbidden transitions from the singlet metastable level, with the consequence that the fluorescence intensity and its polarization become functions of the electric field. This technique has been extended to investigating sheaths in the presence of strong magnetic fields [Wanatabe 1999].

While laser-based techniques have allowed many successful studies of sheath structure to be carried out, these techniques require sophisticated equipment, often use discharge arrangements specifically designed for the purpose, and rely upon the presence of specific atomic or molecular species. Such techniques also involve complicated diagnostic procedures and are possible for only a small number of parameters sets. In other words, they can only rarely be used in applications. Therefore, they are generally not suitable for routine measurements or for monitoring the sheath.

4.2.4 Dust Particle as Probe

Samarian [Samarian 2005] first conducted sheath profile measurements using dust particle as probes. The technique employed was based on the measurement of the equilibrium position and resonant oscillation frequencies of dust particles immersed in the plasma. The resonant oscillation frequency of a dust particle ω is given by,

$$\omega = \sqrt{Q_d E'/m_d}\ , \qquad (4.3)$$

where E' is the gradient of the electric field, Q_d and m_d are the charge and mass of the dust particle, respectively. This frequency can be measured through a method in which a dust particle levitated in the sheath is displaced from its equilibrium position by applying a negative voltage to the electrodes or irradiating the particle using a laser beam.

For micrometre-sized particles the force balance is dominated by the electric and gravitational forces

$$EQ_d = m_d g. \qquad (4.4)$$

Combining Eq. 4.3 and 4.4, the resonant frequency can be expressed as

$$\omega = \sqrt{\frac{gE'(z)}{E(Z)}}. \tag{4.5}$$

Eq. 4.5 provides the recurrent equation for the electric field near the particle levitation position,

$$\ln E(z) = \ln E(z + \Delta z) - \frac{\omega^2(z)}{g}\Delta z. \tag{4.6}$$

Since different size dust particles levitate at different heights, Samarian measured ω for various size dust particles near their equilibrium positions and then used Eq. 4.6 to develop the rough electric field profile in the sheath, as shown below in Fig. 4.4.

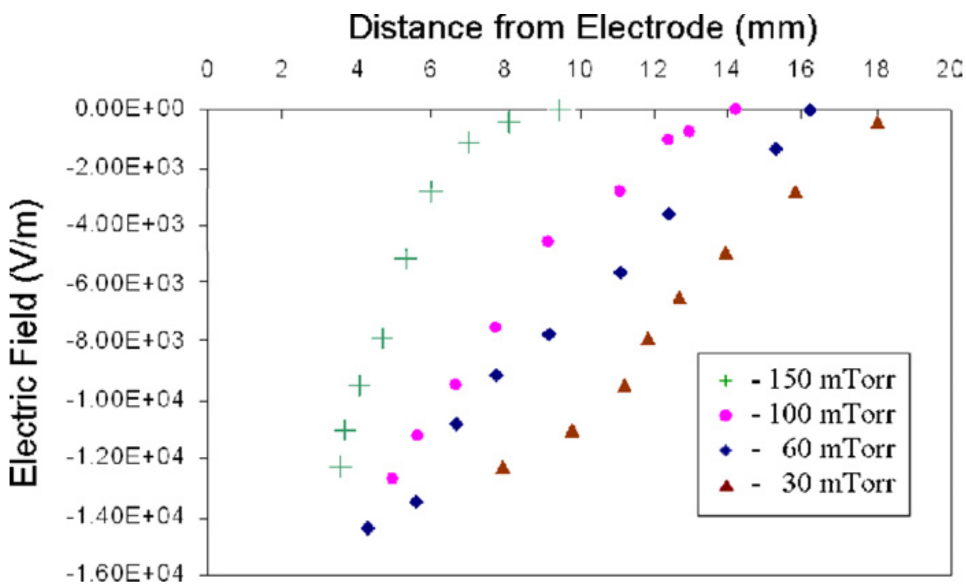

Figure 4.4. Sheath electric field profile at different pressures (Samarian 2005).

As can be seen, the dust particles behave as minimally perturbative electrostatic probes allowing measurement of plasma parameters with good spatial resolution. The technique is relatively simple as the necessary measurements are the position of the particle and its motion after perturbation. As such, simple access to the discharge, for illumination of the particle and recording its motion, is all that is required. The diagnostic is simple to set up and maintain, making it possible. The technique is also suitable for measurement in deposition devices. Unfortunately, this technique can only provide information for the dust particle levitating position employed. Given the difficulty of having many different size dust particles in the equipment, this limits the spatial resolution which can be obtained.

4.3 Freefall Particle Technique

In the remained of this Chapter, we will present a new measurement technique which exhibits both minimal perturbation and good spatial resolution. In this technique, a few hundreds of dust particles were dropped from a dust dropper located above the upper electrode into the sheath, with individual particle motion recorded at 1000 fps. A MATLAB-based algorithm for particle detection was employed to identify the particles in each frame of the data collected, which were then linked using the Hungarian algorithm [Kuhn 1955].

The resulting particle trajectories were examined to eliminate any faulty data. Trajectories exhibiting discontinuities in their calculated accelerations were removed as were trajectories exhibiting minimal particle movement, since both of these are usually associated with noise falsely interpreted as particles. Particle-particle interactions were managed by establishing a minimum allowable distance between detected particles. For this case, it was 1 mm.

Based on the first and second order difference quotients for the trajectories of the particles, the velocities and accelerations in both the vertical ($\dot{Z}, \ddot{Z}$) and horizontal ($\dot{X}, \ddot{X}$) directions were determined. Assuming that only gas drag, confining electrostatic forces and gravity are acting on the particles, the equations of motion are given by

$$m_d\ddot{Z} = \beta\dot{Z} + Q_d E_z - m_d g \tag{4.7}$$

$$m_d\ddot{X} = \beta\dot{X} + Q_d E_x \tag{4.8}$$

where m_d is the mass of the dust particle, g is the acceleration due to gravity, Q_d is the charge on the dust particle, and E_z and E_x are the electric fields in the vertical and horizontal directions. Since the ion drag force is small compared to the confinement force and no external thermal gradient is applied to the system, the ion drag and thermophoretic forces may be considered negligible [Fortov 2004] and then not included. In Eqs. 4.7 and , β is defined as

$$\beta = \delta \frac{4\pi}{3} a^2 N m_n \bar{c}_n \tag{4.9}$$

where ɑ is the radius of the dust particle, *N* is the neutral gas number density, m_n is the mass of the neutral gas atoms (Argon), and the coefficient δ accounts for the microscopic mechanism governing collisions between the gas atom and the surface of the dust particle. For the experiments conducted in this dissertation, with melamine formaldehyde (MF) particles and Argon gas, δ has been determined to be 1.44 as reported in (Land 2010). Finally, $\bar{c}_n$ is the thermal speed and defined as

$$\bar{c}_n = \sqrt{\frac{8kT}{\pi m_n}} \tag{4.10}$$

where *k* is the Boltzmann constant and *T* is the temperature.

Eqs. 4.9 and 4.10 yield a value for β = 9.26×10^{-12} N m^{-1} s. This coefficient was also measured experimentally, giving β = (9.77 ± 2.56)×10^{-12} N m^{-1} s, in good agreement with the analytical value. The analytical value was used in all following calculations.

Employing this result and using Eq. 4.7 and 4.8, the electrostatic forces, $Q_d E_z$ and $Q_d E_x$, in the vertical and horizontal directions can now be calculated. For convenience, this data was recorded as the vertical and horizontal acceleration $Q_d E_z / m_d$ and $Q_d E_x / m_d$.

The image analysis method mainly comes from a Matlab based program "Simple Tracker" by Jean-Yves Tinevez.

Particle tracking consist in re-building the trajectories of one or several particles as they move in time.

Links are first created between each frame pair, using the Hungarian algorithm. Links are created among particle pairs found to have the closest (Euclidean) distance. By virtue of the Hungarian algorithm, it is ensured that the sum of the pair distances is minimized over all particles between two frames. Meanwhile, the code also defines a maximal value in particle linking. Two particles will not be linked (even if they are the remaining closest pair) if their distance is larger than this value.

The Hungarian algorithm has been long time used to solve the assignment problem. It was developed and published in 1955 by Harold Kuhn, who gave the name "Hungarian method" because the algorithm was largely based on the earlier works of two Hungarian mathematicians: Dénes Kőnig and Jenő Egerváry.The following steps shows that how to use the Hungarian method.

Step 0: Create an n$\times$m matrix called the cost matrix in which each element represents the cost of assigning one of n workers to one of m jobs. Rotate the matrix so that there are at least as many columns as rows and let k=min(n,m).

Step 1: For each row of the matrix, find the smallest element and subtract it from every element in its row. Go to Step 2.

Step 2: Find a zero (Z) in the resulting matrix. If there is no starred zero in its row or column, star Z. Repeat for each element in the matrix. Go to Step 3.

Step 3: Cover each column containing a starred zero. If K columns are covered, the starred zeros describe a complete set of unique assignments. In this case, Go to DONE, otherwise, Go to Step 4.

Step 4: Find a noncovered zero and prime it. If there is no starred zero in the row containing this primed zero, Go to Step 5. Otherwise, cover this row and uncover the column containing the starred zero. Continue in this manner until there are no uncovered zeros left. Save the smallest uncovered value and Go to Step 6.

Step 5: Construct a series of alternating primed and starred zeros as follows. Let Z_0 represent the uncovered primed zero found in Step 4. Let Z_1 denote the starred zero in the column of Z_0 (if any). Let Z_2 denote the primed zero in the row of Z_1 (there will always be one). Continue until the series terminates at a primed zero that has no starred zero in its column. Unstar each starred zero of the series, star each primed zero of the series, erase all primes and uncover every line in the matrix. Return to Step 3.

Step 6: Add the value found in Step 4 to every element of each covered row, and subtract it from every element of each uncovered column. Return to Step 4 without altering any stars, primes, or covered lines.

DONE: Assignment pairs are indicated by the positions of the starred zeros in the cost matrix. If C(i,j) is a starred zero, then the element associated with row i is assigned to the element associated with column j.

4.4 Experimental Results for the Sheath of a Planar Electrode

The experiments discussed below were conducted in the Equipment described in Chapter Three. In this case, the dust particle size was 8.89 micro meter in diameter. Experimentally measured results for the vertical electric field force profiles in the sheath of the planar lower electrode are shown in Fig. 4.5, which compares the effects of changing rf power (Fig. 4.5a) and changing gas pressure (Fig. 4.5b). Note that all forces here and elsewhere in this paper are normalized by the gravitational force acting on the dust particle.

As a dust particle enters the sheath from the plasma bulk above, the vertical electric force rapidly increases from zero as the magnitude of the electric field increases with the gradient of the force curve decreasing as the particle approaches the lower electrode. This is due to the fact that the electron density drops quickly near the lower electrode, leading to a reduced magnitude of charge on any individual dust particle (Douglas 2001).

In the plasma bulk, the electrostatic force acting on the dust particles should be almost zero. The results shown in Fig. 4.5 can therefore be used to establish the sheath width s0, the distance above the lower electrode separating the sheath and presheath from the plasma bulk (Bohm 1949). In the graph below, we define the sheath width as the first point above the lower electrode (Z=0), where the force curve becomes zero. It should be noticed that the electric field force in the region above the cross point is not identically

zero, but this is inside the error bars of this measurement technique, which is about $\pm 0.05\ m_d g$.

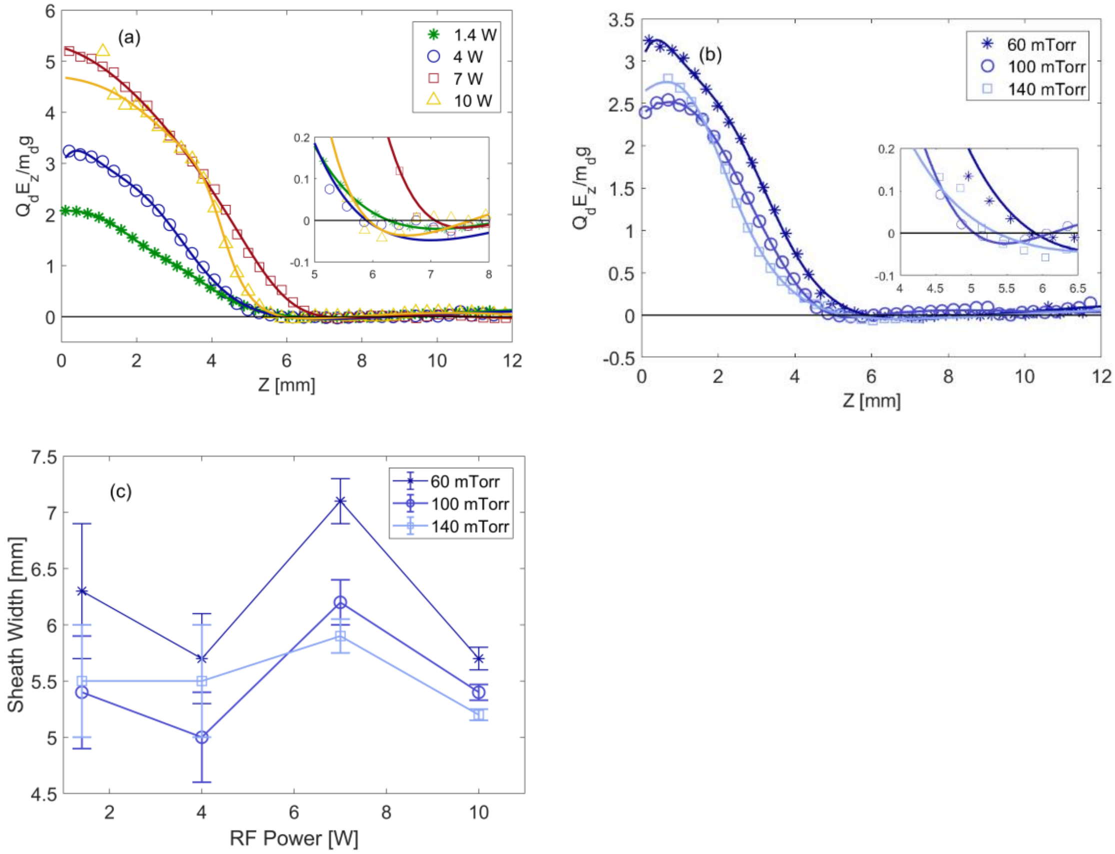

Figure 4.5. Vertical electrostatic force acting on dust particles levitated in the sheath above the lower powered electrode as a function of distance (Z) from the lower electrode for (a) varying rf powers and fixed gas pressure of 60 mTorr and (b) varying gas pressures for a fixed rf power of 4 W. The symbols indicate measured data points while the lines indicate a rational fit. The inserts show a detailed view of the region where the vertical force goes to zero, marking the sheath width. (c) Sheath widths determined for different powers and gas pressures.

As shown in Fig. 4.5(c), the sheath width is only weakly related to the plasma power. The largest sheath width observed across all gas pressures occurred at 7 W, although the differences between the sheath widths measured at all other powers fell within the error bars. The reason why this particular sheath exhibited a different sheath width at a power of 7 W is still unknown. The sheath width was observed to be largest at a gas pressure of

60 mTorr, although no significant differences between sheath widths was observed for pressures of 100 mTorr and 140 mTorr.

4.5 Experimental Results for Overlapped Sheaths

A proper understanding of the physics underling the production of the plasma sheath is vital to the plasma processing industry. Processes such as plasma enhanced deposition, etching, and plasma immersion ion implantation, are all conducted in the plasma sheath with the sheath electric field determines the ion densities and dynamics. The target geometry is often complicated, with a trench-like geometry being the most widely used [Chu 1996]. The sheath produced by a trench (see Fig. 4.6) geometry will in general fit one of three different types depending on the sheath width in relation to the trench width W and depth D. As shown in Fig. 4.6a, a sheath width much smaller than the width of the trench $s_0 << W$ allows the plasma edge to conform to the shape of the surface topography, a feature known as plasma molding [Kim 2003]. As shown, there is no overlap between the sheaths formed by the different surfaces of the trench. When the sheath width is comparable to the width $s_0 \approx W$, the sheaths produced at the walls of the trench begin to overlap (Fig. 4.6b). Compared with case (a), the edge of the sheath is raised from the trench floor or even pushed out of the trench. When the sheath width s_0 is much larger than the width $s_0 >> W$, the sheaths of the two opposing walls completely overlap (Fig. 4.6c). The sheath edge is almost planar, as it would be if there were no trench. It should be noted, that in most researches, the overlapping is considered to be happened between the sheaths of the upper steps, instead of the sheaths of the surfaces in the trench.

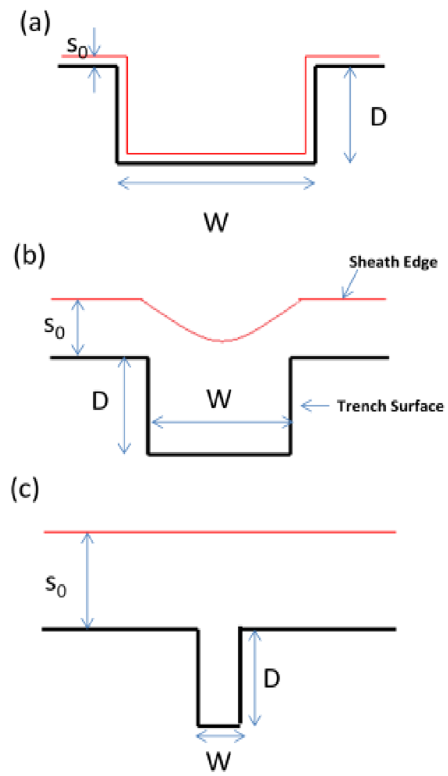

Figure 4.6. Schematic of a typical plasma sheath produced by a trench with width W and a depth D. The geometry of the sheath boundary, indicated by the red line, depends on the sheath width s_0 in relation to the trench width, W.

There are a few simulation results for the sheath profiles inside the trench like structure. Kim et. al [Kim 2003] used fluid model and molecular cell method to simulate the electric field inside the trench structure, the results are shown in Fig 4.7.

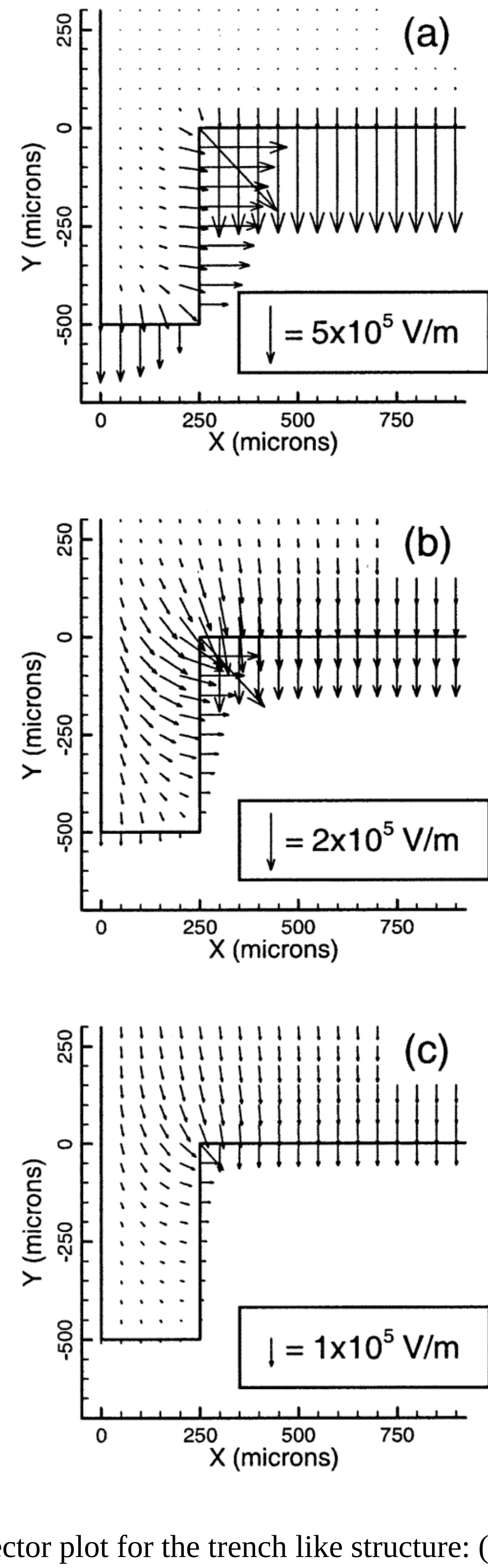

Figure 4.7. Electric field vector plot for the trench like structure: (a) $s_0/D = 0.216$; (b) $s_0/D = 0.936$; (c)$s_0/D = 2.562$. (Kim 2003)

However, experiments mapping the sheath profile produced inside a trench and for overlapping sheaths are rare. In an experiment reported by Sheridan [Sheridan 2017], the overlapping is considered to be due to the sheath of the top surfaces of the opposite trench steps. To data, there have been no experimental measurements inside a trench. In this Section, the freefall particle technique is used to map the sheath electric field in the vertical direction as a function of the changing sheath width, which is altered by varying the plasma operating power and pressure. A glass box (consisting of insulating walls and a conductive substrate or electrode) is employed to simulate a trench geometry.

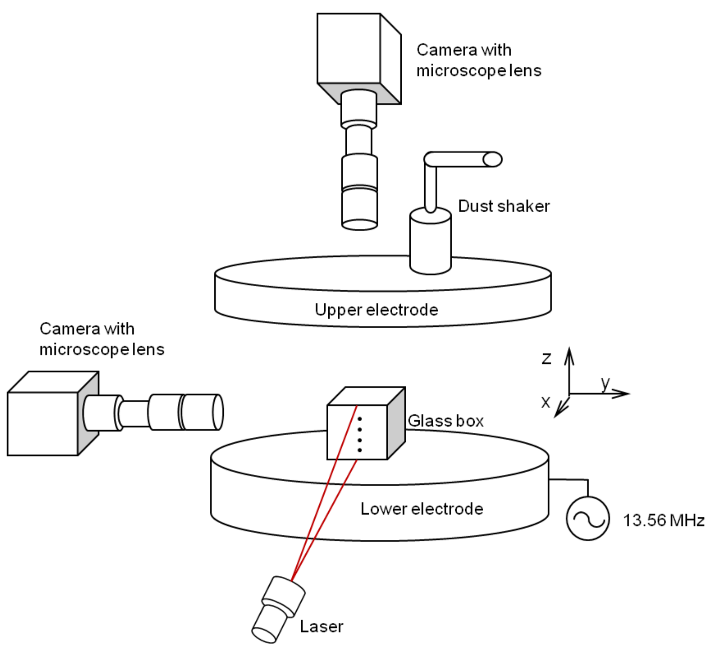

Figure 4.8. Experimental setup. The upper ring electrode is grounded while the lower electrode is powered. The open-ended glass box shown has outer dimensions of 2.54 cm × 2.34 cm × 2.34cm (height, width, length) is placed on the lower powered electrode. The motion of the particles is captured using a Photron CCD high speed camera (side view).

The measured electric force at the center line of the glass box is compared with the electric force measured above a planar lower electrode in Fig. 4.9. At the lowest gas pressure P = 60 mTorr, the vertical electric force profile within the box can be seen to be quite different from that measured within the sheath above the planar electrode. The profiles of the vertical electric force above the planar electrode, indicated by dashed lines in Fig. 4.9 (a), show that the electric force acting on the dust particles continuously increases as the particles approach the lower electrode, flattening out very close the electrode surface (usually less than 0.5 mm above the lower electrode). Inside the box, the point marking the sheath width, where the vertical electric field force is approximately equal to zero, is much further from the lower electrode than without the box. Overall a large vertical extent, the gradient of the electric force is relatively small, or even becomes negative. This leads to a relatively ‘flat’ region indicated by the shaded region in the electric force profile as shown in Fig. 4.9(a), which is not observed in the planar sheath cases. The extent of the flat region decreases with increasing rf power. At the lowest operating power (1.4 W) the length of this flat region is much larger than the sheath width measured for the planar electrode. At fixed operating powers, as shown in Fig. 4.9(b), increasing the gas pressure leads to a convergence between the force profiles observed within the box and those observed above the lower planar electrode. The ‘flat’ region disappeared at 100 and 140 mTorr gas pressure.

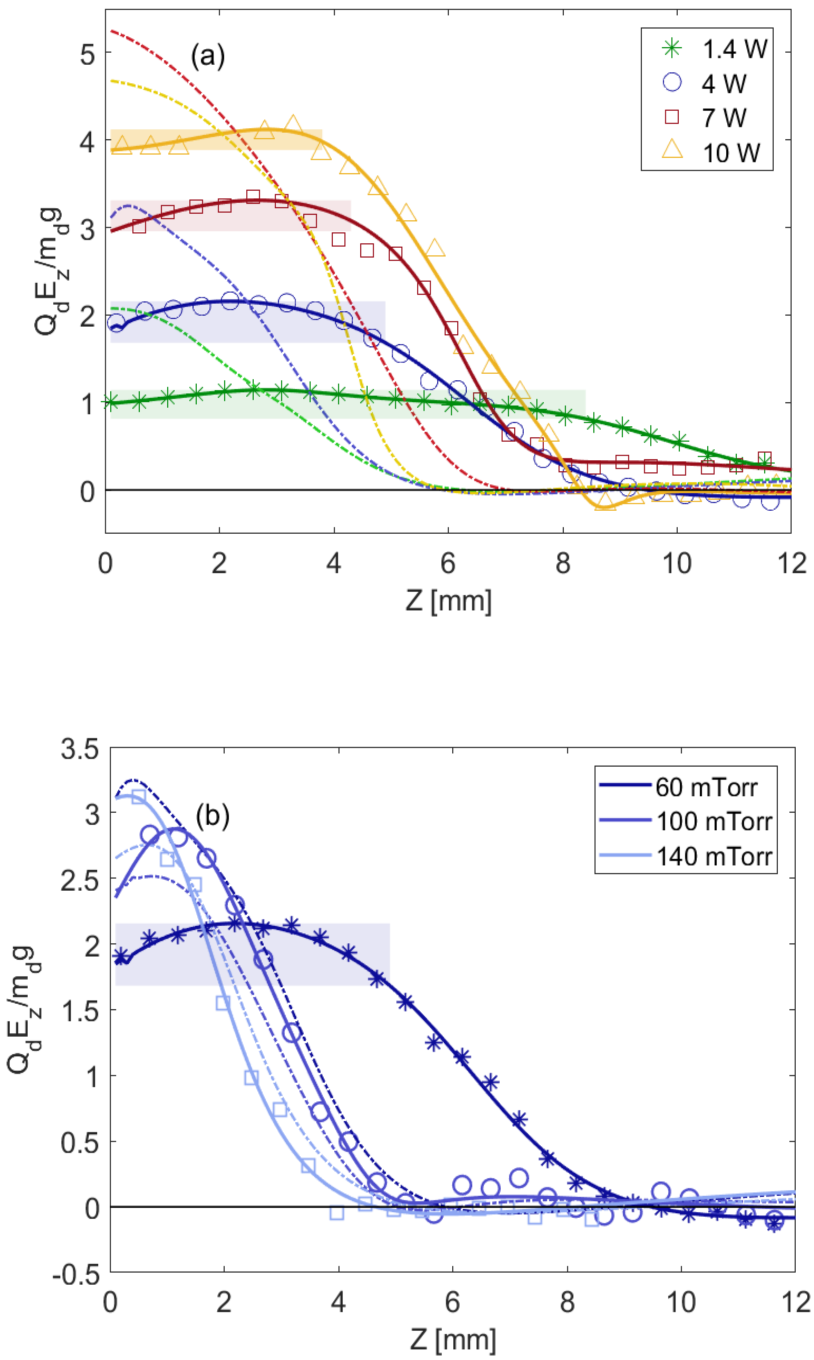

Figure 4.9. Comparison of vertical electric field force in the sheath of the lower planar electrode and inside the box for (a) varying rf powers at a fixed gas pressure of 60 mTorr and (b) varying gas pressures for a fixed rf power of 4 W. Symbols show the measured data points, the solid line indicate the corresponding fit and the dash line show the fits from the data shown in Fig. 4.5.

Fig. 4.10 (a) shows a 2-D map of the horizontal electric field force for the lowest pressure and power (60 mTorr gas pressure and 1.4 W rf power). Fig. 4.10(d) shows the 1-D profile of the horizontal electric force at the vertical position marked by the red line in Fig. 4.10(a). At this height, the horizontal electric force is almost linear across the region [-7 mm to 7 mm], indicating that the horizontal force from the walls is felt across the entire region and the sheaths of the glass walls overlap with one another. The map shown in Fig. 4.10(b) corresponds to the plasma conditions for the case where there is a small flat vertical force profile. At positions near the lower electrode, indicated by the red line in Fig. 4.10(b), the horizontal electric force is nearly linear across the width of the box, as shown by the corresponding 1-D profile in Fig. 4.10(e). This leads to the conclusion that the sheaths from the walls are overlapping in this region. At distances farther from the lower electrode, as indicated by the blue horizontal line in Fig. 4.10(b), the corresponding1-D profile is nearly flat cross the center of the box, increasing rapidly in magnitude only very close to the walls. This shows that the sheaths from the vertical walls are well-separated at this height. Finally, a horizontal electric force map is shown in Fig. 4.10(c) for an operating condition where the vertical electric force profile within the box is similar to that above the planar lower electrode. The horizontal electric field is nearly zero throughout the entire box region, only having significant non-zero magnitude in the corners of the box very close to the lower electrode surface.

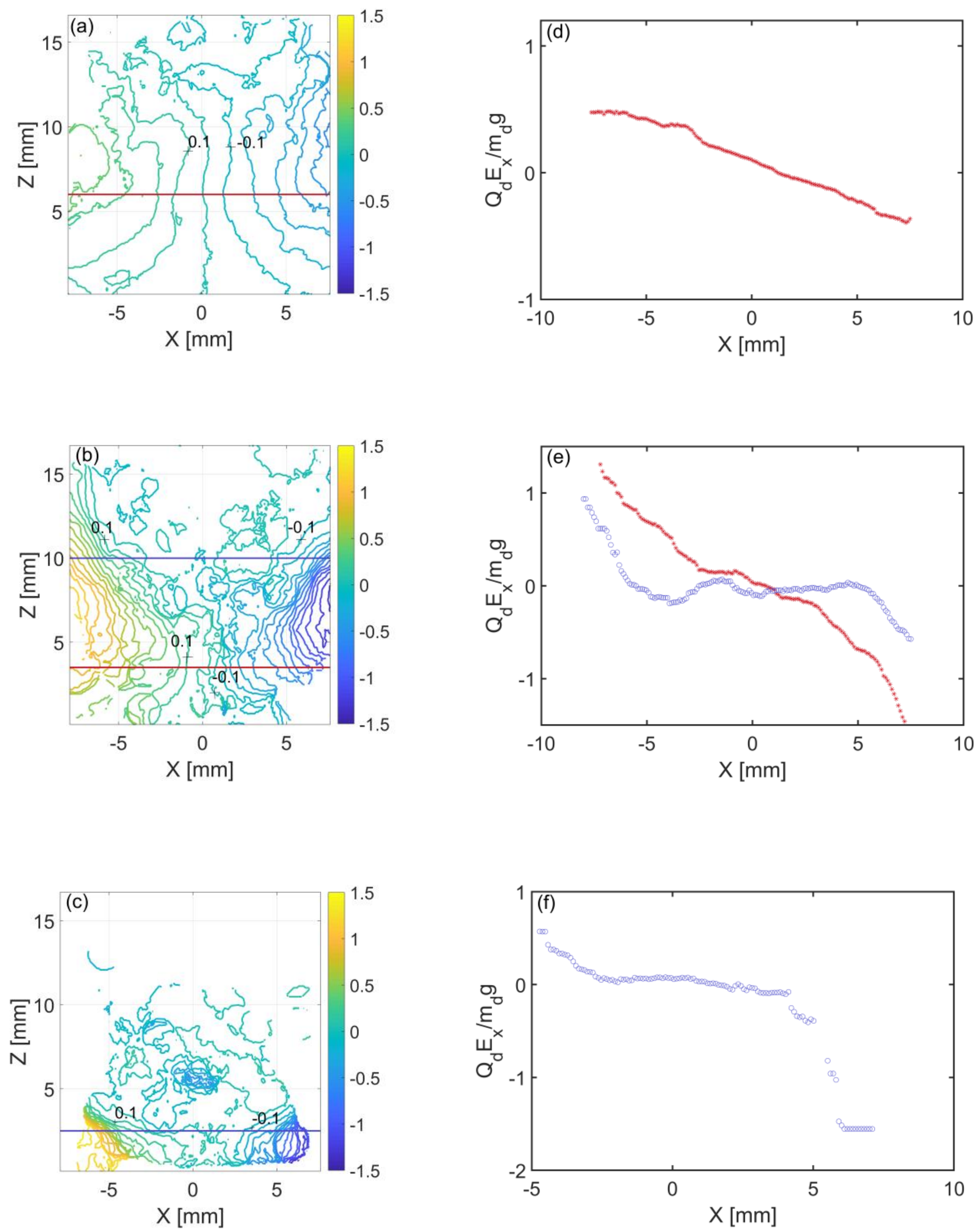

Figure 4.10. The horizontal electric field force acting on the dust particles within the box at (a) 60 mTorr gas pressure and 1.4 W rf power; (b) 60 mTorr gas pressure and 4 W rf power and (c) 140 mTorr gas pressure and 4 W rf power. The colorbar indicates the magnitude of the electrostatic force normalized by the force of gravity, with positive forces acting to the right. (d-f) Variation of horizontal electric force at the vertical positions marked by the horizontal lines in (a-c), respectively.

The region where overlapping between the sheaths of the inner surface of the glass box can be identified from the data shown in Fig. 4.10. The sheath overlap is indicated by the differences between the profiles of the horizontal electric field in the regions marked by the blue and red lines in the force maps. In the region where the sheaths overlap, the contour line indicating $\frac{Q_d E_x}{m_d g} = 0$ exists only in the middle of the box (X = 0) with the contour lines marking $\frac{Q_d E_x}{m_d g} = \pm 0.1$ diverging from one another when approaching the lower electrode, as shown in Fig. 4.10(a) and for the region Z < 6.5 mm in Fig. 4.10(b). In a region where the sheaths are not overlapped, the contour lines denoting $\frac{Q_d E_x}{m_d g} = \pm 0.1$ converge with decreasing Z, and $\frac{Q_d E_x}{m_d g} = 0$ over a large range inside the box (the regions (-1mm < X < 1 mm or 5mm < Z in Fig. 4.10 (c) and Z > 6.5 mm in Fig. 4.10(b)).

In the experiments presented here, the overlapping is observed between the sheaths of the inner surfaces of the glass walls, instead of the top surfaces of the glass walls stated by Sheridan. In some cases, such as that shown in Fig. 4.10(b), there is no sheath overlap in the upper region of the box, while the sheath overlap in the lower part of the glass box.

The transition from non-overlapping to overlapping sheaths from the glass walls is most likely due to the decreased density of electrons and ions. Sheath theory indicates that the closer to the lower electrode surface, the smaller the electron and ion densities and this depletion may be greater within the box due to the absorption of electrons on the glass walls. Decreasing the electron and ion densities leads to a larger Debye shielding length, which in further means the sheath influence extends further, increasing the sheath width. Given that the glass box is immersed in the sheath of the lower electrode, an increasing shielding length for glass wall can be observed when approaching the lower electrode. As this sheath width increases to larger than the half of the width of the glass box, the sheaths of the glass walls begin to overlap.

Comparing the ‘flat’ regions for the vertical electrostatic force profiles (Fig. 4.9) and the overlapping regions in the 2D maps of the horizontal electrostatic force (Fig. 4.10), the ‘flat’ region and the overlapping sheath region coincide with one another. For example, in the case with the greatest sheath overlap (60 mTorr gas pressure and 1.4 W rf power), the ‘flat’ region shown in Fig. 4.9 (a) extends from approximately zero to 8.3 mm in Z, while the sheath overlap can be observed in almost the same region in Fig. 4.10 (a). For the case with the same pressure but at an increased rf power of 4 W, the ‘flat’ region in Fig. 4.9 (a) extends from $Z = 0$ to $Z = 6$ mm with the overlapping sheath region in Fig. 4.10(b) at approximately $Z = 0$ to $Z = 6.5$ mm. At higher gas pressures, no overlap is evident in the map of the horizontal electrostatic force shown in Fig. 4.10(c) and the corresponding vertical electric field force profiles in Fig. 4.9(b) exhibit no ‘flat’ region.. Therefore, the ‘flat’ region in the vertical force profiles can only be observed in a region where sheath overlap exists.

Overlapping of the sheaths produced by the box side walls ‘pushes up’ the sheath of the lower electrode, as shown in Fig. 4.9. Specifically in cases where sheath overlapping exists, the positions of the typical sheath profiles were observed to be higher than those formed for the bare electrode cases under the same operating parameters, albeit with a smaller gradient. This is most likely not due to the electrical force produced by the box side walls, since the vertical electrical force provided by the side walls is at least one order of magnitude smaller than the difference shown in Fig. 4.9. One possible reason for this may be that the ions in the center of the box reach the Bohm speed in the vertical direction much more rapidly under the influence of the side wall sheaths as compared to 'no overlap' cases. Therefore, the sheath of the lower electrode is formed higher or 'pushed up' as compared to the no sheath overlapping case.

The resulting 'flat' region observed is consistent with the rapid decrease in electron density. As previously shown, the electron density begins to drop at the sheath edge and continues to decrease rapidly in the sheath. Since in this case, the sheath edge is 'pushed up' due to existing sheath overlap, the electron density as well as the dust particle charge decrease rapidly as compared to the no overlapping case at the same height. Therefore, in this 'flat' region, the decreased change in dust particle charge when compared to the increase in the electrical field, causes the electrical force profile to appear 'flat'.

4.6 Conclusion

In this Chapter, we introduced a novel technique, the freefall particle technique, which allows the sheath profile measurement with small perturbation, high spatial resolution and minimal equipment requirements. This technique was used to measure the sheath profile both for a planar electrode and inside a glass box sitting on the electrode. This method was shown to accurately measure the electrostatic force in the sheath as well as the sheath width for various power and pressure settings. The resulting force profiles clearly identify conditions which produce overlapping sheaths from the inner surfaces of the glass box, as would be expected inside a trench. This overlap leads to a linear electric field force distribution in the horizontal direction and a 'flat' curve in the vertical electric field force profile.

CHAPTER FIVE

Ion Wake Field in Plasma Crystal and
the Relationship between Confinement and Dust Particle Structures

Parts of this chapter have been published as 'Ion wake field inside a glass box', Mudi Chen, Michael Dropmann, Lorin S. Matthews and Truell W. Hyde, Physical Review E, 94(3), 033201.

5.1 Introduction

Plasmas are generally thought to be the most disordered form of matter—which in its most highly ordered state is considered to be crystalline. Following a suggestion by Ikezi in 1986, liquid and crystalline plasma states were discovered in 1994 [Chu 1994]. The 'plasmas' in question are now 'complex plasmas', which consist of electrons, ions and charged microparticles. These multi-component systems are overall charge neutral and satisfy the usual requirements defining a plasma. In fact, the interesting regime of strong coupling, which gave rise to the new liquid and crystalline plasma states discovered in 1994, produces collisional plasmas, in the sense that the components readily exchange momentum and energy through Coulomb collisions. The term 'complex plasmas' was chosen not because the systems are complicated—all plasmas would qualify on this account—but because in fluid physics liquids containing micro- and/or nanoparticles are named 'complex liquids'. The analogy is obvious.

In this Chapter, a study of the underlying physics required to form dust particle structures will be presented. An overview of the complex plasma crystal and the basic interactions which can occur in dust particle structures will be introduced in Section 5.2. In Section 5.3, an experimental study of the ion wake field force will be described, while in Section 5.4, the relationship between system confinement and dust particle structures will be discussed.

5.2 Overview of Plasma Crystal and Basic Interactions within Dust Particle Structures

5.2.1 Plasma Crystal

Two of the most remarkable early discoveries in complex plasma were the existence of crystalline plasma states—i.e. a 'plasma condensation' state—and, liquid plasma states [Thomas 1994]. Early experiments showed the characteristic hexagonal patterns of quasi two-dimensional systems (see Fig. 5.1 taken from [Thomas 1994]) due to energy minimization. Later experiments, once experimenters were able to produce and investigate larger systems with several vertical layers showed that 'hexagonal close packed' (hcp) and 'face centered cubic' (fcc) lattice structures were often formed in addition to the early first observations of vertically aligned structures—see Figs. 5.2 and 5.3 (taken from [Pipper 1996, Zuzic 2000]). Theoretically, MD calculations had predicted a phase transition from the liquid to crystalline plasma states as shown in Fig. 5.3 [Hamaguchi 1997]. Both 'body centered cubic' (bcc) and fcc crystal structures were expected to exist for systems in thermodynamic equilibrium. However, both hcp structures (which has a Madelung energy significantly higher than the other two crystal structures mentioned) and the vertically aligned structures, (which were presumed to be due to ion focusing in the plasma sheath and a consequence of having only a few lattice planes located in the plasma sheath where ion flows are important [Schweigert 1996]), were unexpected. The ordering parameters for these phase transition are often described by coupling parameter Γ and Debye shielding parameter κ,

$$\mathit{\Gamma} = \frac{\text{Coulomb interaction energy}}{\text{Thermal energy}} \tag{5.1}$$

$$\kappa = \frac{\text{Particle separation distance}}{\text{Shielding length scale}} \tag{5.2}$$

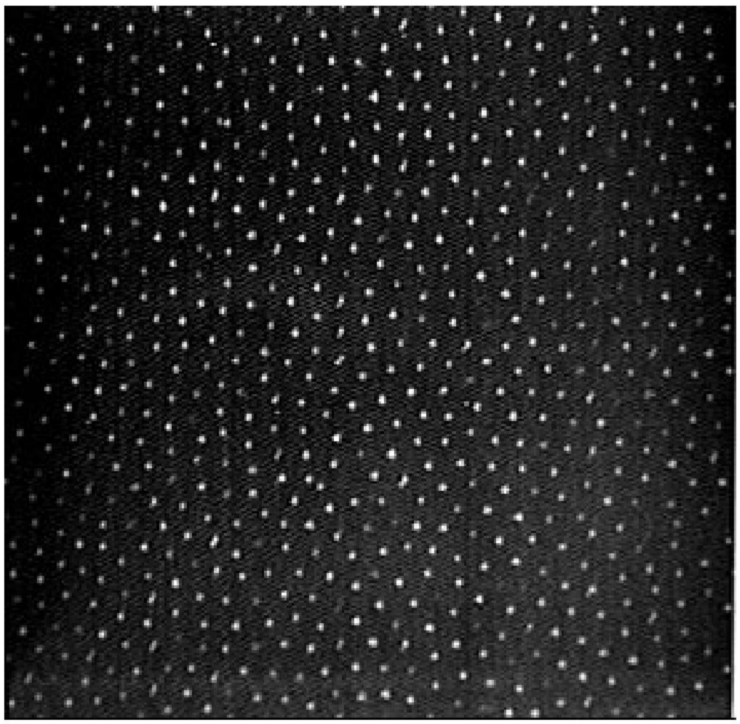

Figure 5.1. Image of a microparticle cloud in the plane above the lower powered electrode. The area shown is $7.7 \times 7.7\ \text{mm}^2$ and contains 724 particles of 7μm diameter. (Thomas 1994)

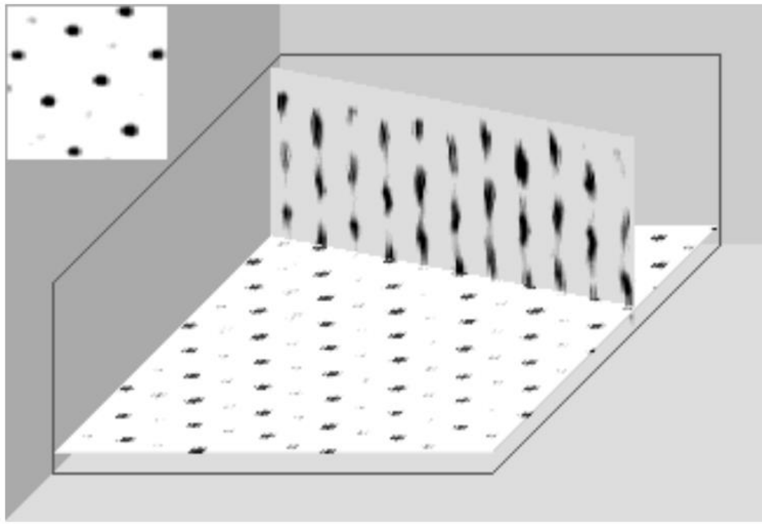

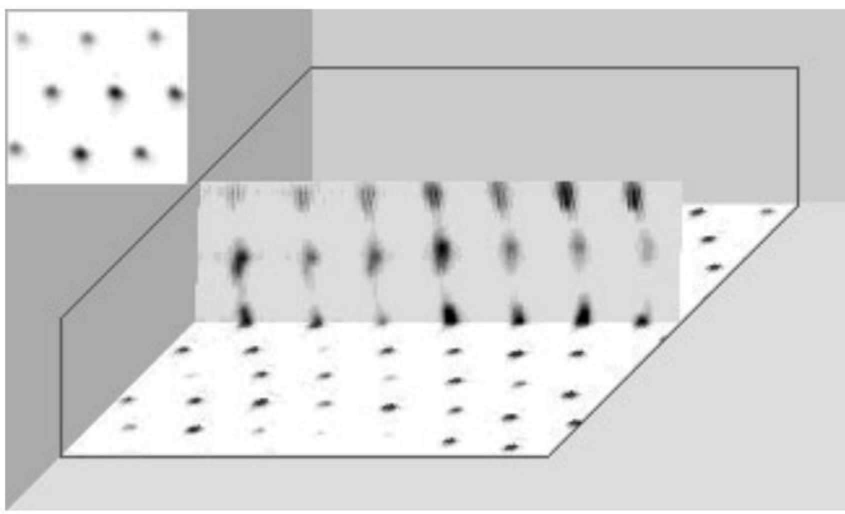

Figure 5.2. Images within the three-dimensional volume of a Coulomb crystal formed by 9.4 μm polymer spheres in a 1.4 Torr Kr discharge. In each image one horizontal plane and a vertical cross section through the data are shown; the inset shows a portion of the horizontal plane viewed from above. The data are contained in a stack of horizontal planar images resolved by selective illumination by a 90μm thick sheet of light from a focused, swept laser beam. The particle images appear longer in the vertical direction due to the infifinite thickness of the laser sheet. (*a*) bcc, (*b*) simple-hexagonal structure. (Pipper 1996)

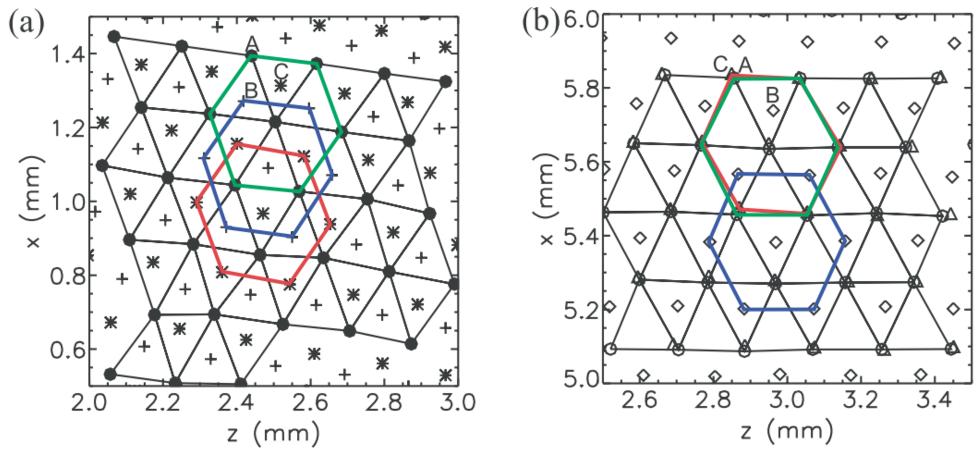

Figure 5.3. Superposed local regions of adjacent crystal layers: (a) three planes from the bottom part of the crystal. The symbols denote the particle positions in the third (open hexagon), fourth (△), and the fifth (⋄) layer. The planes are arranged in hcp lattice type. The three layers in (b) belong to another region, with the symbols showing the first (O), second $(*)$, and the third $(+)$ layer. The structure corresponds either to a fcc, or bcc lattice with the (111) plane parallel to the electrodes(Zuzic 2000).

In the limit $\kappa \to 0$, the phase transition occurs at the classical one component plasma (OCP) limit of $\Gamma \simeq 172$, as can be seen in Fig. 5.4.

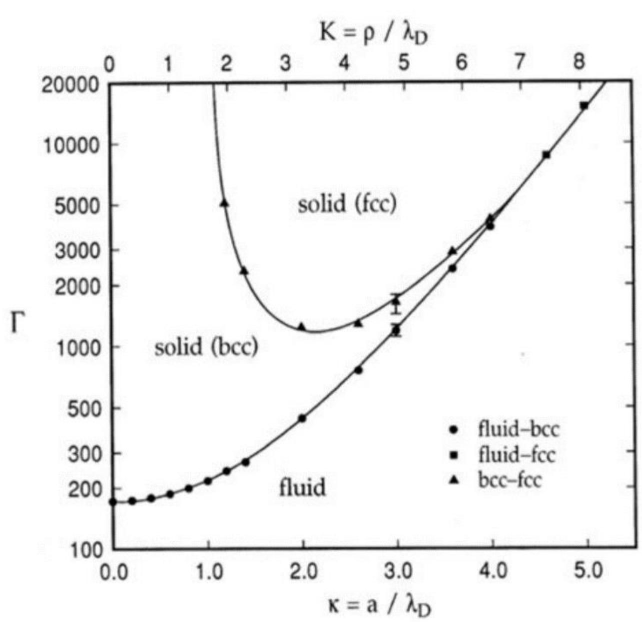

Figure 5.4. Numerical simulation of the Γ/κ phase space showing the fluid and crystalline states of a three-dimensional Yukawa system (Hamaguchi 1997).

In experiments on Earth, gravity provides a major large-scale perturbing body force. This is due to the fact that the complex plasma has to be suspended by an opposing force-and unlike liquid suspensions, where a homogeneous buoyancy force can be established to ‘neutralize’ gravity, this is not easy to achieve in plasma. The electrostatic fields used for particle suspension in plasmas usually have a characteristic length scale comparable to the sheath size and hence the supporting force has a gradient which can distort and modify suspended complex plasma structures. This is one reason why experiments in space, under microgravity conditions, are important. Recently, such experiments were carried out with the PKE-Nefedov and the PK-4 complex plasma experiment on board the International Space Station. The elusive *bcc* phase was observed and new insights into the co-existence of *bcc*, *fcc* and *hcp* crystalline phases were obtained [Nefedov 2003].

5.2.2 The Crystal-liquid Phase Transition

In 1996, the first kinetic study of a melting transition was published [Thomas 1996]. This was later elaborated on by Morfill [Morfill 1999] using further analysis of the kinetic properties of the complex plasma system. Summarizing these findings, the following picture emerges.

(a) The (vibrational) temperature of the microparticles in the crystalline state is approximately room temperature, suggesting a thermal equilibrium with the neutral gas. The velocity distribution of the dust particles is Maxwellian to a high degree of accuracy, making it possible to derive a coefficient of self-diffusion from kinetic measurements,

$$D(t) = \frac{\langle |r(t)-r(0)|^2 \rangle}{6t} \equiv \frac{1}{6nt}\sum_{i=1}^{n} \left[r_i(t) - r_i(0)\right]^2 . \tag{5.3}$$

This characterizes the system, since we can now compare the measured value of $D(t)$ with the result expected for Brownian motion, D_{B}, due to gas-particle collisions. It turns out that D is independent of t over the relevant timescales investigated $(0.5\ \mathrm{s})$, as expected for Markov-processes. Thus, values of $D < D_{\mathrm{B}}$ indicate 'caged' particles, that are limited in their mobility by the combined force fields of their neighbours. In the crystalline state $D \simeq \frac{1}{3} D_{\mathrm{B}}$.

(b) A 'flow and floe' stage follows as melting proceeds from this crystalline state. This is characterized by small islands (floes) of crystalline regimes (generally only 10 or so lattice planes in dimension) surrounded by liquid (flowing) regimes. Flows during this stage tend to be (kinetically) triggered by single particles leaving or entering a given lattice plane, thus forcing a readjustment of the system which occurs with observed asymmetry. When a particle leaves a horizontal lattice plane, the readjustment can involve up to 10 particles flowing along a lattice line towards the resulting vacancy in order to re-establish equilibrium again. This movement is often associated with a slight counterstreaming of the particles between the two boundaries. On the (microscopic) scales investigated, these flows can be regarded as substantial. On the other hand when a particle enters a horizontal lattice plane, it pushes its neighbors slightly outward. This readjustment to a new force equilibrium effects roughly as many particles as in the previous case, although its spatial extent is only noticeable over two lattice sites with the typical number of particles involved $\simeq 18$. It is believed this asymmetry may be a consequence of the anisotropy introduced by gravity, however, investigations under microgravity to test this assumption are still outstanding.

(c) The 'flow and floe' phase is very much reminiscent of a normal second order phase transition (like ice and water), albeit, on a comparatively microscopic scale. As such, the straightforward expectation was that this trend would continue with the 'floes' decreasing before disappearing and leaving a liquid complex plasma state. The temperature distribution of the system in the 'flow and floe' state seemed to support this, since it was clearly bi-Maxwellian, suggesting cold 'floes' and warmer 'flows' (see Fig. 5.5). However, the complex plasma behaved differently. On further 'heating' (or more appropriately on further reduction of Γ) the system actually began to re-crystallize, as determined from the orientational order parameter. At this point the vibrational amplitudes started to grow, as reflected in the kinetic temperature shown in Fig. 5.5. Although vibrations were initially localized, they rapidly spread throughout the system. Three-dimensional measurements were made to determine whether these vibrations were predominantly polarized in the horizontal plane, but for the system under study--which had a dozen vertical planes--no polarization was discerned to a statistical accuracy of a few percent. Although this presumably rules out systemic parametric instabilities as the cause for the existence of this vibrational phase, it could still be a consequence of a gravity induced asymmetry. However, to date, no measurements have been conducted under microgravity conditions to clarify this issue. Interestingly, such a 'vibrational phase' is predicted in the Lindemann melting criterion, so there is some substance to the possibility that kinetically this is exactly what could be expected to occur.

(d) After the vibrational phase the complex plasma system proceeded smoothly towards a disordered state. The frequency with which particles could leave their 'cage' (or lattice site) increased with vibration amplitude and very soon both the notion of a mean lattice site and translational or orientational order became meaningless. At this stage the coefficient of self-diffusion quickly became 10 and then 100 times larger than then the Brownian motion value and the system was in a disordered state and the phase transition was complete. Interestingly, on the basis of translational order, there was still a discernible peak. As such, it is not clear whether the system sublimed directly into a gaseous state. Unfortunately, this difference is hard to identify since the particles are, of course, trapped in a (gravitational) potential well and their scale height depends on their kinetic temperature. This means that the particles are always close together and some translational ordering is almost mandatory under those circumstances. Fig. 5.6 shows some images of the phase transition from a plasma crystal to the disordered state, including both the 'flow and floe' and 'vibrational' phases

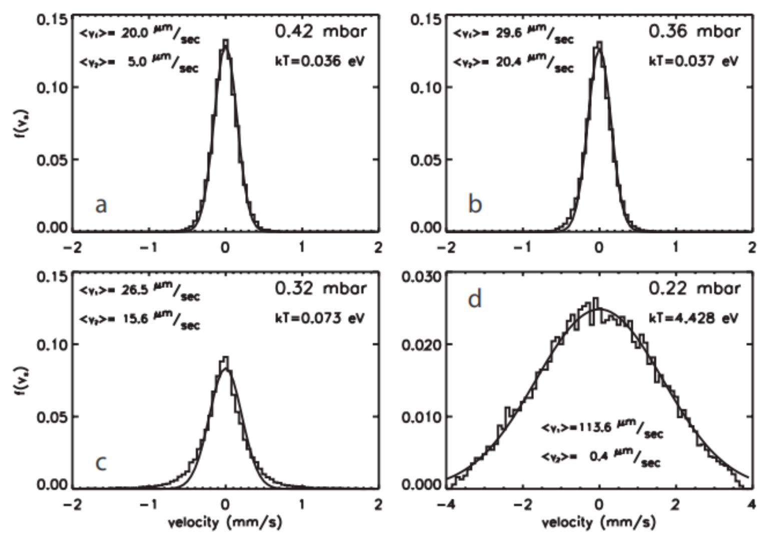

Figure 5.5. Velocity distributions of the microparticles during (a) the crystalline state ($T = 415$ K), (b) the 'flow and floe' state ($T = 430$ K), (c) the 'vibrational phase' ($T = 850$ K), and (d) the 'disordered' phase ($T = 50000$ K) (Morfill 2002).

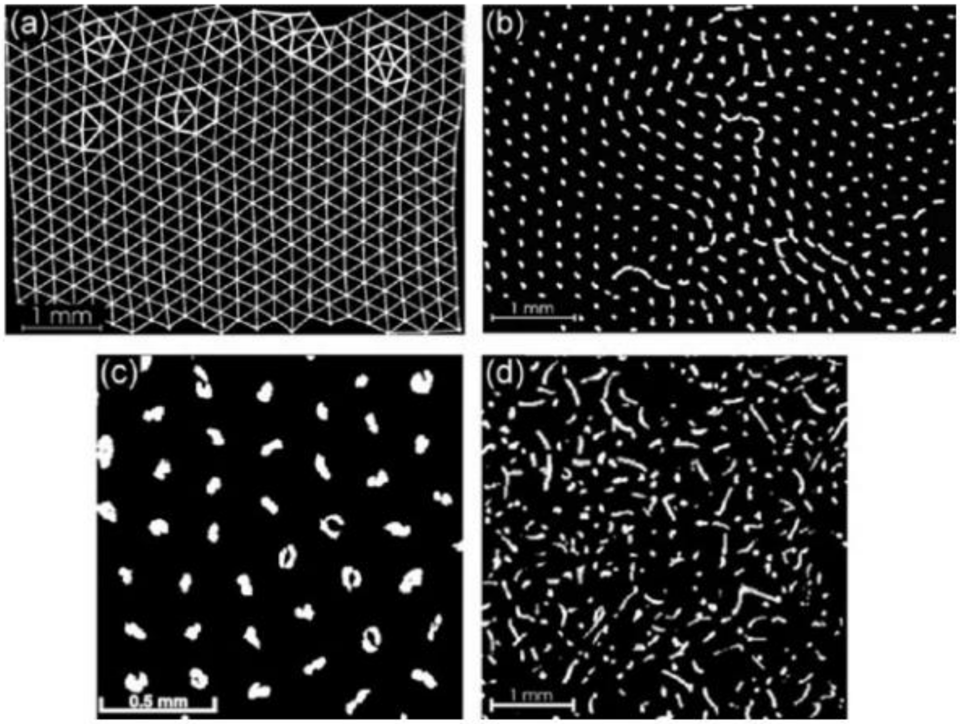

Figure 5.6. Different states of the plasma crystal: (a) crystalline, (b) flow and floe, (c) vibrational, and (d) gaseous (Morfill 2002).

5.2.3 Vertical Dust Particle Structures and the Forces Acting on the Dust Particles

All of the structures mentioned in 5.2.1 are observed to occur in a horizontal plane. They provide excellent data for studying crystal formation and structure, but they are not ideal for the investigation of phase transitions are the forces acting on the dust particles, due to the difficulties of controlling the dust particles inside such a dust particle structure.

Fortunately, through placement of a glass box on the lower electrode, as mentioned in Chapter Four, vertical dust structures can be easily obtained. Once stable, changing the pressure and input power allows phase transitions from 1D to 2D zigzag is from zigzag to 3D to easily be observed, as shown in Fig. 5.7.

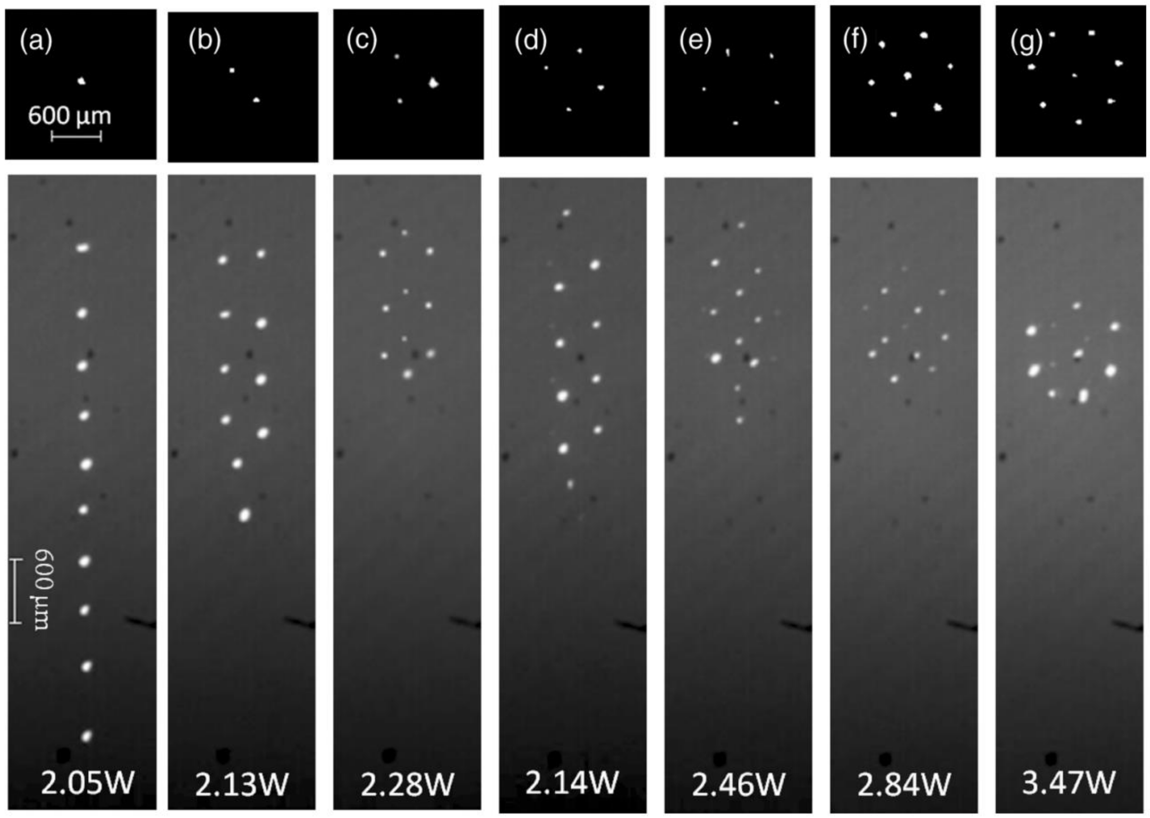

Figure 5.7. Top view (upper) and side view (lower) of vertical structures formed at varying rf powers. In all cases, the background pressure is held at 16 Pa. In (a)-(c), each structure contains a total of ten particles, while (d)-(g) include a total of 20 particles. One- through four-chain structures are shown in (a)-(d), with six- through eight-chain structures (including the center chain) shown in (e)-(g). Notes: Data collected via the top camera have been processed by applying a binary threshold to each image. Due to the width of the laser sheet used for illumination and the specific portion of the chain imaged by the camera, not every particle in each structure is visible in the side view images (Hyde 2013).

After forming a 1D dust particle structure (Fig. 5.7(a)), particle numbers can be chosen by lowering the system power in order to drop the lowest dust particle. At this point, by changing the system gas pressure and power, various dust particle structures and instabilities can be established. Therefore, the glass box system is convenient for investigating the phase transitions and forces acting on each individual dust particle.

The forces acting on any individual dust particles mainly includes the gravitational force, the sheath electrical field force (balancing the gravitational force), the confinement force, the thermal force, the neutral drag force and the ion wake field force. (Additional forces were discussed in Chapter Four.) In scetion 5.3, the ion wake field force acting on an individual dust particle inside the glass box will be examined.

5.3 Ion Wake Field Inside a Glass Box

The ion-wake effect has been studied both theoretically [Milock 2008] and experimentally [Carstensen 2012], since research showed that charged dust particles tend to align with the ion flow [Milock 2010]. Upstream particles focus the ions at a point beneath them, where downstream particles are attracted by the positive space charge region created due to this ion focusing. The nonreciprocal interaction [Melzer 1999] between the upstream and downstream particles is a signature property of this ion-wake effect. In this case, upstream particles dominate the motion of downstream particles, while the reverse effect is so small that it can often be considered negligible. Recent simulation studies [Milock 2012] also indicate that the downstream particles can become discharged by this interaction between the upstream and downstream particles.

As noted, a glass box confinement has proven ideal for the formation of vertically aligned 1D, 2D and 3D structures, which are difficult to obtain under other types of confinement. However, a comprehensive study of the role that the ion-wake effect plays within such a confinement or whether the ion-wake field exists at all in this environment has not yet been conducted. Given the strong confinement produced by the glass box and the direct interaction between the particles, an investigation of the ion-wake effect under these conditions is solely needed to determine a proper explanation of the underlying physics.

5.3.1 The Confinement Created by the Glass Box

The experimental setup discussed here is similar to the setup shown in Chapter Four, with the introduction of a perturbing laser. Using the technique described in Chapter Four, the confinement of the glass box under specified operating conditions was measured with the results hown in Fig. 5.8.

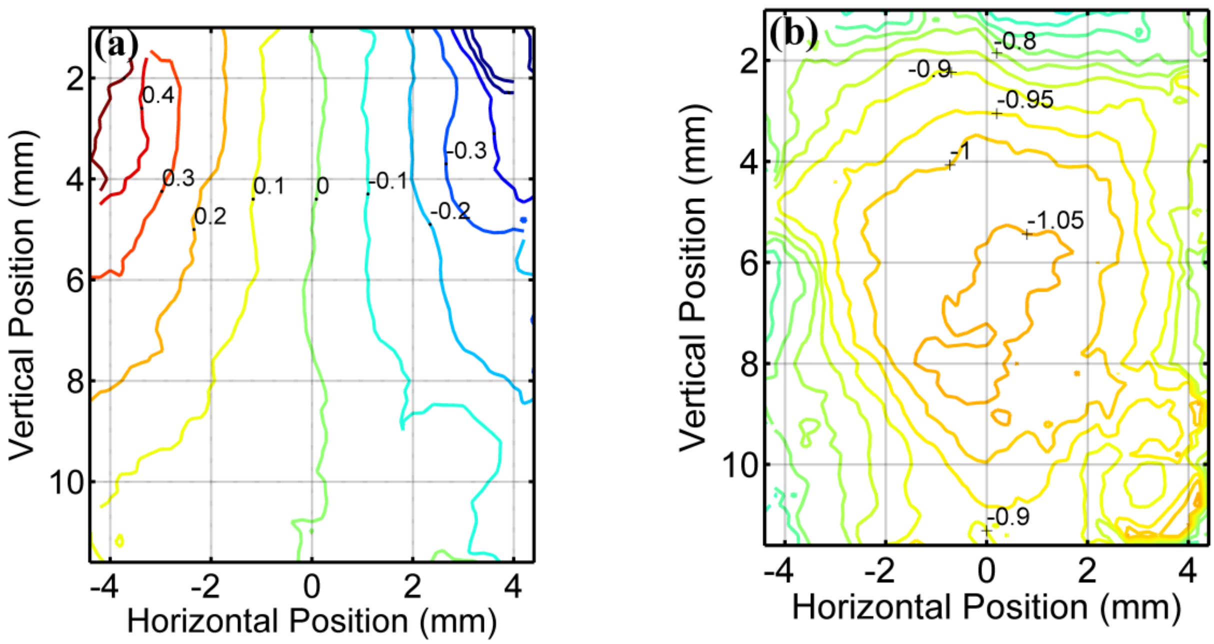

Figure 5.8. Maps of the horizontal (a) and vertical (b) dust particle accelerations measured within the box. Experiments shown were run at 6.67 Pa Argon gas pressure and 2 W RF power. Particle acceleration is given as a multiple of *g (and a negative sign indicates upward acceleration)*. In the vertical direction the distance is measured from the top of the glass box while in the horizontal direction distance is measured from the center of the box.

Fig. 5.8(a) shows the horizontal acceleration of the dust particles. This acceleration is always directed toward the center of the box, with the largest acceleration (approximately 0.5 g) observed at the top edge. As shown, in the central region of the box (-1 mm $\leq x \leq$ 1 mm, -2 mm $\leq z \leq$ -6.5 mm) the horizontal confinement force can be treated as a linear force with a restoring constant of approximately -0.11±0.01 $m_d\, g$ mm^{-1}.

Fig. 5.8(b) shows the vertical acceleration map for the dust particles. Particles can only levitate in the region where their vertical acceleration is greater than or equal to the acceleration due to gravity. In contrast to the conditions within the plasma sheath formed without a box, under the experimental parameters shown, the vertical confinement force inside the glass box does not increase monotonically as a particle approaches the lower powered electrode. Instead, a maximum vertical acceleration in magnitude of ~1.05g is found at the middle of the box (-2 mm $\leq x \leq$ 2 mm), with an extended vertical region (5.5 mm $\leq z \leq$ 9 mm) where the acceleration is approximately -1g. As such, a 1D dust string consisting of more than two particles can only be formed in this region. For the operating parameters used to generate the data shown in Fig.2, the longest particle chain observed consisted of 11 particles spanning a vertical region of 9.7 mm. It should be noted that unlike the case without a box, where the radii of the particles within such a vertical structure are often different, a particle chain formed inside the box consists of nearly identically sized particles. As such, the vertical levitation region is highly dependent on the system’s operating parameters. For example, decreasing the RF power decreases both the extent of the levitation region as well as the magnitude of the confining force until at some critical points, particles can no longer be levitated and those closest to the lower electrode are removed. Thus, the number of particles comprising a vertically aligned particle chain can be controlled using the RF power.

5.3.2 *Investigation of Ion Wake Field Force*

In order to examine particle-particle interactions within the chain, a Coherent VERDI G5 laser was employed to perturb individual particles and their subsequent motion was recorded using a high-speed camera running at 500 fps. In the simplest case, a particle pair was formed and an individual particle was pushed horizontally using a pulsed laser beam of 100 ms duration and 10 mW power. The diameter of the beam spot was approximately 50 μm and the particles were initially aligned vertically with an interparticle separation distance of 0.80 ± 0.05 mm. Due to the short heating time, low laser power, and small diameter of the beam as compared to the interparticle distance, each particle could easily be perturbed separately. Fig. 5.9 shows the experimental data as well as a cartoon of the particle motion while separately perturbing the top or bottom particle.

As shown in Figs.5.9 (b)-(e), pushing the top particle to the left causes the bottom particle to move upwards and slightly to the left. As the horizontal displacement of the top particle increases, the confinement produced by the box eventually forces it back toward equilibrium, resulting in the bottom particle returning to its original position. Perturbation of the bottom particle in an analogous manner is illustrated in Figs.5.9 (g)-(j). Once the bottom particle is removed from its equilibrium position, it immediately moves upwards as shown in Fig. 5.9(h). During this time, the top particle remains stationary until the interparticle distance is smaller than 550 μm, at which point it is repelled slightly upwards and to the right. Once the bottom particle returns to its equilibrium position (again due to the horizontal confinement), it drops quickly beneath the top particle, as

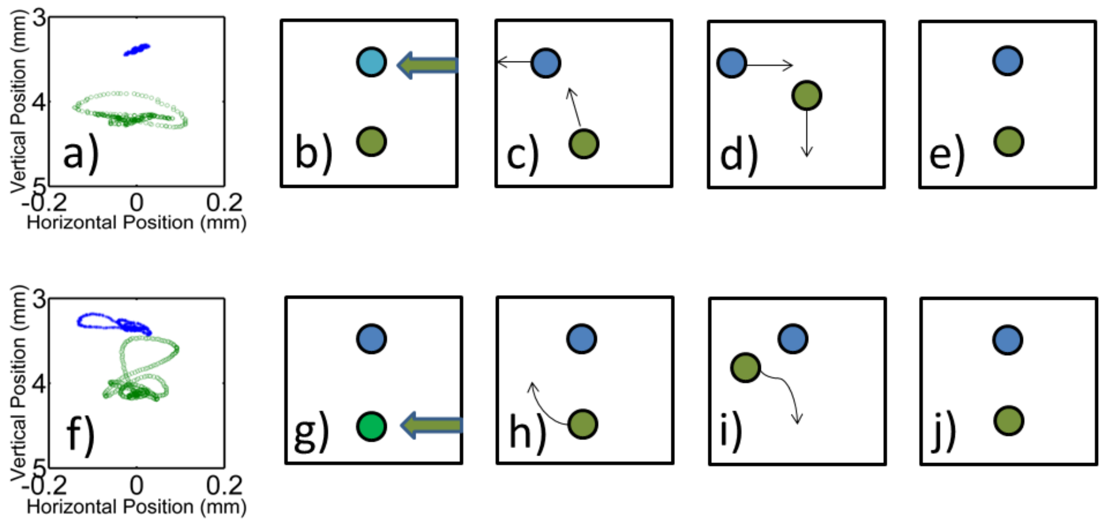

Figure 5.9. Perturbed motion of particles within a particle pair. Blue represents the top particle of the pair while green represents the bottom particle. The experimental data (a) and representative cartoon (b-e) when only the top particle is disturbed; the experimental data (f) and representative cartoon (g-j) when only the bottom particle is disturbed. The vertical axis and horizontal axis in (a) and (f) represent the distance to the top and the middle of the box, respectively.

Seen in Fig. 5.9(i). Finally, in Fig. 3(j), the particle pair resumes its stable configuration after a short time of exhibiting damped oscillations.

As shown in Eq. 5.3, the total force acting on the particles once the laser beam is removed consists of the confinement force, the neutral drag force and the particle-particle interaction force

$$\mathbf{F}_{total} = \mathbf{F}_{conf} + \mathbf{F}_{drag} + \mathbf{F}_{inter}, \qquad (5.3)$$

since for the reasons described earlier, the ion drag force and the thermophoretic force can be considered negligible. Therefore, using the previously measured confinement force and total force while assuming a neutral drag force given by

$$\mathbf{F}_{drag} = -\boldsymbol{\beta}v, \qquad (5.4)$$

the particle-particle interaction force can be calculated from the measured total force using Eq. 5.3.

Fig. 5.10 shows the displacement (Figs. 5.10(a)(c)) and the calculated acceleration (Figs. 5.10(b)(d)) of both particles due to the particle-particle interaction force in the horizontal direction. Negative quantities represent movement directed toward the left, while positive numbers represent motion to the right. Note that the negative acceleration of the illuminated particle persists for some time after the laser is turned off. This is assumed to be due to the photophoretic force caused by particle heating [Wurm 2010]. As shown, when the top particle is perturbed from its equilibrium position (Fig. 5.10(a)), the bottom particle follows in the same direction over a short range (100μm) before reversing direction to oscillate about its equilibrium position.

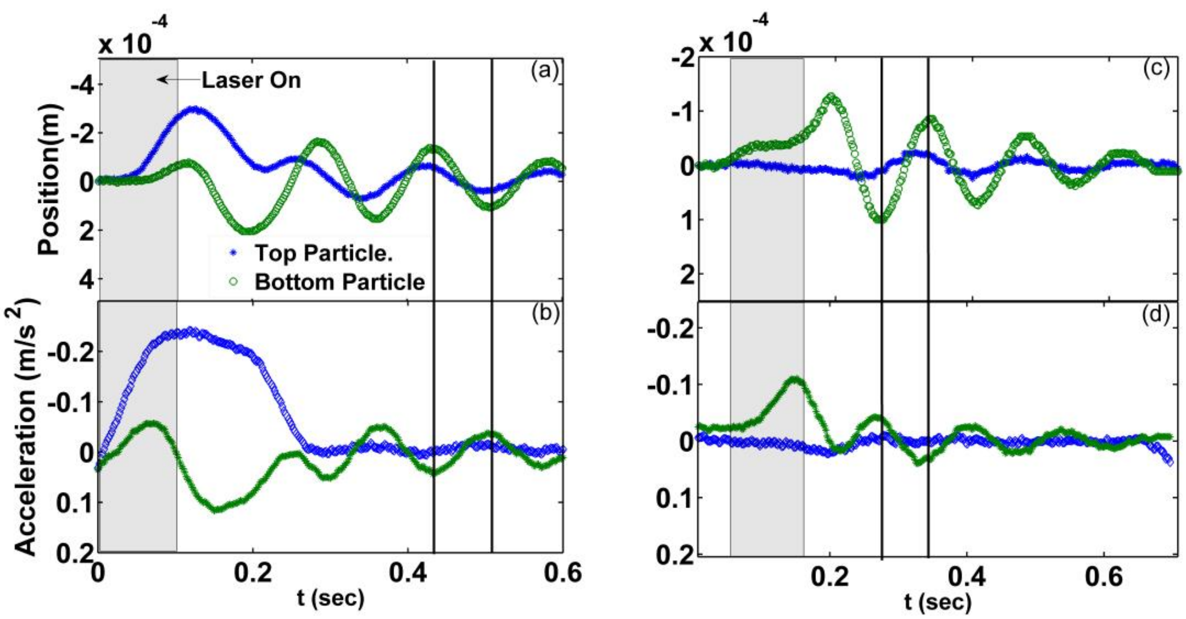

Figure 5.10. Particle motion and acceleration due to the particle-particle interaction force in the horizontal direction. (a) Motion and (b) acceleration for perturbation of top particle and (c) Motion and (d) acceleration for perturbation of the bottom particle for the conditions described in the text. The shaded region indicates the time during which the laser illuminated the particle. Vertical lines indicate the positions and accelerations of particles at corresponding times.

When the bottom particle is pushed to the left, as shown in Fig. 5.10(c), the top particle remains at its original position before being repelled slightly to the right. This phenomenon confirms the assumption that the initial motion observed for the bottom particle when the top particle is pushed (see the trajectory during the first 0.1 s in Fig. 5.10(a)) was not caused by the laser. This damped particle oscillation also allows the neutral gas drag coefficient β to be calculated using [Zhang 2010],

$$\ddot{X} + \beta\dot{X} + \omega_0{}^2 X = 0 \qquad (6)$$

where X is the horizontal displacement from equilibrium position and ω_0 is the natural frequency of the horizontal potential well. The value of β determined in this manner is $(8.97\pm1.15)\times10^{-12}$ N m^{-1} s, also in agreement with analytically calculated results.

Figs. 5.10(b) and (d) show the accelerations created by the force imparted by the laser and resulting interparticle interactions. In the first case, the top particle was initially given an acceleration of 0.3 m/s^2 to the left by the laser. The bottom particle followed the top particle, was displaced to the left and experienced a maximum acceleration of 0.05 m/s^2. As the particles returned to oscillate about their equilibrium positions after 0.3 s, it can be seen that the acceleration of the top particle was almost zero, while the bottom particle still had a maximum acceleration of 0.04 m/s^2 directed toward the top particle, as indicated by the vertical lines showing the correlation between the positive force for a negative displacement. Upon perturbation of the lower particle, Fig. 4(d), the top particle was repelled, moving to the right for the first 0.2 s during the time that the bottom particle approached it from below and left. By the time the bottom particle returned to its equilibrium position, the interaction force acting on the top particle was almost negligible, although the bottom particle continued to exhibit an attractive interaction, as indicated by the vertical lines.

Using the perturbation method described, acceleration maps for the interparticle interaction between the top and bottom particles were generated by separately perturbing particles with varying laser powers between 0.01W and 0.50W. The region where the data was collected was overlaid with a grid having a spacing of 0.1mm and the average acceleration was calculated for all data points within a radius of 0.05mm of each grid point. Accelerations were calculated only for regions containing at least five data points. In all cases, the coordinate origin was centered on the position of the top particle, indicated by a blue dot, while the y-axis and the x-axis represent the vertical and horizontal interparticle separations respectively. At equilibrium, the bottom particle is located at [0, 0.79] as indicated by the green dot, measured with respect to the location of the top particle.

In Figs.5.11 (a) and (c), positive values indicate a horizontal acceleration to the right, while in Figs. 5.11 (b) and (d), positive values represent a downward vertical acceleration. Figs. 5.11(a) and (b) provide interaction maps for the force of the top particle acting on the bottom particle, (generated by perturbing the top particle) while the data shown in Figs. 5.11(c) and (d) were obtained by perturbing the bottom particle and measuring the force exerted on the top particle by the bottom particle at the specific separations. Taken together, these provide the interparticle interactions between the bottom and top particles. Note that the horizontal axes are asymmetric in the two cases, as the bottom particle is to the right of the top particle when the top particle is perturbed, while the bottom particle is to the left of the top particle when the bottom particle is perturbed. White regions out of the contours indicate a lack of data.

In Fig. 5.11(a), the horizontal acceleration of the bottom particle is shown for the region where the interparticle distance was larger than 0.4 mm. Horizontal accelerations are always directed toward the midline directly beneath the top particle, indicating that the bottom particle experiences a horizontal attractive interparticle interaction across this region. The strongest attractive acceleration, -0.05 m/s^2, is observed approximately 0.3 mm away from the midline beneath the top particle, which is in agreement with measurements made by Hebner using two particles with different masses approaching each other under a cutout confinement [18, 30]. As seen in Fig. 5.11(b), the vertical acceleration of the bottom particle is always downward, showing there is only a repulsive interaction from the top to the bottom particle. The maximum downward acceleration, 0.31 m/s^2, is observed at approximately [0, 0.79], which coincides with the particle's equilibrium position. As shown in Fig. 5.11(c), the horizontal acceleration provided from the bottom to top particle is almost zero when the bottom particle is at its equilibrium position. All accelerations shown in the Fig. 5.11(c) are positive (to the right) while the bottom particle is at the left side of the top particle. This indicates that the bottom particle repels the top particle to the right. Note that the top particle can only be repelled by the bottom one, and that repulsive acceleration increases with decreasing interparticle distance. In Fig. 5.11(d), the bottom particle causes the top particle to have an upward (negative) acceleration when their vertical separation is larger than 0.2 mm. In this region, the repulsive interaction from bottom to top increases with decreasing distance with a maximum magnitude less than 0.1 m/s^2. It is also interesting to note that the top particle gains a downward acceleration when the bottom particle is close to it and in the same horizontal plane.

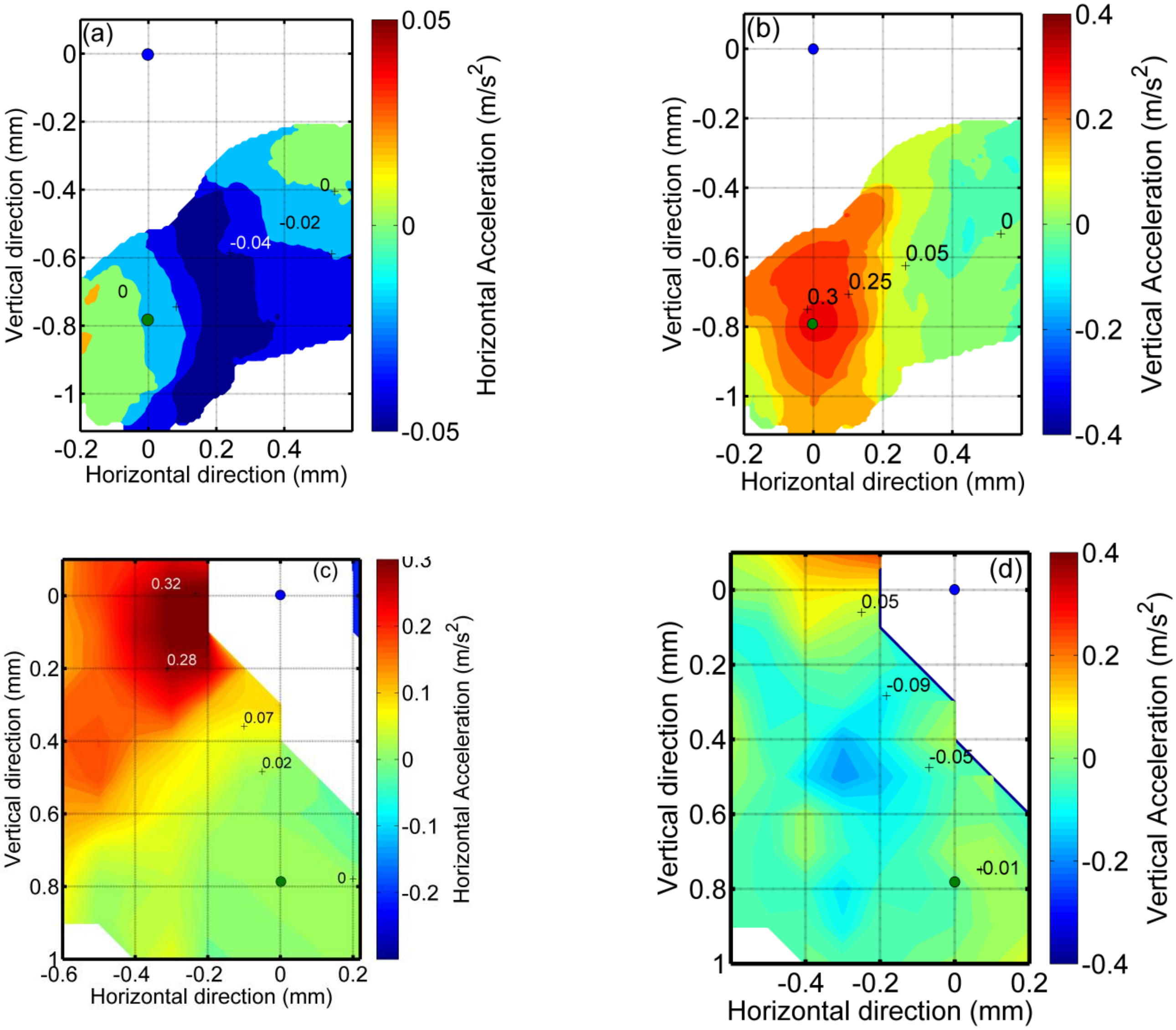

Figure 5.11. Maps of the acceleration due to interparticle interaction. Figures (a) and (b) show the horizontal and vertical acceleration of the bottom particle due to the interaction from the top particle when the top particle is perturbed. Figures (c) and (d) show the horizontal and vertical acceleration of the top particle due to the interaction from bottom particle when the bottom particle is perturbed. In all cases, [0,0] is the position of the top particle and the x- and y-axes give the horizontal and vertical displacement of the bottom particle from the top particle. Positive acceleration values indicate rightward and downward acceleration, respectively. The blue point indicates the position of the top particle at the point [0, 0], while the green circle indicates the equilibrium position of the bottom particle at the point [0, 0.079].

As shown in Figs. 5.10, 5.11(a) and (c), in the horizontal direction, the top particle of a vertically aligned two particle chain attracts the bottom particle, while the bottom particle exerts little to no force on the top particle at the same relative positions. Only a repulsive horizontal force can be observed on the top particle from the bottom particle in Fig. 5.11(c). At the same time, Figs. 5.11(b) and (d) show that while both the top and bottom particles in the chain repel each other in the vertical direction, the acceleration of the top particle is much smaller than the acceleration of the bottom particle. The top particle exerts a maximum downward vertical acceleration (and therefore force) of 0.31 m/s^2 on the bottom particle when it is at a point 0.79 mm directly below the top particle. This point coincides with the equilibrium position of the lower particle. The corresponding acceleration of the top particle in the equilibrium configuration is less than 0.01 m/s^2. In other words, the interaction between the top and bottom particle is non-reciprocal in both the horizontal and vertical directions.

This non-reciprocal attractive interaction in the horizontal direction has been previously observed in particle-pair experiments under similar operating conditions but without a glass box confinement [Carstensen 2012]. It is generally explained using the ion-wake effect, where a positive ion-focusing region is formed beneath the upper particle due to the ion flow, as shown in Fig. 5.12. The positive space charge region, the location of which is determined by the upstream particle, can attract the downstream particle, while the downstream particle can only repel the upstream particle since both are negatively charged. When the upstream particle move in horizontal direction and the attractive force from the ion-wake is larger than then repelling coulomb force between two particles, the downstream particle will follow the upstream particle since the ion wake follows the upstream particle. Due to the non-reciprocal nature of this attractive force, the non-reciprocal attractive interactions in the horizontal direction can be observed until the inter-particle distance is small enough to make the reciprocal repelling coulomb force larger than the attractive force.

The positive space charge region also causes the downstream particle to charge less negatively as there is an enhanced ion impact on the downstream particle. This discharging effect has been measured experimentally [Carstensen 2012] as well as predicted numerically [Ludwig 2012] but again without a glass box confinement. Given that a non-reciprocal interaction is considered to be a primary indicator of the ion-wake field effect, the experiments here prove the existence of an ion-wake field within the box, answering a long standing question in the field.

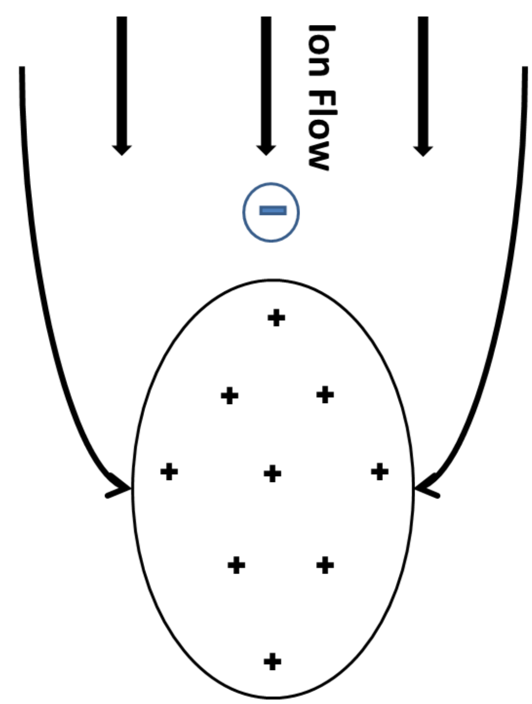

Figure 5.12. Scheme of the ion wake. The blue circle is the dust particle.

It is interesting to note that due to the strong confinement provided by the box, an attractive interaction can only be observed close to the midline beneath the top particle, which in these experiments spans a horizontal region of approximately -0.3 mm $\leq x \leq$ 0.3 mm. Outside this region, the horizontal confinement produced by the glass box is much larger than the observed attractive effect, which may explain why the existence of the ion-wake effect within a glass box has remained in question for such a long time. In the vertical direction, the wake field effect is much more apparent. As shown in Fig. 5.11(b) and (d), the bottom particle always experiences a downward interaction while providing only a small interaction acceleration on the top particle, particularly at vertical distances larger than 0.7 mm. This implies that the non-reciprocal interparticle ratio (i.e., the interaction between the upstream and downstream divided by the interaction between the downstream and upstream particle) may be quite large (approximately 5-60). This is interesting since for experiments without a glass box, this ratio is much smaller (approximately 5-10) [Carstensen 2012]. The largest value found for this ratio in our experiment was R = 60, observed when particles were near their equilibrium positions (top particle at [0, 0] and bottom particle at [0, 0.79]). The difference is due to the different inter-distance between dust particles. Outside the glass box, the vertical pair is obtained by dropping dust particles with different sizes. Due to the large gradient of electric field near the levitating positions of dust particles, the inter-particle distances are usually less than the shielding length. However, inside the glass box, due to the small gradient of electric field near the dust particle levitating positions, with the discharging effect of ion wake, the inter-particle distance when the particle pair are at their equilibrium positions is equal or larger than then shielding length. Therefore, comparing with the case without box, our cases have a much smaller Coulomb/reciprocal force between the up and downstream particle and a larger non-reciprocal ratio near the particles equilibrium positions. The downward acceleration gained by top particle when the bottom particle is close to the top particle maybe due to the resolution of our mapping technique.

5.3.3 Conclusion

A non-reciprocal particle interaction was observed in both the horizontal and vertical directions, confirming the existence of an ion-wake field within the glass box. It was shown that for this case, the predicted attractive horizontal non-reciprocal phenomenon can only be observed near the midline of the box due to the existence of the strong inherent confinement forces produced by the box while in the vertical direction, the non-reciprocal ratio is much greater than that observed without a glass box confinement. This explains why the existence of an ion-wake field in a glass box has long been in question; the horizontal attractive interaction between a particle and the ion-wake field is much smaller than that provided by the confinement force for most regions within the box. However, at the midline of the box, these become comparable and in the vertical direction, the effect of the ion-wake field can become large enough to play an integral role in determining the position of the downstream particle. A representative example of this is the extended levitation region observed where dust particles experience an upward electrical force approximately equal to that of the gravitational force. This ‘flat’ confinement region is the key factor for forming long 1D vertically aligned dust particle structures.

The discussions above shows the ion-wake field force rarely is comparable in magnitude to the confinement forces under most conditions. Therefore, in this case, due to the box, the key factor for forming vertical dust particle structures is the confinement force.

5.4 The Relationship between the Confinement and Dust Particle Structures within a Glass Box

The formation between various dust particle structures within a glass box have attracted a lot of interest. Although research has shown that these transitions are directly related to the confinement, due to a lack of data on this confinement, only a few particle-pair transitions, such as the Vertical-to-Horizontal transition (VHT) and the Horizontal-to-Vertical transition (HVT), have been studied. Both transitions are thought to be highly depending on the ratio of the confinement strength between the horizontal and vertical direction (γ).

Using the technique introduced in Chapter Four, the confinement within a glass box is discussed below and the relationship between structural transitions and γ is examed.

5.4.1 The Confinement inside a Glass Box

The following experiments employ an identical setup to that used in Chapter Four and Chapter Three. The gas pressure was initially set to 80 mTorr with the system power (rf) at 2W. Maps of the electric field force due to the confinement for experiments both without and within a glass box have been shown in Fig. 5.13, in which, (a) and (b) represent the horizontal and vertical confinement without the box while (c) and (d) represent the horizontal and vertical confinement within the box. The 0 in x-axis and y-axis indicate the midline of the box in the horizontal direction and the position of the lower electrode in the vertical direction, respectively. As shown in Figs. 5.13(a) and (c), there is very little horizontal confinement when there is no box, while once a box is placed on the lower electrode, a strong horizontal confinement as large as 0.6 *mg* (60% of the gravitational force effect on the dust particle) was observed. Using this data, it can be seen that the strongest horizontal confinement occurs near the top edge of the box while below 5 mm from the top of the box, it is reduced to less than 0.1 *mg*. This clearly shows that the horizontal confinement strongly depends on the height or the distance from the top edge of the box. Therefore, for vertically aligned dust particle structures, individual particles within each structure experience different horizontal confinement forces. Thus, it is not valid to use a confinement force measured at the position of the top particle in the chain to represent the confinement force on any other particle within the dust particle structure.

In the vertical direction, the confinement outside the glass box as shown in Fig. 5.13(b) increases as the lower electrode is approached, decreasing quickly when moving away from the lower electrode. This is the typical electrical field force map whenever a dust particle is moving in the sheath of the lower electrode. In this case, it is valid to consider this as a parabolic potential. However, within the glass box, a totally different vertical confinement can be observed in Fig. 5.13(d). In this case, the confinement force does not increase as the height decreases, but instead, it increases as the particle moves closer to the lower electrode, reaching a maximum of around 1 to 1.05 mg at 6-10 mm above the lower electrode before decreasing. This can not be treated as a parabolic potential as has been assumed in some studies. In this case, both the maximum amplitude and the gradient for the vertical confinement are much smaller than for the case without the box. The reason is due to the overlap of the sheath, which has been discussed in Chapter Four.

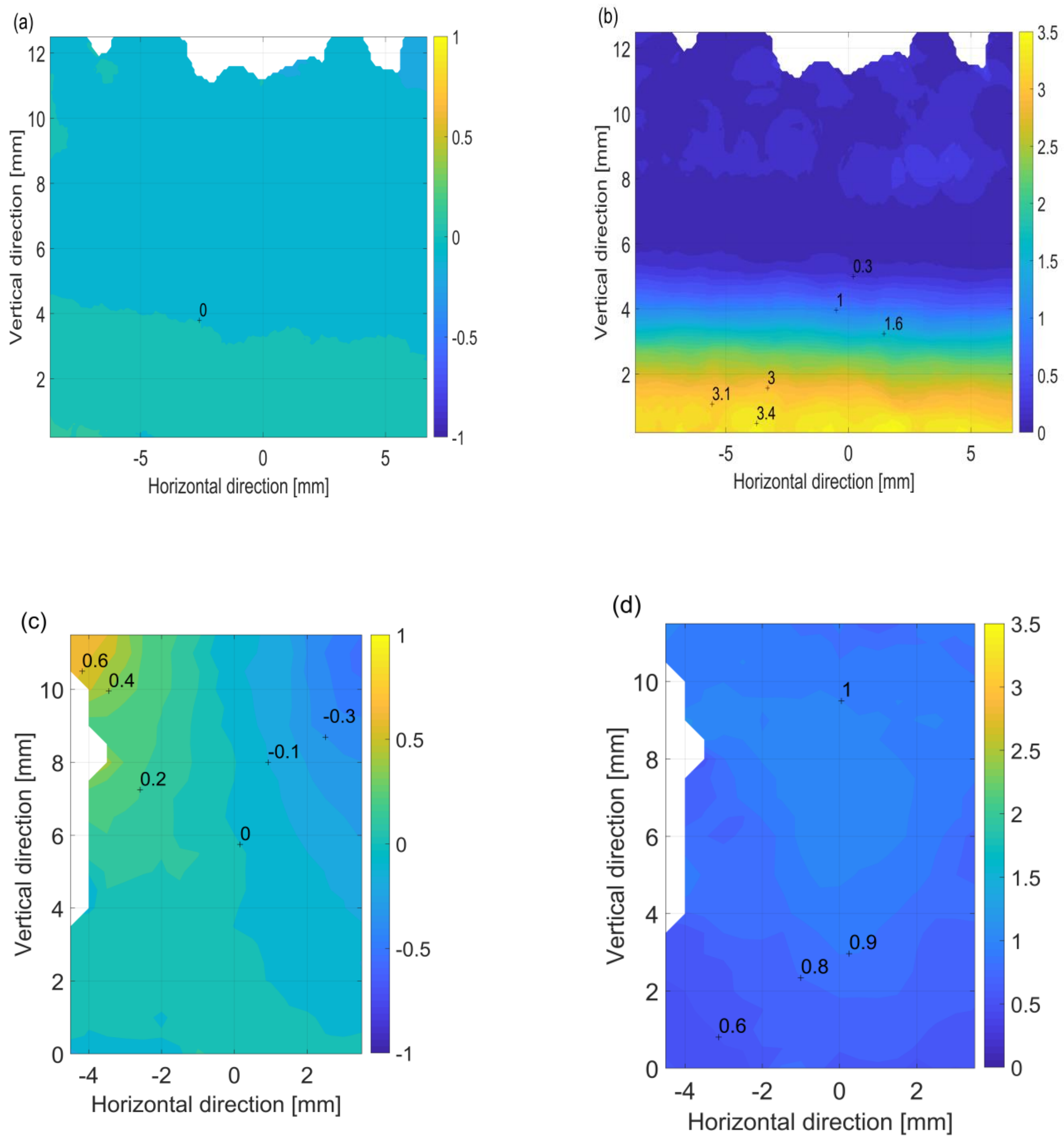

Figure 5.13. The confinement force map outside (a)(b) and inside (c)(d) the half inch glass box. (a)(c) represent the confinement force in the horizontal direction and (b)(d) represent the confinement force in the vertical direction.

5.4.2 The Relationship Between the Confinement and Dust Particle Structure

Inside the glass box, it has been shown that dust particles can form various structures by simply adjusting the operating parameters [Hyde, 2012]. As an example, increasing the rf power produces the structures shown in Figs. 5.14 (a) to (e). In these structures (a)(d)(e) are stable. However, as shown in (b) and (c), any small change in plasma parameters or any disturbance can lead to structural changes. Therefore, in this paper these structures were categorized into four different types: a single chain (Fig. 5.14(a)), helical structures (Figs. 3(b)-(c)), a double layer (Fig. 5.14(d)) and a single layer (Fig. 5.14(e)).

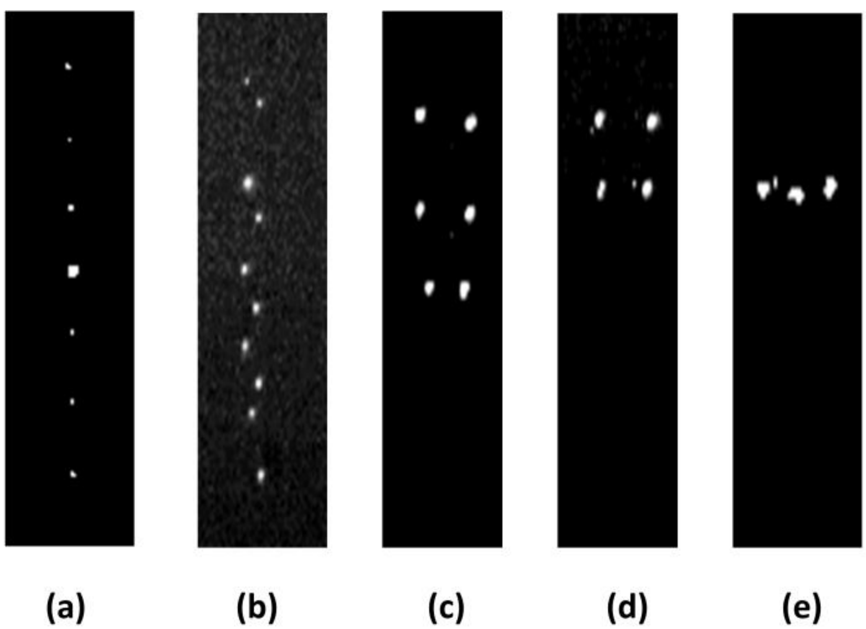

Figure 5.14. Side view of dust particle structures formed inside a glass box.

By conducting experiments under different pressures, these structures, especially the single chain, double layer and single layer can always be observed. The transitions between (a) to (b), (c) to (d) and (d) to (e) are named transitions 1, 2 and 3, respectively. The experimental parameters when these transitions occur are called the transition parameters. It should be noticed that although all these transitions are reversible, the reverse transition parameters between transitions 1 and 2 are different. Studies have shown that particle structural transitions are highly related to γ, defined as the ratio of the confinement strength, i.e., the gradient of the confinement force between the horizontal and vertical direction. However, the majority of these studies were conducted employing a cutout confinement and the value of γ was determined either at the position of the top particle or the center of the chain and then used to represent the γ value for the entire particle structure. As discussed above, this is not valid, especially inside a glass box. Moreover, in our experiments, it was found the transition parameter for transition 1 is very sensitive to dust particle number. As a result, under the same pressure, particle chains having fewer particles reach the transition point at higher rf powers than do chains with more particles. This has not been explained in other studies.

Employing a confinement force map, such as the one shown in Fig. 5.13, allows γ to be easily obtained by calculating the gradient of the confinement force in the horizontal and vertical directions. As an example, confinement strength ratio maps were produced at the operating parameters for transitions 1, 2 and 3 of 80 mTorr and the positions of the dust particles were recorded by the side view camera as shown in Fig. 5.14. In order to make the mapping result more easily be seen, max $\gamma = 1$ shows all of the regions where horizontal confinement is stronger than the vertical confinement.

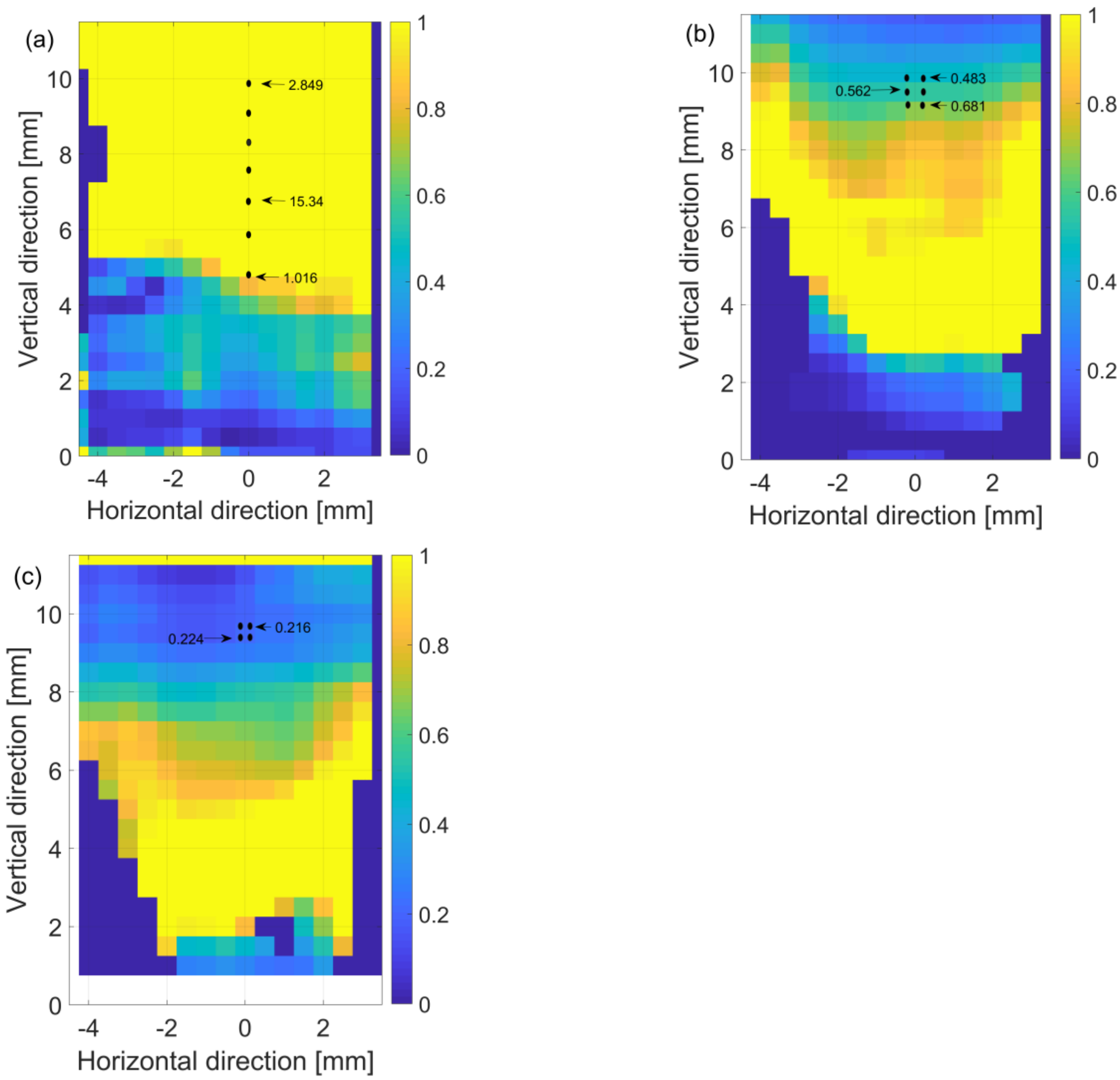

Figure 5.15. The map of the γ ratio of the confinement strength in the horizontal and vertical direction at transitions 1(a), 2(b) and 3(c) for 80mTorr. The black dots represent the positions of the particles recorded by the side view camera with the numbered arrows showing the value of γ at these positions.

Using experimentally measured maps such as the ones shown in Fig. 5.15, γ was determined at the position of every particle within the particle structures. For the particle chain shown in the Fig. 5.15(a), the γ value for the top particle is 2.849 but only 1.016 at the position of the bottom particle, even though the maximum value for γ was 15.34. In

Fig. 5.15(b), every dust particle layer has a different value of γ. Only in transition 3 are the values of γ at the positions of different particles close to each other. This is primarily due to the small interparticle distances. Therefore, for vertically aligned dust particle structures, especially long dust particle chains, it is not valid to use the value of γ as measured at the position of the top particle to represent the value of γ for the entire structure.

Obviously, inside the box, the value of γ is relatively large in the region where the sheaths of box walls are overlapping. In these sheath overlapping regions, the vertical confinement tends to be ‘flat’ while the horizontal confinement is significant because dust particles are inside the sheaths of the box side walls and then experience strong electrical field force from the box side walls. Therefore, there are a small vertical confinement strength and a large horizontal confinement strength, which means large value of γ. Outside these regions, the situation is similar to the cases without the box, for example, a cutoff electrode, where the vertical confinement strength is usually much larger than the horizontal confinement strength or have smaller values of γ.

In order to investigate the relationship between γ and dust system structural transitions, γ for three transitions, each having a different particle number, has been measured. The largest, smallest and average γ at the positions of dust particle levitating for these structures is recorded in Table 5.1.

Table 5.1. The maximum, smallest and average γ at three transition points for these dust particle structures having different numbers of particle.

Particle Number		5		6	7	8	9	10
Tran1	γ_{Max}	7.64		12.71	15.34	20.87	27.23	40.13
	γ_{Min}	0.94		1.06	1.01	0.99	0.92	1.11
	γ_{Avg}	2.41		4.81	5.37	5.85	6.24	7.11
Tran2	γ_{Max}	0.54		0.57	0.68	0.88	0.79	0.72
	γ_{Min}	0.49		0.50	0.48	0.51	0.55	0.52
	γ_{Avg}	0.52		0.54	0.58	0.66	0.72	0.68
Tran3	γ_{Max}	0.22		0.22	0.22	0.23	0.24	0.21
	γ_{Min}	0.20		0.21	0.21	0.19	0.21	0.20
	γ_{Avg}	0.21		0.22	0.22	0.22	0.23	0.21

As shown in Table 5.1 transition 3, all of the γ_{Max}, γ_{Min} and γ_{Ave} for all structures consisting of the different numbersof particles are approximately 0.22. However, for transitions 1 and 2, γ_{Max} and γ_{Min} vary with particle number. As an example, for transition 1, γ_{Max} increases from 7.64 to 40.13 and γ_{Ave} increases from 2.41 to 7.11 with increasing particle number. Interestingly, in this case, γ_{Min} remains unchanged with the change in particle number. For transition 1, γ_{Min} is around 1.00±0.15 while for transitions 2 and 3, it is 0.52±0.03 and 0.21±0.02, respectively. This shows that these transitions are actually related to γ_{Min}.

A second point of interest is that the value of the γ_{Min} of the transition 2 is very closed to the reported [Samarian, 2010] value of γ when the particle pair Vertical-to-Horizontal transitions (VHT) were observed. In our experiments within the box, the VHT are easily obtained using laser perturbation when γ_{Min} is smaller than that for transition 2 γ_{Min}. However, these transintions can not be achieved when γ_{Min} is larger.

It might be explained by a simple model. If the dust particles in a particle structure experience larger horizontal squeezing force than vertical squeezing forces, particles tend to move in the vertical direction and align along the vertical direction. Otherwise, they tend to move in the horizontal direction and align alone the horizontal direction. Here, the squeezing force may come from confinement, coulomb force, ion-wake force or any force acting on the dust particles. For the vertical dust particle chain, γ_{Min} is larger than 1. The horizontal confinement force is larger than the vertical confinement force for every dust particle in the chain. Since there is no horizontal inter-particle force and the vertical inter-particle force is small compared with the vertical confinement force due to the large inter-particle distance, the squeezing force is approximately equal to the confinement force. Therefore, for each particle in the chain, the horizontal squeezing force is larger than then vertical squeezing force

To justify this relationship, the particle number was held at N= 6 while changing the pressure from 60 to 140 mTorr and reproducing experiments above. The values of γ_{Min} at each transition point are shown in Fig. 5.16(a). As can be seen γ_{Min} remains stable even for pressure changes. This indicates that for any particle inside a particle structure that experiences a value of γ closer to the transition value γ_{Min}, the structure loses its current stable structure and begins the transition. This explains why particle chains with different particle numbers become unstable at different RF powers. Taking transition 1 as an example and using data from our experiment, when γ_{Min} approaches 1, the chain loses its stability and starts the transition. As an example, for the 7-particle-chain shown in Fig. 5.15(a), the bottom particle has the lowest measured valye of γ, reaching 1 which is closed to the transition $\gamma_{Min.}$ Therefore, the transition 1 will occure. If one additional particle is 'dropped', the remainder of the particles maintain their same positions under this operating condition. In this case, the top particle has the lowest value of γ (2.849). Since this is larger than 1, the chain will remain stable until if the power is increased or the gas pressure is reduced, which make the lowest value of γ for the particles in the chain less than 1.

To verify this relationship, the same experiments were conducted within a 1 inch glass box. The results are shown in Fig. 5.16 (b). For transitions 1, 2 and 3, the value of γ is 1.02 ± 0.09, 0.48 ± 0.02 and 0.21 ± 0.03, respectively. As can be seen, although these transitions within the 1 inch box occur under different operating conditions, the values of γ_{Min} at the transition points are close to identical the same, which confirms the existence of a relationship between γ_{Min} and dust particle structuring.

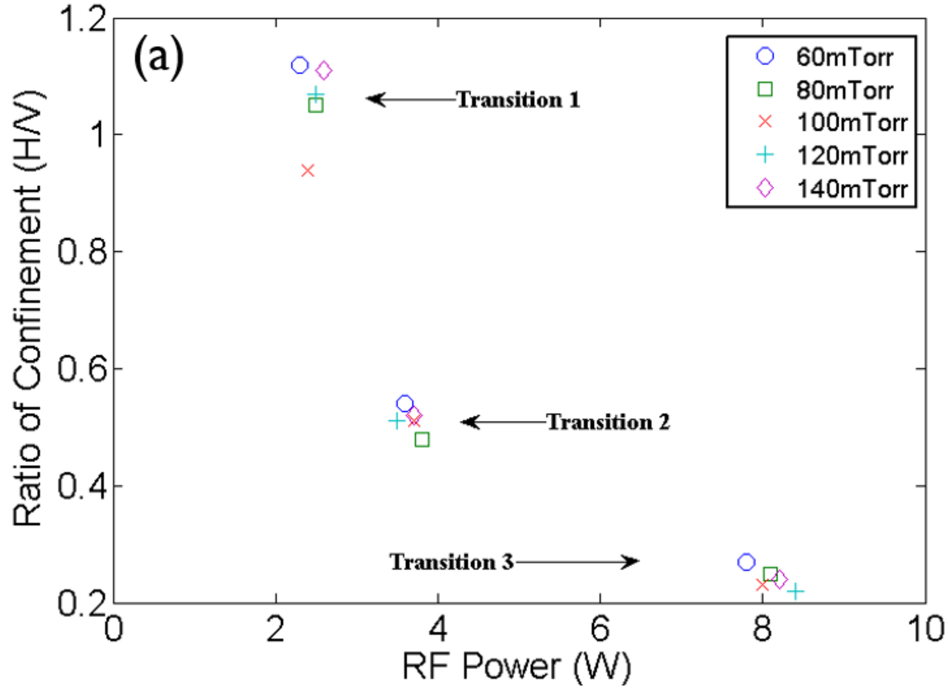

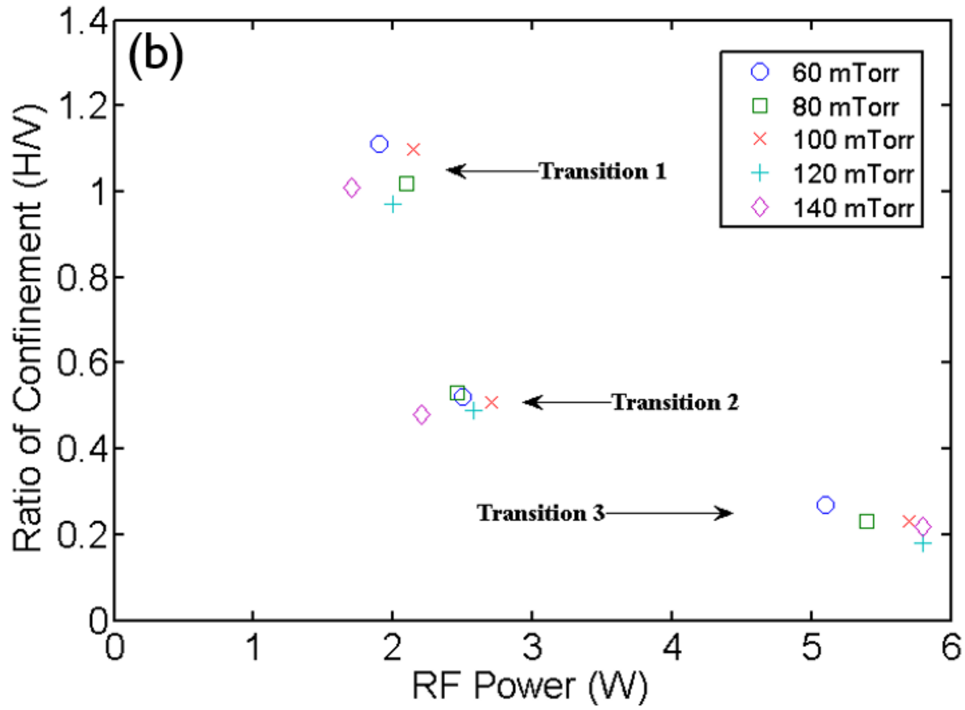

Figure 5.16. The minimum value of the ratio of the confinement strength between the horizontal and vertical direction (γ_{min}) at the particle levitating positions under the transition parameters within the half inch box (a) and the one inch box (b).

5.5 Conclusions

In this Chapter, the result of experiment to produce interparticle force maps between the top and the bottom particles of a two-particle chain were mentioned. The maps were generated employing a laser beam to perturb each individual particle. A nonreciprocal particle interaction was observed in both the horizontal and vertical directions, confirming the existence of an ion-wake field within the glass box. It was shown that, for this case, the predicted attractive horizontal nonreciprocal phenomenon can only be observed near the midline of the box due to the existence of the strong inherent confinement forces produced by the walls of box, whereas in the vertical direction, the nonreciprocal ratio is much greater than that observed without a glass box confinement. This explains why the existence of an ion-wake field in a glass box has long been in question; the horizontal attractive interaction between a particle and the ion-wake field is much smaller than that provided by the confinement force created by the box walls for most regions within the box. These results show that although the ion wake field force plays a role in the formation of dust particle vertical structures, it does not play the crucial role. Instead, the confinement force is the key factor for determining dust particle structuring. One representative example of this is the extended levitation region observed where dust particles can experience an upward force approximately equal to that of the gravitational force. This "flat" confinement region is a key factor in forming long 1D vertically aligned dust particle structures. It is also interesting to note that form a 1D vertical dust particle chain requires a value of γ, which is the ratio between the horizontal and vertical confinement strength, larger than1 (at the position of each individual dust particle inside the chain). Finally, three typical transitions have been reported in this chapter and the minimum value of γ where such a transition can begin for such a dust particle structure have been identified.

CHAPTER SIX

Summary and Future Work

In a complex (dusty) plasma, dust particles acting as a charged species provide a plasma which is both more complicated and closer to the real environment observed in the universe and industry. At the same time, dust particles are natural tools for investigating such plasmas, in particular the plasma sheath which is crucial to the semi-conductive and self-assembling system which are important to next generation nanofab industry. In this thesis, we focused on the interesting dust particle structures which can exist in the plasma sheath and how these can be used to determine the properties of the sheath, especially overlapping sheaths by using the dust particles as probes.

In first part of the thesis, a novel technique for minimally perturbative measurement of complex plasma, especially the plasma sheath was introduced. This technique, which is named the freefall technique, exhibits both minimal perturbation and good spatial resolution. In this technique, a few hundreds of dust particles were dropped from a dust dropper located above the upper electrode into the sheath, with individual particle motion recorded at 1000 fps. A MATLAB-based algorithm for particle detection was employed to identify individual particles in each frame of the data collected, which were then linked using the Hungarian algorithm. By applying this technique, accurate sheath profiles of a planar electrode under different operating conditions were obtained. The sheath width and the manner in which it changed for various operating conditions was measured. This technique was also employed to investigate overlapping sheaths inside a glass box, which are similar to the trench-like situations observed in industry. Overlapped sheaths inside a trench were measured experimentally for the first time with results identifying clearly where the sheath produced by the side walls of the glass box begin to overlap with one another. It was also shown that overlapping the sheaths produced by the side walls modified the profile of the sheath of the lower electrode significantly. Instead of an almost linear vertical electric field force profile, a relatively 'flat' curve was observed in this sheath overlapping region.

The second part of this thesis examined ordered dust particle structures and manner in which they are influenced by the forces existing within the plasma sheath. Both the ion-wake field force and the confinement force, which are usually considered as two of the most important forces in forming the ordered dust particle structures were investigated. Interaction maps between the top and the bottom particles and the bottom and the top particles of a two-particle chain were generated employing a laser beam to perturb each individual particle. The ion wake was proven to exist inside a glass box, which has been in doubt for a long time. Additionally, the ion-wake field force inside the glass box was mapped experimentally, which was rarely done before. Both the horizontal and vertical nonreciprocal interaction ratio was recorded. It was shown that, for this case, the predicted attractive horizontal nonreciprocal phenomenon can only be observed near the midline of the box due to the existence of strong inherent confinement forces produced by the box, whereas in the vertical direction, this nonreciprocal ratio is much greater than that observed without a glass box confinement. It was also shown that due to the small magnitude of these forces as compared with the confinement force, the ion-wake field force inside the glass box could not be the key factor for forming different dust particle structures. In another words, the confinement force determines dust particle structuring. To clarify the relationship between the confinement force and the dust particle structures, the confinement force was measured under different operating conditions to determine its relationship to formation of different dust particle structures. Inside a glass box, three typical transitions between dust particle structures were observed: the vertical chain to zigzag structure transition (transition 1), the helical to a double layer transition (transition 2) and the double layer to single layer transition (transition 3). These transitions were found to be highly depending on γ, the ratio of horizontal and vertical confinement strength. To form a vertical chain, the value of γ at the position of each dust particle of the chain must be larger than 1, otherwise, the transition 1 will occur. This explains how dust particle number effects the stability of the dust particle chain. As a second example, in order to obtain a helical structure, γ_{min}, the minimum value of γ at the position of each dust particle in the structure, must be larger than approximately 0.48 but less than 1. Finally for double layer to single layer transitions, the regions of γ_{min} must be $0.21 < \gamma_{min} < 0.48$ and $\gamma_{min} > 0.48$, respectively.

In future work, the free-fall technique needs to be improved in both time and spatial resolution. This enhancement would allow investigation of both the sheath and the overlapping sheath in a more detailed manner. It would also allow the ion-wake resulting from more complicated dust particle structures to be measured.

BIBLIOGRAPHY

Allen, J.E., "Probe theory: the orbital motion approach", *Phys. Scripta 45,* 497–503, 1992.

Allen, J.E., Annaratone, B.M., de Angelis, U., "On the orbital motion limited theory for a small body at floating potential in a Maxwellian plasma", *J. Plasma Phys. 63,* 299–309, 2000.

Angelis U., and A. Forlani, "Grain charge in dusty plasmas", *Phys. Plasmas. 5,* 3068, 1998.

Arp, O., Block, D., and Piel, A., "Dust Coulomb Balls: Three-Dimensional Plasma Crystals", *Phys. Rev. Lett. 93,* 165004, 2004.

Arp, O., D. Block, M. Klindworth, and A. Piel, "Confinement of Coulomb balls", *Phys. Plasmas 12*, 122102, 2005.

Barge, L. B., "Charging Processes and Effects in a Coupled Dusty Plasma", *Dissertation,* 1998.

Barkan, A., D'Angelo, N., Merlino, R.L., "Charging of dust grains in a plasma", *Phys. Rev. Lett. 73,* 3093–3096, 1994.

Barkan, A., Merlino, R.L., and D'Angelo, N., "Laboratory Observation of the Dust Acoustic Wave Mode", *Phys. Plasmas 2,* 3563, 1995.

Barnes, M.S., Keller, J.H., Forster, J.C., O'Neill, J.A., Coultas, D.K., "Transport of dust particles in glow-discharge plasmas", *Phys. Rev. Lett. 68,* 313–316, 1992.

Basner, R., F. Sigeneger, D. Loffhagen, G. Schubert, H. Fehske, and H. Kersten, New J. Particles as probes for complex plasmas in front of biased surfaces, *Phys. 11,* 013041, 2009.

Bittencourt, J. A., "Fundamentals of Plasma Physics", Pergamon, New York, 1986.

Bohm, D., "Minimum ionic kinetic energy for a stable sheath" in "The Characteristics of Electrical Discharges in Magnetic Field", edited by A. Guthrie and R. K. Wakerling, p. 77, McGraw-Hill, New York, 1949.

Bouchoule, A., "Dusty plasmas – Physics, Chemistry and Technological Impacts in Plasma Processing", *John Wiley and Sons Ltd.*, 1999.

Boufendi, L., and Bouchoule, A., “Industrial developments of scientific insights in dusty plasmas”, *Plasma Sources Sci. Technol. 11(3A),* 211-218, 2002.

Chen, F. F., Chap. 4 in “Plasma Diagnostic Techniques”, edited by R. H. Huddlestone and S. L. Leonard, *Academic,* New York, 1965.

Chen, F. F., “Introduction to Plasma Physics and Controlled Fusion, Vol. 1: Plasma Physics”, *Second Edition, Plenum Press,* 1984.

Chu, J.H., I, L., “Direct observation of Coulomb crystals and liquids in strongly coupled rf dusty plasmas”, *Phys. Rev. Lett. 72*, 4009–4012, 1994.

Creel, J., “Characteristic Measurements within a GEC rf Reference Cell”, *Dissertation,* 2010.

D’Angelo N., “Dusty plasma ionization instability with ion drag”, *Phys. Plasmas 5,* 3155–3160, 1998.

D’Angelo N. and R. L. Merlino, “Current-driven dust-acoustic instability in a collisional plasma”, *Planet. Space Sci., Vol. 44. No. 12,* pp. 1593 -1598, 1996

Douglass, A., Land, V., Matthews, L., and Hyde, T., “Dust particle charge in plasma with ion flow and electron depletion near plasma boundaries”, *Phys. Plasmas* ***18***, 083706, 2011.

Douglass A., Victor Land, Ke Qiao, Lorin Matthews, and Truell Hyde, “Determination of The levitation limits of dust particles within the sheath in complex plasma experiments”, *Phys. Plasmas 19,* 013707, 2012.

Daugherty, J. E., Porteous, R. K., and Graves, D. B., “Electrostatic forces on small particles in low pressure discharges”, *J. Appl. Phys. 73,* 1617, 1993;

Eliezer, S., and Eliezer, Y., “The Fourth State of Matter: An Introduction to Plasma Science”, *Second Edition*, *IOP published*, 2001.

Epstein, P. S., “On the Resistance Experienced by Spheres in their Motion through Gases”, *Phys. Rev. 23,* 710, 1924.

Farouki, R.T., Hamaguchi, S., “Thermal energy of crystalline one-component plasma from dynamical simulation”, *Phys. Rev. E 47,* 4330–4336, 1993.

Flanagan, T. M. and J. Goree, “Observation of the spatial growth of self-excited dustdensity waves”, *Phys. Plasmas 17,* 123702, 2010.

Flanagan, T. M. and J. Goree, “Development of nonlinearity in a growing self-excited dust-density wave”, *Phys. Plasmas 18,* 013705, 2011.

Fortov, V. E., Nefedov, A. P., Torchinsky, V. M., Molotkov, V. I., Petrov, O. F., Samarian, A. A., Lipaev, A. M., and Khrapak, A. G., “Crystalline structures of strongly coupled dusty plasmas in dc glow discharge strata”, *Phys. Lett. A 229,* 317, 1997.

Fortov, V. E., A. P. Nefedov,V.A. Sinel’shchikov, A. D. Usachev, and A. V. Zobnin, Filamentary dusty structures in RF inductive discharge, *Phys. Lett. A 267,* 179, 2000a.

Fortov, V.E., A.G. Khrapak, S.A. Khrapak, V.I. Molotkov, A.P. Nefedov, O.F. Petrov, V.M. Torchinsky, “Mechanism of dust–acoustic instability in a current glow discharge plasma”, *Phys. Plasmas 7,* 1374–1380, 2000b.

Fortov, V.E., A.D. Usachev, A.V. Zobnin, V.I. Molotkov, O.F. Petrov, “Dust–acoustic wave instability at the diffuse edge of radio frequency inductive low-pressure gas discharge plasma”, *Phys. Plasmas 10,* 1199–1207, 2003.

Fortov, V. E., Petrov, O. F., Usachev, A. D., and Zobnin, A. V., “Micron-sized particlecharge measurements in an inductive rf gas-discharge plasma using gravity-driven probe grains”, *Phys. Rev. E 70,* 046415, 2004a.

Fortov, V. E., Khrapak, A. G., Khrapak, S. A., Molotkov, V. I., and Petrov, O. F., “Dusty Plasmas”, *Usp. Fiz. Nauk 174,* 495, 2004 [*Phys. Usp. 47,* 447, 2004b].

Fortov, V.E., Ivlev, A.V., Khrapak, S.A., Khrapaka, A.G., Morfill, G.E., “Complex (dusty) plasmas: Current status, open issues, perspectives”, *Phys. Reports 421,* 1 – 103, 2005.

Frost L. S., “Effect of Variable Ionic Mobility on Ambipolar Diffusion”, *Phys. Rev. 105,* 354-356, 1957.

Gozadinos, A. V. Ivlev and J. P. Boeuf, “A fluid model for colloidal plasmas under microgravity G. conditions”, *New J. Phys. 5* 32.1–32.9, 2003.

Goedheer W. J., V. Land and J. Venema, “Hydrodynamic and kinetic modelling of complex radio-frequency plasmas”, *J. Phys. D: Appl. Phys. 42* 194015, 2009.

Hamaguchi, S., Farouki, R. T., Dubin, D. H. E, “Triple point of Yukawa systems”, *Phys. Rev. E 56,* 4671–4682, 1997.

Hargis, P.J., Greenberg, K.E., Miller, P.A., et al. “The gaseous electronic conference radio-frequency reference cell: a defined parallel-plate radio-frequency system for experimental and theoretical studies of plasma-producing discharges”, *Rev. Sci. Instrum. 65 (1),* 140–154, 1994.

Havnes, O., Aanesen, T. K., and Melandsϕ, F., “On Dust Charges and Plasma Potentials in a Dusty Plasma With Dust Size Distribution”, *J. Geophys. Res. 95*, 6581–6585, 1990.

Hayashi, Y., and Tachibana, S., “Observation of Coulomb-crystal formation from carbon particles grown in a methane plasma”, *Japan. J. Appl. Phys. 33* L804–L806, 1994.

Hebner G. A. *et al.*, “Direct Determination of Particle-Particle Interactions in a 2D Plasma Dust Crystal”, *Phys. Rev. Lett. 87*, 235001, 2001.

Hebner, G. A., Riley, M. E., and Marder, B. M., “Dynamic probe of dust wakefield interactions using constrained collisions”, *Phys. Rev. E 68*, 016403, 2003.

Hebner, G. A., Riley, M. E., “Measurement of attractive interactions produced by the ion Wakefield in dusty plasmas using a constrained collision geometry”, *Phys. Rev. E 68*, 046401, 2003.

Hebner, G. A., Riley, M. E., “Structure of the ion wakefield in dusty plasmas”, *Phys. Rev. E 69*, 026405, 2004.

Hollenstein, Ch, The physics and chemistry of dusty plasma, *Plasma Phys. Control. Fusion 42*, R93, 2000

Homann, A., Melzer, A., Peters, S., and Piel, A., “Determination of the dust screening length by laser-excited lattice waves”, *Phys. Rev. E 56*, 7138–7141, 1997.

Homann, A., Melzer, A., and Piel, A., “Measuring the charge on single particles by laser excited resonances in plasma crystals”, *Phys. Rev. E 59*, R3835–R3838, 1998a.

Homann, A., Melzer, A., Peters, S., Madani, R., Pie1, A., “Laser-excited dust lattice waves in plasma crystals”, *Physics Letters A 242*, 173-180, 1998b.

Homann, A., Melzer, A., and Piel, A., “Measuring the charge on single particles by laserexcited resonances in plasma crystals”, *Phys. Rev. E 59*, R3835, 1999.

Hone, J., M. Whitney, C. Piskoti, and A. Zettl, “Thermal conductivity of single-walled carbon nanotubes”, *Phys. Rev. B 59*, R2514, 1999.

Hørlück, S. and P. Dimon , Statistics of shock waves in a two-dimensional granular flow, *Phys. Rev. E 60*, 671,1999.

Hutchinson, I.H., “Ion collection by a sphere in a flowing plasma: 2. Non-zero Debye length”, *Plasma Phys. Control. Fusion 45*, 1477–1500, 2003.

Hutchinson, I.H., “Ion collection by a sphere in a flowing plasma: 3. Floating potential and drag force”, *Plasma Phys. Control. Fusion 47*, 71–87, 2005.

Ignatov, A.M., “Interaction between Dust Grains near a Conducting Wall”, *Plasma Physics Reports, Vol. 29,* No. 4, 2003, pp. 296–299. Translated from *Fizika Plazmy, Vol. 29*, No. 4, 2003, pp. 325–328.

Ikezi, H., “Coulomb solid of small particles in plasmas”, *Phys. Fluids 29,* 1764-1766, 1986.

Ivlev, A.V., Morfill, G., Fortov, V.E., “Potential of a dielectric particle in a flow of a collisionless plasma”, *Phys. Plasmas 6,* 1416–1420, 1999.

Ivlev A. V. and G. Morfill, “Acoustic modes in a collisional dusty plasma: Effect of the charge variation”, *Phys. Plasmas 7,* 1094, 2000.

Ivlev, A.V., Khrapak, S.A., Zhdanov, S.K., Morfill, G.E., Joyce, G., “Force on a charged test particle in a collisional flowing plasma”, *Phys. Rev. Lett. 92,* 205007/1-4, 2004a.

Ivlev, A.V., Zhdanov, S.K., Khrapak, S.A., Morfill, G.E., “Ion drag force in dusty plasmas”, *Plasma Phys. Control. Fusion 46,* B267–B279, 2004b.

Ivlev, A.V., Zhdanov, S.K., Khrapak, S.A., Morfill, G.E., “Kinetic approach for the ion drag force in a collisional plasma*”, Phys. Rev. E 71,* 016405/1-7, 2005.

Joyce G., M. Lampe, and G. Ganguli, “Instability-Triggered Phase Transition to a Dusty-Plasma Condensate”, Phys. Rev. Lett. 88. 095006, 2002.

Khrapak, S.A., Ivlev, A.V., and Morfill, G., “Interaction potential of microparticles in a plasma: role of collisions with plasma particles”, *Phys. Rev. E 64* 046403/1-7, 2001.

Khrapak, S., D. Samsonov, G. Morfill, H. Thomas, V. Yaroshenko, H. Rothermel, T. Hagl, V. Fortov, A. Nefedov, V. Molotkov, O. Petrov, A. Lipaev, A. Ivanov, Y. Baturin, “Compressional waves in complex (dusty) plasmas under microgravity conditions”, *Phys. Plasmas 10,* 1–4, 2003a.

Khrapak, S.A., Ivlev, A.V., Morfill, G.E., “Momentum transfer in complex plasmas”, *Phys. Rev. E 70*, 056405/1-9, 2004.

Khrapak, S.A., Ratynskaia, S.V., Zobnin, A.V., Usachev, A.D., Yaroshenko, V.V., Thoma, M.H., Kretschmer, M., Hebner, H., Morfill, G.E., Petrov, O.F., Fortov, V.E., "Particle charge in the bulk of gas discharges", *Phys. Rev. E 72*, 016406/1-10, 2005a.

Khrapak, S. A., Ivlev, A. V., Zhdanov, S. K., and Morfill, G. E., "Hybrid approach to the ion drag force", *Phys. Plamsas 12*, 042308, 2005b. Kittel C., "Introduction to Solid State Physics 7th edition", *New York: Wiley*, 1996.

Kong, J., T. Hyde, L. Matthews, K. Qiao, Z. Zhang and A. Douglass, "One-dimensional vertical dust strings in a glass box", *Phys. Rev. E* 84, 016411, 2011.

Konopka, U., Ratke, L., and Thomas, H. M., "Central Collisions of Charged Dust Particles in a Plasma", *Phys. Rev. Lett. 79,* 1269–1272, 1997.

Konopka, U., Morfill, G. E., and Ratke, L., "Measurement of the Interaction Potential of Microspheres in the Sheath of a rf Discharge", *Phys. Rev. Lett. 84,* 891, 2000.

Lampe, M., Joyce, G., Ganguli, G., and Gavrishchaka, V., "Interactions between dust grains in a dusty plasma", *Phys. Plasmas 7,* 3851–3861, 2000.

Lampe, M., Gavrishchaka, V., Ganguli, G., Joyce, G., "Effect of trapped ions on shielding of a charged spherical object in a plasma", *Phys. Rev. Lett. 86,* 5278–5281, 2001.

Lampe, M., Goswami, R., Sternovsky, Z., Robertson, S., Gavrishchaka, V., Ganguli, G., Joyce, G., "Trapped ion effect on shielding, current flow, and charging of a small object in a plasma", *Phys. Plasmas 10,* 1500–1513, 2003.

Land V., Smith, B., Matthews, L., and Hyde T., "Probing the Sheath Electric Field With a Crystal Lattice by Using Thermophoresis in Dusty Plasma", *Transactions on Plasma Science, Vol. 38,* NO. 4, 2010.

Lapenta, G., "Simulation of charging and shielding of dust particles in drifting plasmas", *Phys. Plasmas 6*, 1442–1447, 1999.

Lepria, S., P. Sandri, and A. Politi, "The one-dimensional Lennard-Jones system: collective fluctuations and breakdown of hydrodynamics", *Eur. Phys. J. B 47*, 549, 2005.

Liao, Chen-Ting, Lee-Wen Teng, Chen-Yu Tsai, Chong-Wai Io, and Lin I, "LagrangianEulerian Micromotion andWave Heating in Nonlinear Self-Excited Dust AcousticWaves", *Phys. Rev. Lett. 100*, 185004, 2008.

Lifshitz, E.M., L.P. Pitaevskii, "Physical Kinetics", Pergamon, Oxford, 1981.

Liu, B., Goree, J., and Nosenko, V., “Radiation pressure and gas drag forces on a melamine-formaldehyde microsphere in a dusty plasma”, *Phys. Plasmas 10,* 9-20, 2003.

Liu, B. and J. Goree, “Phonons in a one-dimensional Yukawa chain: Dusty plasma experiment and model”, *Phys. Rev. E 71,* 046410, 2005.

McGhee, C. A., *et al*., “HST observations of spokes in Saturn's B ring”, Icarus 173, 508-521, 2005.

Melzer, A., Trottenberg, T., and Piel, A., “Experimental determination of the charge on dust particles forming Coulomb lattices”, *Phys. Lett. A 191,* 301-308, 1994.

Melzer, A., Schweigert, V. A., and Piel, A., “Transition from Attractive to Repulsive Forces between Dust Molecules in a Plasma Sheath”, *Phys. Rev. Lett. 83,* 3194, 1999.

Melzer, A., Schweigert, V. A., and Piel, A., “Measurement of the Wakefield Attraction for “Dust Plasma molecules”, *Physica Scripta. Vol. 61,* 494-591, 2000.

Melzer, A. and Goree, J., “Fundamentals of dusty plasmas *Low Temperature Plasmas* vol 1” ed R Hippler, H. Kersten, M. Schmidt and K. H. Schoenbach (*New York: Wiley*) pp. 129, 2008.

Merlino, R. L., A. Barkan, C. Thompson, and N. D’Angelo, “Laboratory studies of waves and instabilities in dusty plasmas”, *Phys. Plasmas 5*, 1607–1614, 1998.

Merlino R. L., “Dust-acoustic waves driven by an ion-dust streaming instability in laboratory discharge dusty plasma experiments”, *Phys. Plasmas 16*, 124501, 2009.

Mitchell, C. J., *et al*., “Saturn's Spokes: Lost and Found.”, *Science 311*, 1587, 2006.

Molotkov, V.I., A.P. Nefedov, V.M. Torchinskii, V.E. Fortov, A.G. Khrapak, “Dust acoustic waves in a dc glow-discharge plasma”, *JETP 89*, 477–480, 1999.

Morfill, G. E., and Thomas, H., “Plasma crystal”, *J. Vac. Sci. Technol. A 14,* 490-495, 1996.

Morfill, G. E., H. M. Thomas, U. Konopka, H. Rothermel, M. Zuzic, A. Ivlev, and J. Goree, “Condensed Plasmas under Microgravity”, *Phys. Rev. Lett. 83*, 1598, 1999.

Northrop, T. G. and Birmingham, T. J., “Plasma drag on a dust grain due to Coulomb collisions”, *Planet. Space Sci. 38,* 319, 1990.

Nosenko, V., K. Avinash, J. Goree, and B. Liu, "Nonlinear Interaction of Compressional Waves in a 2D Dusty Plasma Crystal", *Phys. Rev. Lett. 92*, 085001, 2004.

Nosenko V., S. K. Zhdanov, S.-H. Kim, J. Heinrich, R. L. Merlino and G. E. Morfill, "Measurements of the power spectrum and dispersion relation of self-excited dust acoustic waves", *Europhys. Lett. 88*, 65001, 2009.

Nunomura, S., Samsonov, D., and Goree, J., "Transverse waves in a two-dimensional screened-Coulomb crystal (dusty plasma)", *Phys. Rev. Lett. 84*, 5141–5144, 2000.

Nunomura, S. Goree, J., Hu, S., Wang, X., and Bhattacharjee, A., "Dispersion relations of longitudinal and transverse waves in two-dimensional screened Coulomb crystals", *Phys. Rev. E 65*, 066402, 2002.

Olthoff, J. K., and Greenberg, K. F., "The Gaseous Electronics Conference RF Reference Cell—An Introduction", *J. Res. Natl. Inst. Stand. Technol. 100*, 327, 1995.

Pandey, B. P. and Dutta, A., "The Bohm criterion for a dusty plasma sheath", *Pramana Vol. 65*, NO 1, 117-124, 2005.

Peters, S., Homann, A., Melzer, A., and Piel, A., "Measurement of dust particle shielding in a plasma from oscillations of a linear chain", *Phys. Lett. A 223*, 389–393, 1996.

Piel, A., M. Klindworth, and O. Arp, "Obliquely Propagating Dust-Density Plasma Waves in the Presence of an Ion Beam", *Phys. Rev. Lett. 97*, 205009, 2006.

Pramanik, J., B. M. Veeresha, G. Prasad, A. Sen, and P. K. Kaw, "Experimental observation of dust-acoustic wave turbulence", *Phys. Lett. A 312*, 84, 2003.

Quinn R. A., and Goree, J., "Particle Interaction Measurements in a Coulomb Crystal Using Caged-Particle Motion", *Phys. Rev. Lett. 88*, 195001, 2002.

Rao, N. N., Shukla, P. K., and Yu, M. Y., "Dust-Acoustic Waves in Dusty Plasma", *Planet. Space Sci. 38*, 543, 1990.

Ratynskaia, S.V., Khrapak, S.A., Zobnin, A.V., Usachev, A.D., Yaroshenko, V.V., Thoma, M.H., Kretschmer, M., Quinn, R.A., Morfill, G.E., Petrov, O.F., Fortov, V.E., "Experimental Determination of Dust-Particle Charge in a Discharge Plasma at Elevated Pressures", *Phys. Rev. Lett. 93*, 085001, 2004.

Riemann, K., "The Bohm criterion and sheath formation", *J. Phys. D: Appl. Phys.* 24, 493, 1991.

Riemann, K., "The influence of collisions on the plasma sheath transition", *Phys. Plasmas 4*, 4158, 1997.

Roca i Cabarrocas, P., Gay, P., and Hadjadj, A., "Experimental evidence for nanoparticle deposition in continuous argon-silane plasmas: Effects of silicon nanoparticles on film properties", *J. Vac. Sci. Technol. A 14,* 655, 1996.

Rosenberg, M., "Ion- and dust-acoustic instabilities in dusty plasmas", *Planet. Space Sci. 41,* 229, 1993.

Rosenberg M., E. Thomas, Jr, and R. L. Merlino, "A note on dust wave excitation in a plasma with warm dust: Comparison with experiment", *Phys. Plasmas 15,* 073701, 2008. Roth, J. R., "Industrial plasma engineering Volume 2: Application to nonthermal plasma processing", *Institute of Physics Publishing, Bristol and Philadelphia,* 2001.

Rothermel, H., T. Hagl, G. E. Morfill, M. H. Thoma, and H. M. Thomas, "Gravity Compensation in Complex Plasmas by Application of a Temperature Gradient", *Phys. Rev. Lett. 89,* 175001, 2002.

Samarian, A.A., and James, B.W., "Sheath measurement in rf-discharge plasma with dust grains", *Physics Letters A 287,* 125–130, 2001.

Samarian, A. A., and James, B. W., "Dust as fine electrostatic probes for plasma diagnostic", *Plasma Phys. Control. Fusion 47,* B629–B639, 2005.

Sato, N., G. Uchida, T. Kaneko, S. Shimizu, and S. Iizuka, "Dynamics of fine particles in Magnetized plasmas", *Phys. Plasmas 8,* 1786, 2001.

Schollmeyer, H., Melzer, A., Homann, A., and Piel, A., "Dust–dust and dust - plasma interactions of monolayer plasma crystals", *Phys. Plasmas 6,* 2693, 1999.

Schwabe, M., M. Rubin-Zuzic, S. Zhdanov, H. M. Thomas, and G. E. Morfill, "Highly Resolved Self-Excited Density Waves in a Complex Plasma", *Phys. Rev. Lett. 99,* 095002, 2007.

Schwabe, M., Zhdanov, S. K., Thomas, H. M., Ivlev, A. V., Rubin-Zuzic, M., Morfill, G. E., Molotkov, V. I., Andrey M Lipaev, Vladimir E Fortov and Thomas Reiter, "Nonlinear waves externally excited in a complex plasma under microgravity conditions", *New J. Phys. 10,* 033037, 2008

Schweigert, V. A., I. V. Schweigert, A. Melzer, A. Homann, and A. Piel, "Alignment and instability of dust crystals in plasmas", *Phys. Rev. E 54,* 4155, 1996.

Selwyn, G. S., Heidenreich, J. E., and Haller, K. L., "Particle trapping phenomena in radio frequency plasmas", *Appl. Phys. Lett. 57,* 1876 1990.

Sheridan, T. E., Dusty plasma ring model, *Phys. Scr. 80*, 065502, 2009.

Shukla, P. K., Mamun, A. A., “Introduction to Dusty Plasma Physics”, *Institute of Physics Publishing, Bristol and Philadelphia*, ISBN 0 7503 0653 X, 2002.

Smith, B. A., *et al*., “Encounter with Saturn: Voyager 1 Imaging Science Results”, *Science, New Series 212*, 163-191, 1981. Smith, B. A., *et al*., “A New Look at the Saturn System: The Voyager 2 Images”, *Science, New Series 215*, 504-537, 1982.

Smith Jr., B. A. T., “An Experimental Study of Phase Transitions in a Complex Plasma”, *Dissertation*, 2005.

Sparks, M., Theory of Electron-Avalanche Breakdown in Solids, in Laser-Induced Damage in Optical Materials, edited by A. J. Glass and A. H. Guenther (National Bureau of Standards, Washington, D. C., *Special Publication 435*, 1975), p. 331v.

Sukhinin G. I. and A. V. Fedoseev, “Influence of dust-particle concentration on gas discharge plasma”, *Phys. Rev. E 81*, 016402, 2010.

Teng, Lee-Wen, Mei-Chu Chang, Yu-Ping Tseng, and Lin I, “Wave-Particle Dynamics ofWave Breaking in the Self-Excited Dust AcousticWave”, *Phys. Rev. Lett. 103*, 245005, 2009.

Thomas, E., Jr., R. Fisher, and R. L. Merlino, “Observations of dust acoustic waves driven at high frequencies: Finite dust temperature effects and wave interference”, *Phys. Plasmas 14*, 12370, 2007.

Thomas E., Jr., “Driven dust acoustic waves with thermal effects: Comparison of experiment to fluid theory”, *Phys. Plasmas 17*, 043701, 2010.

Thomas, H., Morfill, G.E., Demmel, V., Goree, J., Feuerbacher, B., Mlmann, D., “Plasma crystal: Coulomb crystallization in a dusty plasma”, *Phys. Rev. Lett. 73*, 652–655, 1994.

Thomas, H. M., , Gregor E. Morfill, Alexei V. Ivlev, Anatoli P. Nefedov, Vladimir E. Fortov, Hermann Rothermel, Milenko Rubin-Zuzic, Andrey M. Lipaev, Vladimir Molotkov, Oleg F. Petrov, “PKE-Nefedov Complex Plasma Research on the International Space Station”, *Micrograv. Sci. Technol. 16*, 317-321, 2005.

Thomas T., B. Dietmar, and P. Alexander, “Dust confinement and dust-acoustic waves in weakly magnetized anodic plasmas”, *Phys. Plasmas 13*, 042105, 2006.

Thompson, C., A. Barkan, N. D’Angelo, and R. L. Merlino, “Dust acoustic waves in a direct current glow discharge ” Phys. Plasmas 4, 2331, 1997.

Tomme, E. B., Law, D. A., Annaratone, B. M., and Allen, J. E., “Parabolic Plasma Sheath Potentials and their Implications for the Charge on Levitated Dust Particles”, *Phys. Rev. Lett. 85*, 2518–2521, 2000.

Trottenberg, Th, A Melzer and A Piel, Measurement of the electric charge on particulates Forming Coulomb crystals in the sheath of a radiofrequency plasma, *Plasma Sources Sci. Technol. 4,* 450458, 1995, Printed in the UK.

Trottenberg, T., D. Block, and A. Piel, “Dust confinement and dust-acoustic waves in weakly magnetized anodic plasmas”, *Phys. Plasmas 13,* 042105, 2006.

Tsytovich, V.N., Khodataev, Ya.K., Morfill, G.E., Bingham, R., Winter, D.J., “Radiative dust cooling and dust agglomeration in plasmas”, *Comments Plasma Phys. Control. Fusion 18* 281–291, 1998.

Tsytovich, V. N., and de Angelis, U., “Kinetic theory of dusty plasmas. I. General approach”, *Phys. Plasmas 6,* 1093, 1999.

Tsytovich V.N., U. de Angelis, R. Bingham, “Low-frequency responses and wave dispersion in dusty plasmas”, *Phys. Rev. Lett. 87* 185003/1-4, 2001.

Tsytovich V.N., U. de Angelis, R. Bingham, “Low frequency responses, waves and instabilities in dusty plasmas”, *Phys. Plasmas 9*, 1079–1090, 2002.

Vaulina, O. S., Lisin, E. A., Gavrikov A. V., Petrov, O. F., and Fortov, V. E., “Determination of Pair Interaction Forces between Particles in Nonideal Dissipative Systems”, *Phys. Rev. Lett. 103,* 035003, 2009.

Vaulina O. S., and Lisin, E. A., “Technique for analysis of interparticle interaction in Nonideal dissipative systems with isotropic pair potentials”, *Phys. Plasmas 16,* 113702, 2009.

Vaulina, O. S., and Khrapak, S. A., “Scaling law for the fluid-solid phase transition in Yukawa systems (dusty plasmas)”, *JETP, Vol. 90,* No. 2, 287–289, 2000.

Vladimirov, S.V., S.A. Maiorov, O. Ishihara, “Molecular dynamics simulation of plasma flow around two stationary dust grains”, *Phys. Plasmas 10,* 3867–3873, 2003.

Wang, X., Bhattacharjee, A. and Hu, S., “Longitudinal and Transverse Waves in Yukawa Crystals”, *Phys. Rev. Lett. 86,* 2569-2572, 2001.

Williams J. D., E. Thomas, Jr., “Initial measurement of the kinetic dust temperature of a weakly coupled dusty plasma”, *Phys. Plasmas 13*, 063509, 2006.

Williams, J. D., E. Thomas, Jr., and L. Marcus, “Observations of vertically propagating driven dust acoustic waves: Finite temperature effects”, *Phys. Plasmas 15*, 043704, 2008.

Williams, J. D. and Duff, J., “Observation of the coupling of the driven dust acoustic wave”, *Phys. Plasmas 17*, 033702, 2010.

Wurden, G. A., Wurden, A. J., and Gladstone Jr., I. M., “Plasma Tails: Comets HaleBopp and Hyakutake”, *IEEE Trans. Plasma Sci. 27*, 142, 1999.

Yaroshenko, V. V., Annaratone, B. M., Khrapak, S. A., Thomas, H. M., and Morfill, G. E., “Electrostatic modes in collisional complex plasmas under microgravity conditions”, *Phys. Rev. E 69*, 066401, 2004.

Yaroshenko V V, F Verheest, H M Thomas and G E Morfill, “The Bohm sheath criterion in strongly coupled complex plasmas”, *New J. Phys.* 11 073013, 2009.

Yaroshenko V. V., V. Nosenko, and G. E. Morfill, “Effect of strong electrostatic interactions of microparticles on the dust acoustic waves”, *Phys. Plasmas 17*, 103709, 2010.

Zafiu, C., Melzer, A., and Piel, A., “Nonlinear resonances of particles in a dusty plasma sheath”, *Phys. Rev. E 63*, 066403, 2001.

Zhang, Z., Kong, J., Qiao, K., Truell, H., and Matthews, L., “Simple method to measure The interaction potential of dielectric grains in a dusty plasma”, *Phys. Rev. E 82*, 036401, 2010.

Zobnin, A.V., Nefedov, A.P., Sinelshchikov, V.A., Fortov, V.E., “On the charge of dust particles in a low-pressure gas discharge plasma”, *JETP 91*, 483–487, 1999.

Zobnin, A.V., A.D. Usachev, O.F. Petrov, V.E. Fortov, “Dust–acoustic instability in an inductive gas-discharge plasma”, *JETP 95*, 429–439, 2002.